UNIVERSITEIT VAN PRETORIA
UNIVERSITY OF PRETORIA
YUNIBESITHI YA PRETORIA

Diffusion of implanted europium in glassy carbon

by

Mahboubeh Fathi Kenari

Submitted in partial fulfilment of the requirements for the degree of

DOCTOR OF PHILOSOPHY (PhD) IN PHYSICS

In the Faculty of Natural and Agricultural Sciences

University of Pretoria

15 January 2019

Supervisor: Prof. J. B. Malherbe

Co-supervisor: Dr. T. T. Hlatshwayo

DECLARATION

I, Mahboubeh Fathi Kenari, declare that the dissertation, which I hereby submit for the degree of PhD in University of Pretoria, is my own work and has not been submitted by for a degree at this or any other tertiary institution.

Signature: …….

Date: …….

SUMMARY

Diffusion of implanted europium in glassy carbon

BY

Mahboubeh Fathi Kenari

Submitted in partial fulfilment of the requirements for the degree of (PhD) in Physics in the Faculty of Natural and Agricultural Science, University of Pretoria

Supervisor/Promoter: Prof. J.B. Malherbe

Co- supervisor: Dr T.T Hlatshwayo

In my PhD study glassy carbon samples were implanted with 250 keV europium ions at room temperature and at 100 ^{o}C. The main purpose of my study was to study the diffusion properties of the europium in the glassy carbon.

After implantation the samples were investigated by several techniques to determine the damage created by the ion bombardment processes, the distribution of the europium atoms and possible reactions between the implanted europium and the glassy carbon substrate. The samples were also isochronally annealed in vacuum for a wide ranges of temperatures and again investigated after each heat treatment.

The following heat treatments were done. Room temperature europium implanted samples were annealed at 200-1000 ^{o}C for 1 h. Another set of room temperature implanted samples were annealed at 300-500 ^{o}C for 2 h. 100 ^{o}C implanted samples were annealed at 200-1000 ^{o}C for 1 h. These samples then were analysed to investigate the annealing of the initial damage, the diffusion of the implanted europium and possible reactions between the europium and glassy carbon induced by the ion bombardment and annealing.

The analytical techniques used in this study were RBS (Rutherford backscattering spectrometry), Raman spectroscopy and SEM (scanning electron microscopy). The diffusion and phase formation behavior of the europium ions were investigated with Rutherford backscattering spectrometry

(RBS), i.e. to see under the various high temperatures used, how much these ions diffused. Raman spectroscopy was used to study the structural changes in the glassy carbon due to ion bombardment and annealing.

The diffusion coefficient (D) values for room temperature implanted sample which was annealed for 1 h at 200 and 300 ºC were 2.3×10^{-19} and 1.2×10^{-19} m^2/s, respectively. Annealing at 400 ºC led to a loss of the implanted europium of about 30%. However increasing the temperature did not change this value and the retained europium in the glassy carbon samples was about 70% compared to the as-implanted samples for this range of temperature (400-1000 ºC).

The diffusion coefficient for room temperature implanted europium and then annealed for 2 h is the same that for 1 h. There was no europium lost at 300-400 ºC, while for the annealed sample from 425-500 ºC for 2h, the europium loss was about 25-45 %.

The diffusion coefficients for the 100 ºC implanted sample and then annealed at 200 and 300 ºC were 1.24×10^{-19} and 1.9×10^{-19} m^2/s, respectively. Good fitting of the experimental depth profiles to theory was obtained for the samples annealed from 300-700 ºC indicating that the diffusion was Fickian. The depth profiles for the samples annealed from 800-1000 ºC could no longer be fitted to the solution to the Fick diffusion differential equation. However, there was still europium migration to the surface resulting in europium loss reaching about 50% at 1000 ºC which is higher than the europium melting point ($T_{melting}$ = 826 ºC).

SEM images showed the topography of the surfaces due to ion bombardment and annealing. Furthermore, it also helped to understand the changes in morphology of samples (i.e. to see how much the bonding of materials is changed). There was also evidence of either europium oxide or carbide formation. The appearance of europium on the surface was due to diffusion of europium to the glassy carbon surface.

Raman results showed that ion implantation caused the two distinct D and G peaks of pristine glassy carbon to merge together into a broad peak. This is an indication that ion implantation caused amorphisation of implanted layer of the glassy carbon. By annealing the implanted sample to 1000 °C resulted in only partial recovery of the glassy carbon structure and it did not reach the pristine glassy carbon structure. This is due to retained radiation damage even after annealing at temperatures higher than the melting point of europium i.e. 826 ºC.

Finally, all the results were analyzed to make a recommendation about the suitability of glassy carbon as a storage materials for one of the important fission products, i.e. europium. The diffusion/segregation of europium to the surface to surface, amorphisation of glassy carbon after ion implantation are the positive aspect of the research. These aspects were resulted in that glassy carbon might be taken into a good nuclear storage material.

ACKNOWLEDGEMENTS

- I would like to express my appreciation to my supervisor, Prof. J. B. Malherbe, for his continued patience and support during the course of this study and for being excellent instructor and mentor.
- I would like to acknowledge Prof. C. C. Theron with his financial support during the PhD.
- I would also like to express my appreciation to Dr. T. T. Hlatshwayo as co-supervisor for his guidance about my results.
- I would also like to express my gratitude to our research group, Dr. O. S. Odutomowo, Dr. E. G. Njoroge, and Mr. D. F. Langa, for their guidance to analysis the results and writing the thesis.
- I would also like to express my appreciation to my colleagues, Mr. M. Y. A. Ismail to help me in the analysis my results and Mr. T. M. Mohlala for his assistance with RBS measurements.
- I also wish to acknowledge and thank students and staff in the department of physics, my friends both near and far for their support, assistance and encouragement through the highs and lows of this study.
- I would also like to express appreciation to my supportive friends in South Africa, especially in Pretoria, who was very kind and did not leave me alone during life here.

Finally, I would like to recognize the unwavering support and patience of my mother, sister, brothers, and other family members during this endeavour.

"By the way, thank you God for all your generosity given to me during my life."

LIST OF ABBREVIATIONS

kWh – Kilo Watt Hour

EJ – Exajoule = 10^{18} joules

FPs – Fission Products

NFC – Nuclear Fuel Cycle

TRU – Transuranic

SNF – Spent Nuclear Fuel

HLW – High Level Waste

LLW – Low Level Waste

ILW – Intermediate Level Waste

GC – Glassy Carbon

keV – Kilo Electron Volt

RBS – Rutherford Backscattering Spectrometry

SEM – Scanning Electron Microscopy

Eu – Europium

U235 – Uranium 235

TEM – Transmission Electron Microscopy

ZBL – Ziegler, Biersack, Littmark

MeV – Mega Electron Volt

SSD – Solid State Detector

SBD – Surface Barrier Detector

He – Helium

CCD – Charged Couple Device

UV – Ultra Violet

FWHM – Full Width at Half Maximum

SEs – Secondary Electrons

SE1 –Scattered Electrons (the first group)

UP – University of Pretoria

DAQ – Data Acquisition

nA – Nano Ampere

BWF – Breit-Wigner-Fano

TK – Tuinstra-Koenig

SiC – Silicon Carbide

DLC – Diamond-Like Carbon

DLC:H – Hydrogenated Diamond-Like Carbon

ta:C – Tetrahedral Amorphous Carbon

TABLE OF CONTENTS

TABLE OF FIGURES

LIST OF TABLES

CHAPTER 1

INTRODUCTION

People consume energy in many different forms. All aspects of energy we are using virtually arise from atoms, either from electronic interactions, i.e. chemical compound formation (e.g. burning of fossil fuel) or from atom, i.e. from nuclear reactors. Stars including the sun get energy from nuclear reactions. Then we can use this energy not only after months or years by burning the wood which has been stored in plants through photosynthesis but also after million years of geologic and chemical activation underground, which changes the organic material into fossil fuels, e.g. coal, oil, or gas. The only one other natural source of energy is that of geothermal energy, which has its origin from radioactive elements in the core of the earth.

Our demands to consume energy are unlimited but its traditional sources are not. Mankind is using the limited reserves of fossil fuels several million times faster than they are produced. Along with consuming energy we need to be aware of the consequences of misusing these traditional sources on environment conditions. Carbon dioxide (a major "greenhouse" gas) concentration in the atmosphere has increased about 40% since the inception of the industrial revolution. This has led to global warming and resulting climate change [Ape10].

Unlike in regions with decrease demand, the consumption of power by people, especially electricity, increases in general. This encourages the development of all locally accessible and appropriate electricity generating options, including nuclear power [Ahe11].

The great advantage of nuclear power is the capability of production immense energy from a small amount of fuel with a very small carbon footprint. Nuclear fission, presents an amount of energy (by modifying matter to energy) which is several million times more energetic than chemical burning that only breaks chemical bonds. According to Einstein's relation, $E = \Delta m\, c^2$, where c equals the speed of light, nuclear fusion and nuclear fission leads to a mass loss Δm, between the initial product and the final product. As a result, the mass of 1 kg can be changed into an energy of about 9×10^{16} J or 25×10^9 kWh. This is equivalent to the burning of 3 million tons of coal.

Currently, the production of electrical energy by nuclear fission is applied in some countries, while methods to achieve controllable and continuous nuclear fusion are still being studied.

As can be seen in Figure 1.1, the prediction for global total primary energy consumption growth is on average 0.11% per year for the period 2000-2100. Nuclear energy's proportion will grow from 2% in 2000 to 13% in 2100. This represents the highest growth of all energy types [Vai08].

[The Exajoule (EJ) is equal to one quintillion (10^{18}) joules].

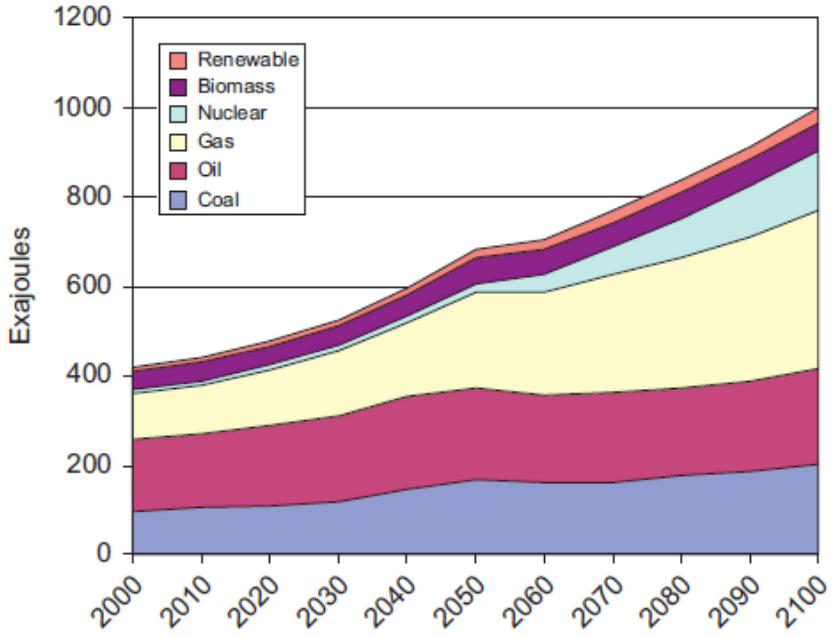

Fig. 1.1. Predicted global total prime energy consumption by fuel type as modeled by World-TIMES. Taken from [Vai08]

Electricity is the most popular form of energy consumption in the world. It is termed a secondary source of energy, i.e. it has to be produced using main energy sources like coal, natural gas, or nuclear reactions. Experts predict that in 2100, electricity generation will increase to 40% compared 2000. Figure 1.2 indicates predicted electricity production from the different energy types for the period 2000 to 2100. In this figure nuclear production is predicted to reach 62 EJ in 2100 representing 25% of the total electricity production [Vai08].

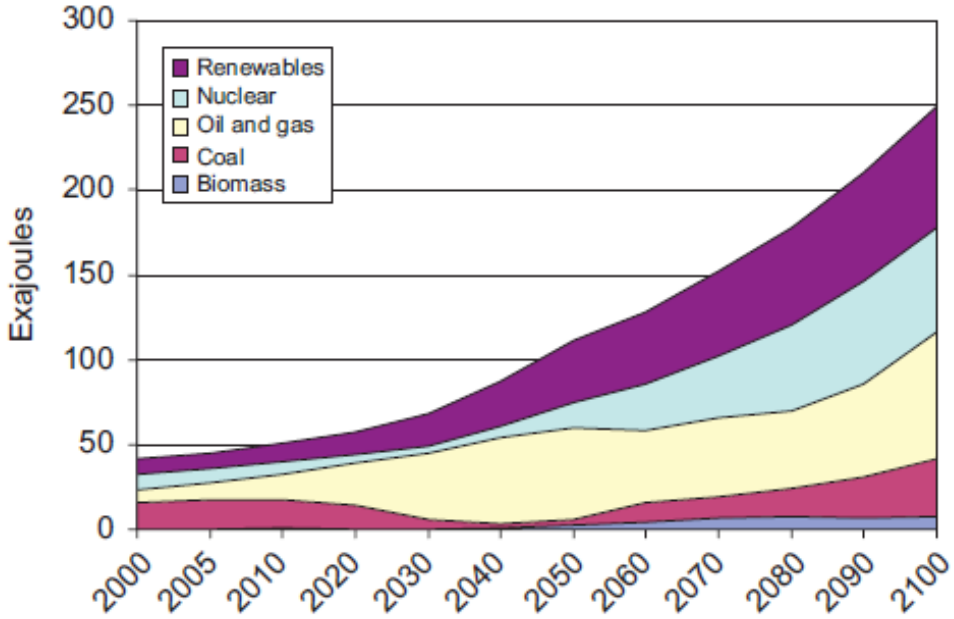

Fig. 1.2. Electricity produced on basis of all sources of energy between (2000-2100). Obtained from [Vai08]

Nuclear power certainly has its advantages and disadvantages like any other aspects of energy powers. Some of them are:

Advantages of nuclear energy: [Ahe11]

- The relatively low cost
- Low levels of pollution when using safe waste management conditions
- High levels of fuel availability
- Supporting peak power consumption
- Low levels of radiation exposure per person
- An established technology

Disadvantages of nuclear energy: [Dit12]

- Harmful radiation emission.
- Finite ore resources
- Large installations
- Long-term storage containers for high-level pollutants
- Pollution of groundwater sources via nuclear wastes

1.1 RADIOACTIVE WASTE

Since nuclear materials are being used in many applications such as in industry (e.g. to generate the electricity), medicine science (e.g. diagnosis and cure of disease), etc., radioactive waste remains in all these applications. The International Atomic Energy Agency (IAEA) defines radioactive waste as "any material that contains or is contaminated by radionuclides at concentrations or radioactivity levels greater than the exempted quantities established by the competent authorities and for which no use is foreseen" [IAE09].

Some nuclear fission products (FPs) and their chemical components are toxic, which means that this must be taken into consideration for safety purposes and for storage. Nuclear waste could be hazardous from ten to several hundreds of thousands of years. This obviously threatens future generations. Many industries are producing dangerous waste. The nuclear industry can develop technology to manage the nuclear waste safely. It is necessary to be done to remove the risk to present and future generations. In order to simplify management and cost of radioactive waste, radioactive waste is classified according to the amount and character of its radioactivity. The concepts of these properties for the safe movement, transport, storage and disposal are also considered. Nuclear waste radioactivity decreases gradually with time. The radioactivity of high-level wastes reduces to the same level as initial mined uranium with time (hundreds of thousands of years). This is the reason why so much research is done to find suitable container materials and a proper design to store high level waste for such a long time, see for example [Ojo07].

1.1.1 SOURCES OF RADIOACTIVE WASTE

All agricultural, medical, industrial, household and human products contain naturally occurring radioactive nuclides [Tan90].

Generally radioactive wastes come from three main sources:

- Spent nuclear fuel cycle (NFC) for generating power and military uses
- Non-NFC institutes comprising of research and medical institutes, hospitals, industries, mining products and etc.
- Accidents (like Chernobyl and Fukushima disasters)

1.1.2 PHYSICAL STATE OF RADIOACTIVE WASTE (RADWASTE)

Radwaste materials can exist in all three physical states: [Tan90]

- Gaseous waste; Gaseous wastes arise from gaseous channels in reprocessing plants and nuclear power plants. This waste usually contains airborne radionuclides such as ^{85}Kr, ^{3}H, ^{14}C, and ^{131}I.
- Liquid waste; Aqueous radioactive wastes are generated within nuclear reactor operations and during the use of radio-isotopes by industries and institutions. Liquid discharge from different parts of a nuclear reactor plant or its steam generators is also liquid waste.
- Solid waste; Solid nuclear waste produced by the nuclear power station such as mining and milling of radioactive ores such as uranium and thorium. Furthermore, equipment and structures of daily trash such as paper, gloves, plastic containers, radioactive resin and chemical sludge, spent filter cartridges and etc., which were exposed to nuclear materials are supposed as solid waste [Tan90].

1.2 NUCLEAR WASTE TYPE

Categorizing waste types for radioactive waste is derived from their origin (i.e. army or commercial wastes), the type of materials [transuranic (TRU) or spent nuclear fuel (SNF) wastes)] and the level of radioactivity (e.g. high- or low-level wastes). The term ‘‘nuclear waste’’ includes five waste categories. The first three i.e. spent nuclear fuels, high-level wastes, and transuranic wastes, are the most significant and most radioactive; the rest of two are low-level wastes and uranium mill tailings [Tan90].

1.2.1 SPENT NUCLEAR FUEL (SNF)

SNF implies fuel rods which were irradiated in a nuclear reactor plant, to have high active and short-lived fission products (such as cesium and strontium). SNF contains highly radioactive nuclei that are found in the center of a nuclear reactor following irradiation. Commercial nuclear fuel, research institutions, industrial users and military activities are mentioned as sources of this type of nuclear waste [Tan90].

1.2.2 HIGH-LEVEL WASTE (HLW)

Extremely radioactive material which originates from the reprocessing from SNFs, or the chemical processes that separates fuel rods into uranium and plutonium and other elements is termed high-level waste. HLW is highly radioactive, and can also include dangerous chemicals and toxic heavy metals. Since this waste type has a life time of about thousands of years, it is needed to be held in safe storage containers until its radioactivity level reduces to safe levels [Tan90].

Aqueous HLW from reprocessing of SNF contain more than 50 elements which can be divided four groups:

- Fission products (FP) such as Cs, Sr, Tc, I, Pm, Sm, Eu.
- Corrosion products such as oxidized Fe, Cr, Co, etc. including activated radionuclides ^{51}Cr, ^{59}Fe, $^{58,60}Co$, etc.

- Minor actinides (MA) such as U and transmutation products such as Pu, Am, etc.
- Process pollutants such as components of Na, K, Li, Ca, etc. including organic process chemical such as phosphate [Ojo07].

1.2.3 TRANSURANIC WASTE (TUR)

Transuranic wastes pertain to any type of waste which have alpha-emitting isotopes of more than 100 nanocuries per gram of waste (a unit of radioactivity, equal to 3.7×10^{10} disintegrations per second) with half-lives of more than twenty years, excluding high-level waste. TUR wastes, from transuranic elements, are produced during the generation of nuclear weapons. A TUR element is an element with an atomic number more than uranium, i.e. with atomic number 92 or larger. Some TUR elements, such as plutonium, have half-lives of thousands of years. Decontamination and decommissioning of nuclear fuel cycle, some industries and institutions, military activities are placed as a source of generating this waste type [Tan90].

1.2.4 LOW-LEVEL WASTE (LLW)

Among all categories of radioactive wastes, LLWs are any type of radioactive waste which does not belong to one of the above categories, particularly not TUR elements. LLWs have a very low percentage of radioactive material to the total volume of the waste. Most LLWs are buried in shallow cavity sites. Some waste products from hospitals, research laboratories and industrial users belong to this classification [Tan90].

1.2.5 URANIUM-MILLING TAILINGS

The great volume of materials remaining after the mining and milling procedures of uranium ores is called as uranium-mill tailings. Although uranium-mill tailings are not categorized as waste, they are hazardous to the environment. Tailings emit radon and are often contaminated with toxic heavy metals [Tan90].

1.3 NUCLEAR WASTE STORAGE

The safety of nuclear waste storage is a very significant issue for the usage of nuclear energy in many applications in industry, medicine, research etc. Many investigations have been done from a safety point of view such as mechanical, chemical, geological and physical studies. These studies can be divided into two parts, surrounding environment (geological position and sediment) and the storage container itself. The purpose of all investigations is to find materials with high capability to containing radioactive wastes in normal and abnormal situations [Alh12].

Nuclear waste management or radioactive waste disposal is a serious part of nuclear power production. There are some very important and strict rules which must be followed by nuclear power plants and companies to assure that all nuclear wastes are buried safely, carefully and without any threat to humans, animals and plants. Nuclear waste can have disastrous effects on life, e.g. resulting in cancer, leading to genetic problems, etc. The primary purpose of management and disposal of radioactive wastes is protecting people and environment. It means isolating or diluting the waste in order to reduce the level of radioactivity and preventing the leakage of any harmful radionuclides to the atmosphere and environment [Ojo14].

1.3.1 RADIOACTIVE WASTE MANAGEMENT ACTIVITIES

Management of nuclear wastes includes the following activities; processing, carrying, packaging, transportation, storage, disposal and decontamination [Tan90].

- To transfer spent nuclear fuel, scientists and engineers differentiate between two main types of storage: wet and dry. Wet storage pools include placing spent nuclear fuel (SNF) in pools of water made of concrete and lined by stainless steel. Dry storage of SNF just works for rods which have had enough time to cool down to a level where it no longer needs to be held in water. For wet storage this process is different. In this case gas (helium or nitrogen) is replaced by water as a coolant, and concrete or metal as a radiation barrier. Fuel should be stored in wet pools for many years before it gets sufficiently cool for dry storage. Usually these pools are inside reactor sites. Metal tubes and cylinders are used for dry storage vaults to store fuel [Tan90].

- Accumulation of intermediate-level waste (ILW) and high-level waste (HLW) is an issue which needs to be investigated in more detail. Most disposal management options have been investigated for high-level waste.
- Low-level and ILW have the highest amount of radioactive waste. Most low-level waste (LLW) is typically transferred straight to land-based disposal units to be followed by packaging for long-term management. This means that the majority of all of the waste types (~90% by volume), are satisfactory disposed [Tan90].

Before discussing disposal options, some options of reprocessing fuel will be described briefly.

1.3.2 RECYCLING

Recycling means reprocessing and recovery of wastes for reuse. Reprocessing of used fuel to recover U-235 (as reprocessed uranium) and Pu (plutonium) avoids the wastage of a precious resource. As a spent fuel (e.g. uranium or thorium), these isotopes can be reprocessed and loaded into another reactor as fuel. Nuclear waste is recyclable. However, it should be transported in containers for movement [Ojo14]. Figure 1.3 shows a schematic diagram of the fuel cycle (recycling and reprocessing).

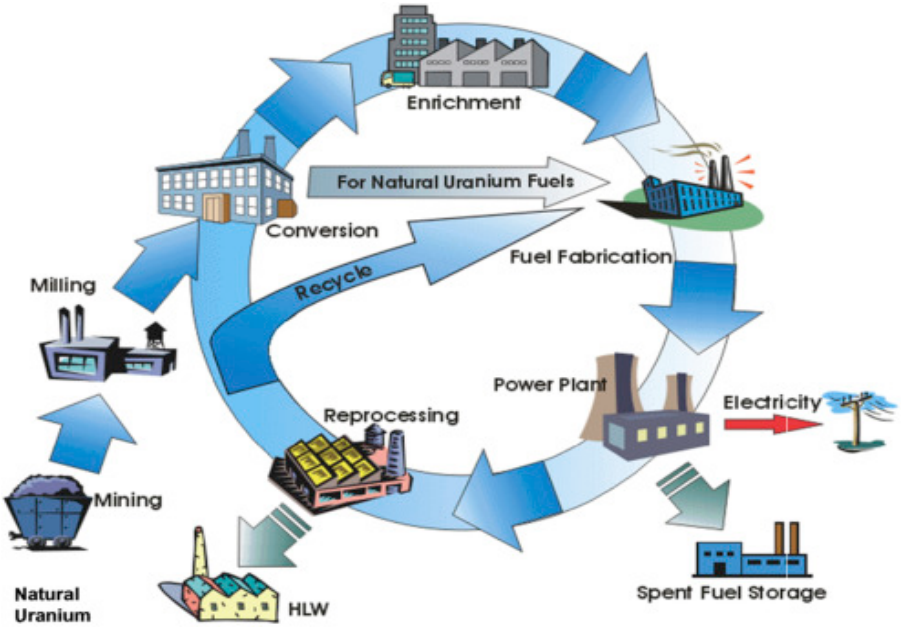

Fig. 1.3. A schematic diagram of a nuclear fuel cycle. Obtained from [Nat17]

1.3.3 WASTE MINIMISATION

This is a process to reduce the amount and activity of nuclear materials to as low a level as reasonably achievable. It can be applied in all steps of processing from the nuclear power plant design through operation to decontaminating [Ojo14].

1.3.4 PROCESSING AND IMMOBILISATION

The processing of nuclear wastes such as pretreatment, treatment and condition, changes their characteristics. Immobilisation reduces the potential for dispersion or migration of contaminants including radionuclides. In any immobilization process, where radioactive materials are used, the process and operational conditions can become complicated. Particularly if it is operated remotely and equipment maintenance is required. Conditioning means those operations which produce a waste package suitable for handling, transportation, storage and disposal. The choice of the immobilization technology depends on the physical and chemical nature of the waste. The other factor is the acceptance criteria for the long term storage and disposal facility to which the waste will be forwarded [Ojo14].

As technology has developed in the last decade, especially dry-cask storage, it provides confidence that wastes from commercial reactors can be stored safely for a long time at current sites. Two options are currently accepted as suitable nuclear wastes disposal sites. These two options are:

1) Near-surface disposal on ground level, or in cavities underneath the ground level (in tens of meters of depths).

2) Deep geological disposal (between 250-1000 meter for mined repositories, and 2000-5000 meter of depths for nuclear waste) [Lou02].

A nuclear waste container consists of a multi-layer which is in contact with the waste. It is designed to resist most of the damage caused by the penetrating forms of radiation. The internal structure of transport containers (using multi-purpose containers) is being designed to maintain separation of different types of fuel or from different sources. Finally, the external structure is designed to maintain containment of the waste in accident conditions. Figure 1.4 illustrates a typical transport container which is employed for used fuel.

Other ideas for disposal:

- Long-term above ground storage
- Disposal in outer space (proposed for highly concentrated wastes)
- Disposal in the ocean
- Sub-seabed disposal
- Disposal in iceberg, glaciers (proposed for heat generating wastes)

To see the details please refer to [Wor17].

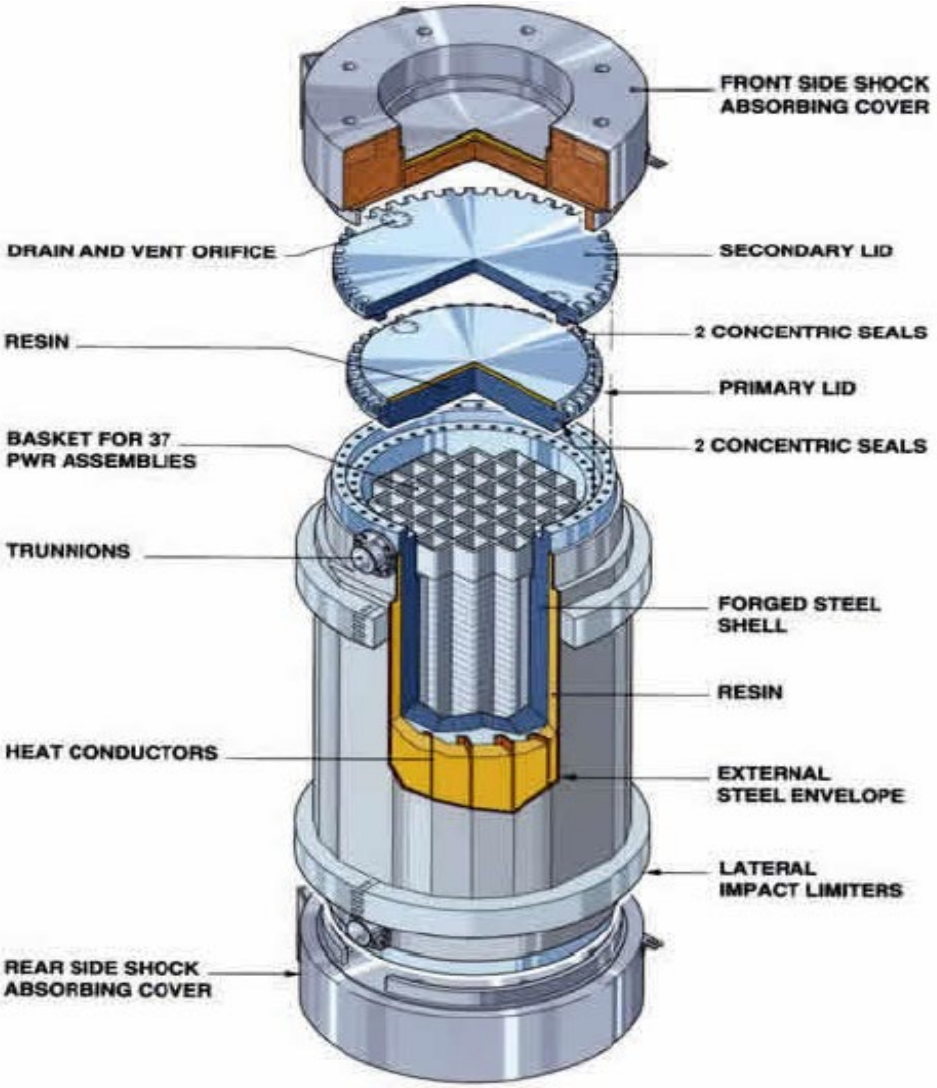

Fig. 1.4. A typical transport canister employed for used fuel. Taken from [Wor17]

1.4 RESEARCH JUSTIFICATION

To choose waste container materials, the design and backfill, and material depend on the waste type to be contained and the nature of the host rock-type available. The container systems are designed to withstand a wide range of severe environmental conditions, such as earthquakes, flooding, extreme temperatures, and tornadoes. The nuclear waste must be placed in suitable storage containers for either short- or long-term storage. The containers must withstand the environment degradations (e.g. accident, corrosion-related processes) on their inner surfaces which are in contact with immobilized nuclear waste. Thus, the material for construction of the canister must be capable of withstanding atmospheric corrosion, have high density, high thermal stability, low thermal conductivity, etc. [All88].

As mentioned above, for properties of cask materials, the most of materials which are being used as the nuclear waste container should be trustworthy. Some elements are not suitable to use as long time storage cask. Some container materials and their shortcomings are listed below:

- Titanium: this material with some of its alloys are mechanically strong and have good corrosion resistance, but they can experience brittle failure and they are expensive.
- Copper: it is sufficient stable, however, it is well known to be poor in brine and radiation environment.
- Iron: it is less prone to disaster failures, but not good enough to be a corrosion resistant material.
- Stainless steel: it has good mechanical properties and is really suitable in corrosion resistant tools. However, catastrophic failure is possible via stress-corrosion cracking [Yim00].

All transportation containers should be very robust, and must be designed to withstand a similar set of extreme events or conditions. The construction materials should have long term stability, corrosion resistance, highly thermal resistance, and etc. From this point of view, glassy carbon (GC) could be an appropriate material to fabricate good waste containers from. It will be explained more in detail in Chapter 2.

1.5 RESEARCH SCOPE

The ultimate scope of this study is the investigation of diffusion of europium in glassy carbon. For this purpose, glassy carbon was implanted with europium ions at 250 keV. One of the major problems in the dry method of nuclear storage is degradation over time due to heat. In order to investigate if glassy carbon is able to withstand the heat treatment behavior, the implanted glassy carbon was annealed at different temperatures. The microstructure of the samples was monitored after ion implantation and annealing at different temperatures using Raman spectroscopy. We the diffusion behavior of europium in glassy carbon due to heat treatment using Rutherford backscattering spectrometry (RBS). The changes in the surface topography of glassy carbon were investigated using Scanning Electron Microscopy (SEM).

1.6 EUROPIUM

Europium is a white/silvery metal. It is the least dense, softest, and the most volatile member of the lanthanide series, and reacts easily with water and oxygen [Pot00] as well as carbon to form a carbide.

One of the primary uses of europium is to apply it in nuclear reactor control rods. When a fissile nuclide such as U-235 atom fissions, it generally splits into two large fragments asymmetrically which could include one of the three europium isotopes and two or three neutrons. In order to control this fission reaction, europium isotopes are used in nuclear reactor control rods [May13].

The other application of europium which is often studied is as a dopant in laser materials europium oxide also serves as a phosphor activator. For example, europium (Eu^{+3} has a large emission band centered near the one of the primary colors i.e. red (612nm)) and consequently has been used as a phosphor in television tubes and panel displays [Pol02], [Que14], [Che02].

Despite the low concentration of europium compared to other fission products, (Figure 1.5), it has important radiological health concerns if it is released into the environment [Dwa16]. Europium can be taken into the body by breathing. It is toxic to lungs and mucous membrane if inhaled. It is also corrosive and burn skin [Moh17].

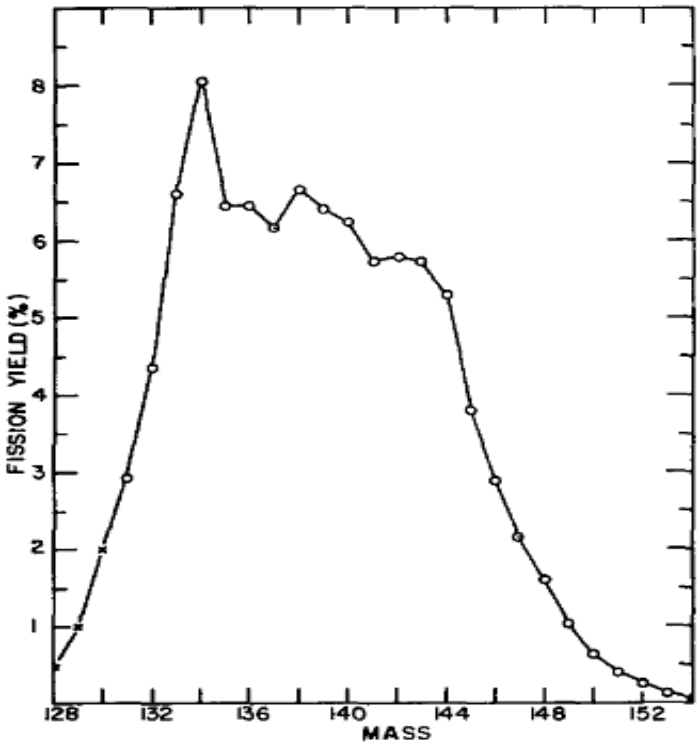

Fig. 1.5. The yield of fission products of U-235 thermal neutron fission. Taken from [Far62]

If europium reaches the blood, 40% it will deposit in the liver, and another 40% will deposit on the bone surface, where it can be absorbed by the bone cells. An additional 6% of the absorbed europium will deposit in the kidneys.

Thirty four Eu isotopes from A = 130 to 165 have been discovered so far, which have half-lives from few seconds to some years. The dates when these isotopes were discovered can be seen in Figure 1.6. The radioactive Eu isotopes can be produced by fusion-evaporation reactions, light-particle reactions, neutron-induced fission, spontaneous fission and etc. [May13].

In nature europium occurs as two stable isotopes. Eu-153 accounts for 52% of natural europium, and Eu-151 makes up the remaining 48%. Among the discovered isotopes, just three ones i.e. Eu-152, Eu-154, and Eu-155 are produced as fission products of uranium and plutonium. They have half-lives of about 13.5 years (with 28% of the gamma radiation), 8.6 years (with 40% of the beta radiation) and 4.7 years (with 31% of the beta radiation), respectively [May13], [Jul57], [Nic08], [Sab14].

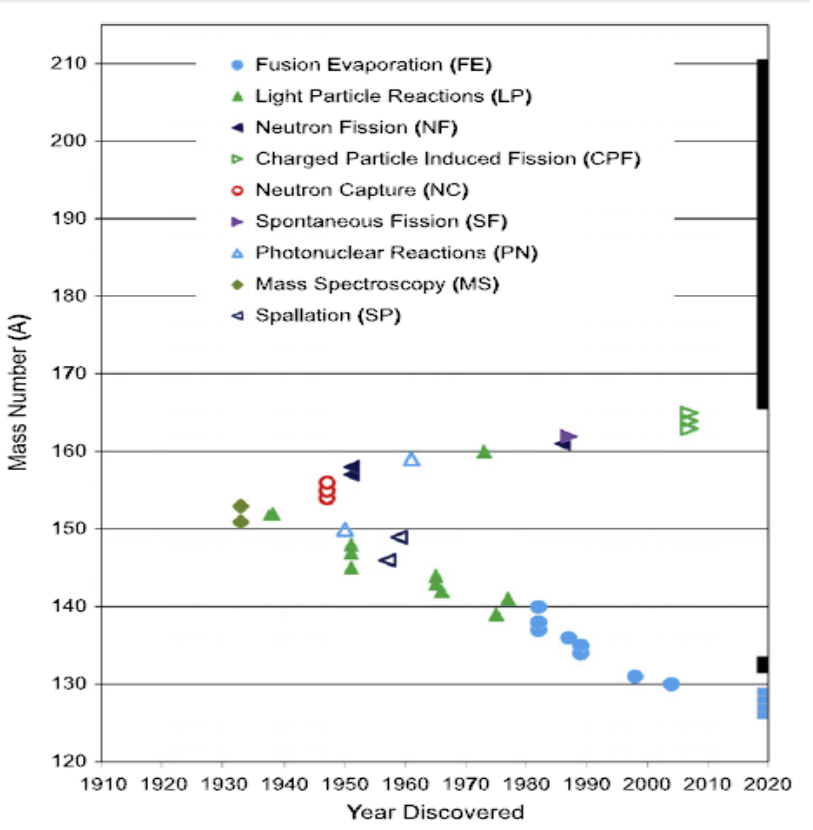

Fig. 1.6. Discovered Europium isotopes as a function of date. Obtained from [May13]

1.7 THESIS OUTLINE

This thesis consists of 8 chapters. Chapter 1 is the Introduction and it gives a general overview of nuclear power and nuclear wastes. The chapter also discusses the methods and challenges of storage and management of nuclear wastes. Chapter 2 discusses carbon and its allotropes, the structures of the allotropes of carbon (with respect to their sp^2 and sp^3 content). The structure and features of glassy carbon are also discussed in this Chapter. The theory of ion implantation and diffusion are discussed in Chapters 3 and 4, respectively. Chapter 5 gives a general overview of the analysis techniques (Rutherford backscattering spectrometry, Raman spectroscopy and scanning electron microscopy) used during the study. The experimental procedures including the annealing processes are discussed in Chapter 6. The results and discussion are presented in Chapter 7. Chapter 7 discusses the experimental data obtained for the europium implanted in glassy carbon. Finally, Chapter 8 is the conclusion from the results.

REFERENCES

[Ahe11] J. F. Ahearne, "Prospects for nuclear energy", Energy Economics, 33(4), pp. 572–580, 2011.

[Alh12] O. Alhassanieh, Z. Ajji, "Migration of strontium, cesium, europium and uranium from poly (methyl styrene) and polystyrene-phosphate composites prepared using gamma radiation", Nukleonika, pp. 369–374, 2012.

[All88] C. C. Allen, M. I. Wood, "Bentonite in nuclear waste disposal: A review of research in support of the Basalt Waste Isolation Project", Applied Clay Science, 3(1), pp. 11–30, 1988.

[Ape10] N. Apergis, J. E. Payne, "A panel study of nuclear energy consumption and economic growth", Energy Economics, 32(3), pp. 545–549, 2010.

[Che02] W. Chen, G. A. Joly, C. M. Kowalchuk, J. O. Malm, Y. Huang, J.O. Bovin, "Structure, Luminescence, and Dynamics of Eu2O3 Nanoparticles in MCM-41', The Journal of Physical Chemistry B, 106(28), pp. 7034–7041, 2002.

[Dit12] M. Dittmar, "Nuclear energy: Status and future limitations", Energy, 37(1), pp. 35–40, 2012.

[Dwa16] S. S. Dwaraknath, G. S. Was, "The diffusion of cesium, strontium, and europium in silicon carbide", Journal of Nuclear Materials, 476, pp. 155–167, 2016.

[Far62] H. Farrar, R. Tomlinson, "Cumulative yields of the heavy fragments in U-235 thermal neutron fission", Nuclear Physics, 34(2), pp. 367–381, 1962.

[IAE09] IAEA "Predisposal Management of Radioactive Waste General Safety Requirements", General Safety Requirements Part 5, pp. 1–38, 2009.

[Jul57] J. O. Juliano, F. S. Stephens JR. "Decay of Europium-154", Physical Review, 108(2), 1957.

[Lou02] H. Louberga, S. Villeneuve, M. Chesney, "Long-term risk management of nuclear waste: a real options approach", Journal of Economic Dynamics & Control, 27, pp. 157–180, 2002.

[May13] E. May, M. Thoennessen, "Discovery of samarium, europium, gadolinium and terbium isotopes", Atomic Data and Nuclear Data Tables, 99(1), pp. 1–21, 2013.

[Moh17] T. M. Mohlala, T. T. Hlatshwayo, M. Mlambo, E. G. Njoroge, S. V. Motloung, J. B. Malherbe, "Migration behaviour of Europium implanted into single crystalline 6H-SiC", Vacuum, 141, pp. 130–134, 2017.

[Nat17] R. Natarajan, "Reprocessing of spent nuclear fuel in India: Present challenges and future programme", Progress in Nuclear Energy, 101, pp. 118–132, 2017.

[Nic08] A. L. Nichols, D. L. Aldama, M. Verpelli, "U235 cumulative fission yields for selected fission products", Handbook of Nuclear Data for Safeguards: Database Extensions, pp. 105–106, 2008.

[Ojo07] M. I. Ojovan, W. E. Lee, "New developments in glassy nuclear wasteforms", Nova Science Publishers, 2007.

[Ojo14] M. I. Ojovan, W. E. Lee, "An Introduction to Nuclear Waste Immobilisation", 2014.

[Pol02] V. G. Pol, R. Reisfeld, A. Gedanken, "Sonochemical synthesis and optical properties of europium oxide nanolayer coated on titania", Chemistry of Materials, 14(9), pp. 3920–3924, 2002.

[Pot00] R. Pottgen, D. Johrendt, "Equiatomic intermetallic europium compounds: Syntheses, crystal chemistry, chemical bonding, and physical properties", Chemistry of Materials, 12(4), pp. 875–897, 2000.

[Que14] A. Quesada, A. del Campo, J. F. Fernández, "Sintering behaviour and translucency of dense Eu_2O_3ceramics", Journal of the European Ceramic Society, 34(7), pp. 1803–1808, 2014.

[Sab14] A. Sabau, Y. Pipon, N. Toulhoat, C. Lomenech, N. Jordan, N. Moncoffre, A. Barkleit, N. Marmier, V. Brendler, S. Surblé, E. Giffaut, "Interaction of europium and nickel with calcite studied by Rutherford Backscattering Spectrometry and Time-Resolved Laser Fluorescence Spectroscopy", Nuclear Instruments and Methods in Physics Research, Section B: Beam Interactions with Materials and Atoms, 332, pp. 111–116, 2014.

[Tan90] Y. S. Tang, J. H. Saling. Radioactive waste management", HPC, 1990.

[Vai08] K. Vaillancourt, M. Labriet, R. Loulou, J. P. Waaub, "The role of nuclear energy in long-term climate scenarios: An analysis with the World-Times model", Energy Policy, 36(7), pp. 2296–2307, 2008.

[Wor17] World nuclear association "Storage and Disposal Options for Radioactive Waste", Available at: http://www.world-nuclear.org/, 2017.

[Yim00] M. Yim, K. L. Murty, "Materials issues in nuclear-waste management", Jom, 2000.

CHAPTER 2
CARBON AND ITS ALLOTROPES

Carbon element in different shapes has been existed in humans' life as charcoal and soot since ~5000 BC before the term "element" was coined. It was obtained from wood and has been applied in some cases such as the production of iron [Kru10].

Over 95% of all known chemical compounds are carbon compounds. Carbon is an adaptability element in periodic table. For example the two most famous carbon allotropes like graphite and diamond illustrate different properties as a soft solid material and hard solid material, respectively [Fal07]. Natural graphite and diamond are only two polymorphs (allotropes) of carbon which exist as minerals on earth. The other carbon allotropes are made by mankind and derive from carbonaceous procedures [Pie93].

Carbon is capable to bond to both electronegative and electropositive elements. It can also bond itself (rings, chains, etc.) without limits through single (average bond energy of ~ 350 kJ/mol), double (with average bond energy ~ 610 kJ/mol) and triple bonds (average bond energy ~ 840 kJ/mol. It is a fairly inert element. However in contrast to the other elements of the IV group, carbon tends to contribute all its four valence electrons to the binding [Kru10], [Fal07].

Less than 70 years ago, Franklin showed that carbon is produced by solid-phase pyrolysis of organic materials in two determined classes [Har05]. The first one was called "graphitizing" carbon which is called "soft carbon" and tends to be soft, with a high density. It is prepared by prolonged heat treatment in range of 2200 ^{o}C - 3000 ^{o}C and readily transforms into crystalline graphite. The second one was "non-graphitizing" and is called "hard carbon" with low density. It cannot be developed to significant graphite structure even at high temperatures (~ 3000 ^{o}C). Franklin in 1951, attempted in her paper to describe a model for the structure of graphitizing and non-graphitizing carbons [Fra51]. Illustrated structural models of Franklin can be seen in Figure 2.1.

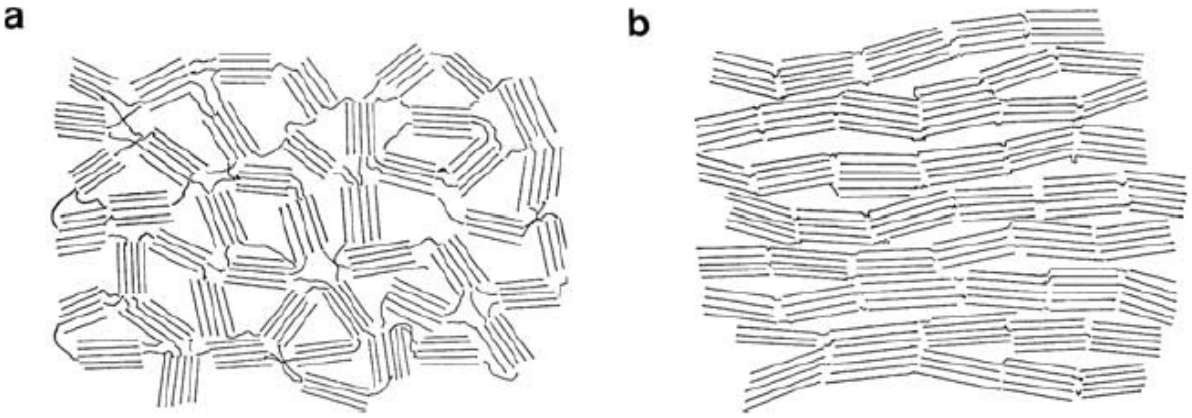

Fig. 2.1. Franklin's model of (a) non-graphitizing and (b) graphitizing carbons. Taken from [Har05]

Figure 2.2 shows the distinction between graphitizing (graphite-like) and non-graphitizing (prepared by pyrolysis of sucrose) carbons using transmission electron microscopy (TEM) [Har05].

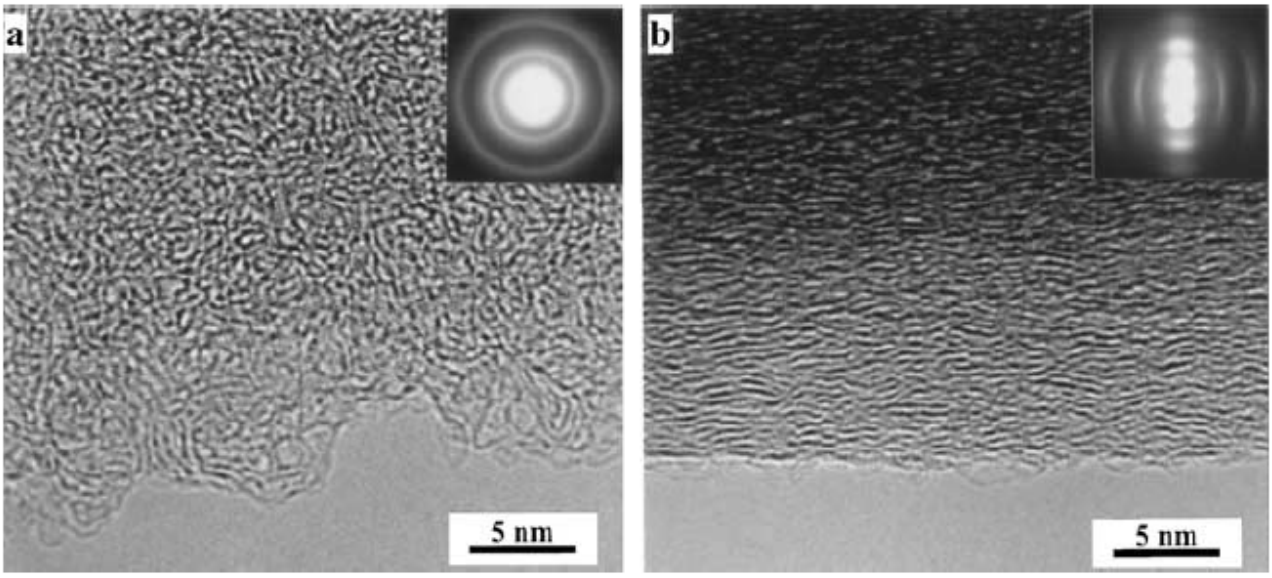

Fig. 2.2. HRTEM images of (a) non-graphitizing carbon prepared in nitrogen at 1000ºC, (b) graphitizing carbon prepared by pyrolysis of anthracene at 1000 ºC. Taken from [Har05]

[Anthracene is a colorless crystalline aromatic hydrocarbon obtained by the distillation of crude oils and used in chemical manufacture.] The general properties of carbon is given in Table 2.1.

Table 2.1. General properties of carbon. Mostly taken from [Pie93]

Name	Carbon
Symbol	C
Atomic number	6
Atomic mass	12.0107 amu
Boiling point	Graphite = 4287ºC
Melting point	3500 ºC
Classification	non-metal
Density (at room temperature) (Krueger, 2010),(Pierson, 1993),(Harris, 2005)	Glassy Carbon = 1.42 g/cm^3 Diamond = 3.35 g/cm^3 Graphite = 2.26 g/cm^3
Crystal structure	Cubic (diamond) Hexagonal (diamond and graphite) Rhombohedral (graphite)

2.1 CARBON ATOM'S STRUCTURE

Since the atomic number of carbon equals six, these electrons are configured as $1s^2\ 2s^2\ 2p^2$ in ground state. It means that carbon has two valence electrons and it is considered as bivalence. However, bivalency is only found in a few carbon compounds. In most compounds, carbon is tetravalent, i.e. the carbon atom can bond to four other atoms, like carbon (diamond) or hydrogen (methane), etc. [Kru10], [Miy98].

Tetravalency may be explained by the hybridization model. Compared with the chemical bonding energy released in reactions, the difference in energy between the 2s and 2p orbitals is small. Thus, mixing of these orbitals is possible and this leads to the formation of four equivalent hybridized orbitals. On the basis of the degree of hybridization, carbon compounds have different structural

properties. Hybridization of carbon atoms is classified into three configurations namely; sp-hybridized (linear chain), sp^2-hybridized (planar structure) and sp^3-hybridized (three-dimensional tetrahedral networks) [Kru10].

The different hybridizations are discussed below.

2.1.1 SP (DIAGONAL) HYBRIDIZATION

sp hybridization is as a result of merging one s and one p orbital. It consist of two lobes (see Figure 2.3), i.e. s- and p-orbitals. The p-orbital is bigger than s-orbital. The angle between these lobes is 180°. Because of the mutual repulsion of the two sp-orbitals, this leads to a linear molecule [Pie93].

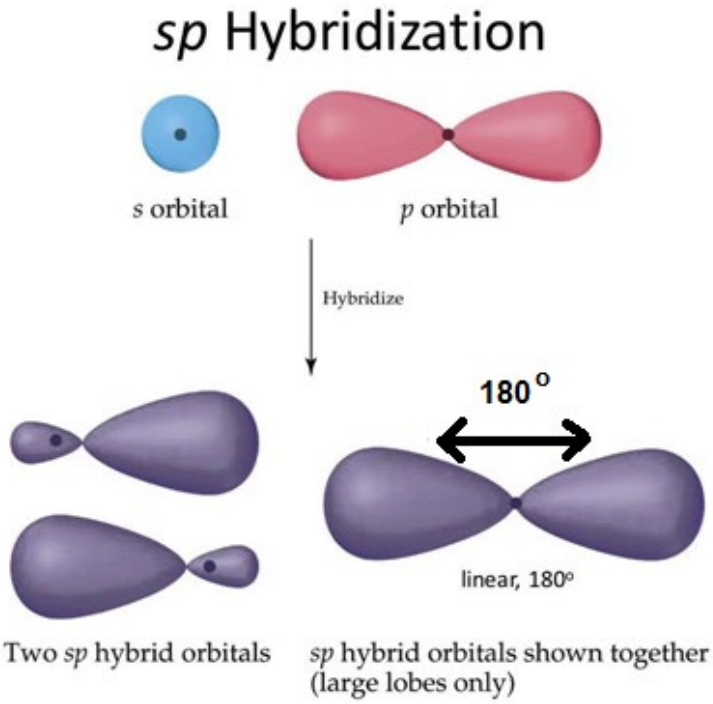

Fig. 2.3. Formation of sp hybridization from 2s- and 2p-orbitals. Taken from [www17]

2.1.2 SP^2 (TRIGONAL) HYBRIDIZATION

Combination of one s-orbital with two p-orbitals (p_x and p_y) results in sp^2 hybridization. All three sp^2 orbitals are in the same plane, presenting a planar assembly. As shown in Figure 2.4, they also have an angle of 120° and a π-bond. There are also σ-bonds which are formed by partial overlapping between two carbon atomic orbitals. The orbitals of sp^2 are the basis of all aromatic compounds and graphitic structures. Considering the p_z-orbital which is perpendicular to the sp^2-hybrid orbitals and a π-bond, crystal structure such as graphite is created [Pes11]. It is shown in Figure 2.5.

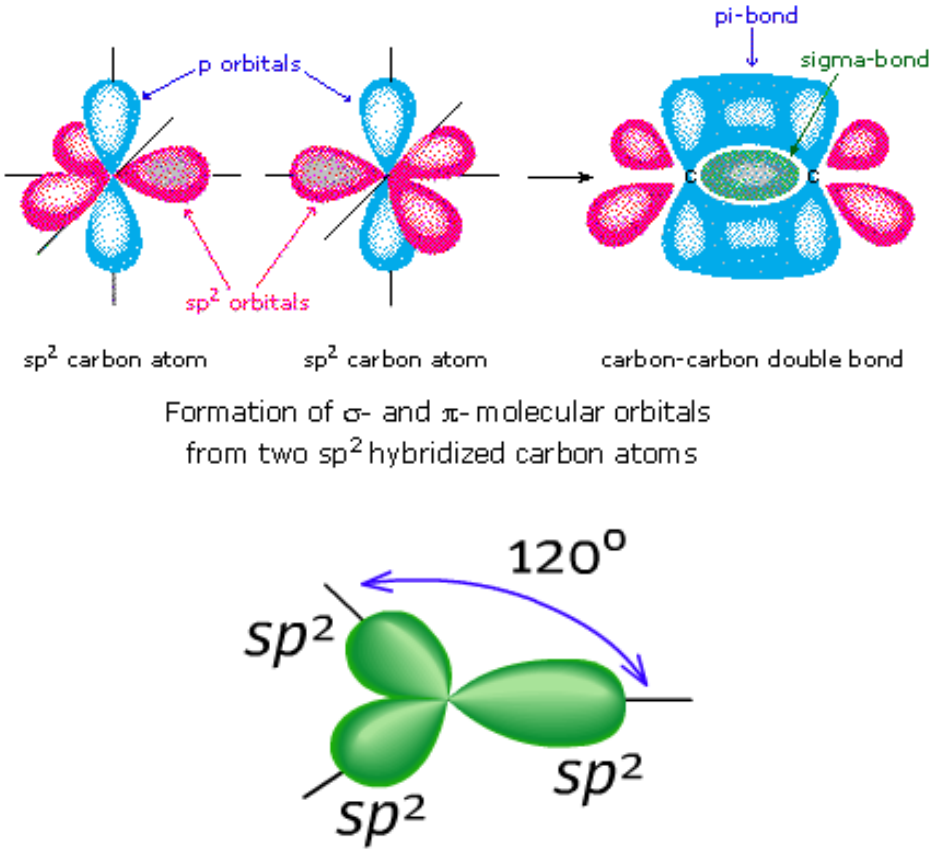

Fig. 2.4. Planar section of the sp^2 orbitals of carbon atom. Taken from [Pes11], [www17]

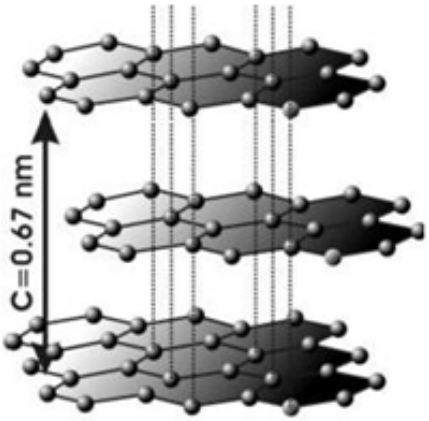

Fig. 2.5. The three dimensional crystal structure of graphite. Taken from [Pes11]

2.1.3 SP^3 (TETRAHEDRAL) HYBRIDIZATION

As mentioned in section 2.1, a carbon atom has six electrons. Four electrons out of six electrons of carbon atom are in the outer shells i.e. 2s and 2p. Since the difference in energy between s-orbital and p-orbital is small, it is possible for one electron from 2s state to be excited into the 2p state. This leads to a mixture of the s-orbital and three p-orbitals (i.e. p_x, p_y and p_z) which introduces a new orbital hybridization. This new hybridization possesses a tetrahedral assembly with four lobes (Figure 2.6) where the angle between any both sp^3 configurations is 109.5° [Pie93], [Pes11].

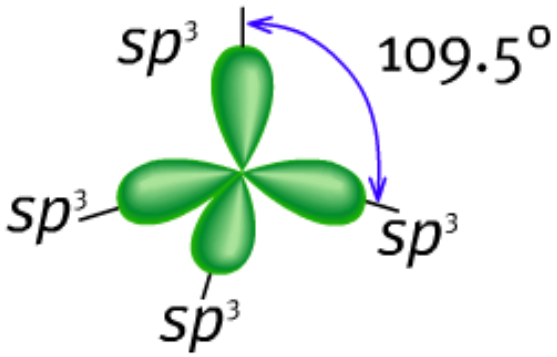

Fig. 2.6. Four sp^3 orbitals in a carbon atom. Taken from [Pes11]

Accumulation of many different three dimensional sp^3 orbital hybridization, makes the lattice structure such as shown in Figure 2.7. The binding strength between any two neighboring carbon atoms is equal in this hybridization. A famous example of this kind of structure is diamond which is well known for its hardness [Pes11].

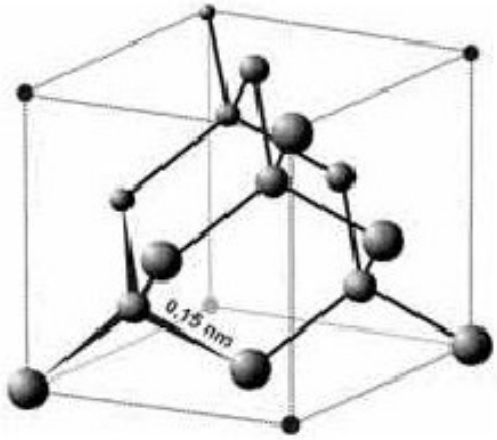

Fig. 2.7. Diamond crystal structure as sp^3 hybridization. Taken from [Pes11]

2.2 CARBON'S ALLOTROPES

In terms of diversity, carbon is really a different and important element compared to the others. This element can introduce several forms of materials which have different physical forms which are known as allotropes (or polymorphs). All of these allotropes (natural and artificial) are made of carbon but having different biological, physical, chemical, thermal and electrical properties [Pie93], [Lin11], [She11]. This is because of the different arrangements of the carbon atomic structure and having sp, sp^2 and sp^3 hybridization ability [Pie93], [He12]. In nature, carbon has three well known allotropes, namely; graphite, diamond and amorphous carbon [She11].

The figure below (Figure 2.8) shows some the carbon allotropes in summary [Fal07]. These allotropes will be described briefly in next sections in this chapter.

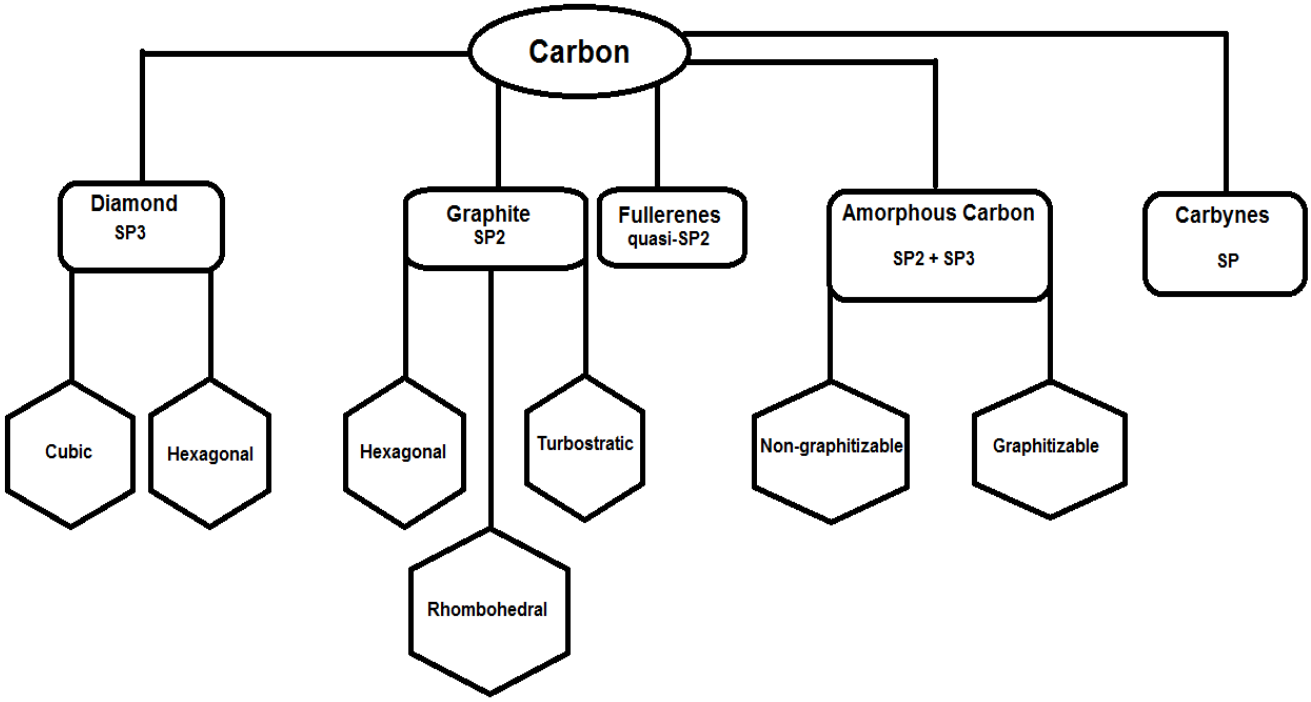

Fig. 2.8. Carbon allotropes. Taken from [Fal07]

2.2.1 GRAPHITE

Graphite is composed of a nearly infinite number of graphene layers which are localized parallel to each other. Each atom bonds to three other carbon atoms and makes a planar hexagon due to sp^2-hybridization. Between the graphene sheets is Van der Waals bonding. There are three forms of graphite; hexagonal, rhombohedral and turbostratic. The common form of graphite is the hexagonal structure formed by ABAB stacking. The rhombohedral structure of graphite is uncommon with its ABCABC stacking. After heat treatment above 1300 ^{o}C the rhombohedral graphite structure transforms into the hexagonal form. Turbostratic is a disordered form of graphite. The graphene layers in turbostratic structure are often randomly rotated to each other resulting in stacking faults [Kru10], [Fal07], [Pie93], [Pau66], [Li 07].

Figure 2.9 shows both hexagonal and rhombohedral and Figure 2.10 shows the turbostratic form of graphite.

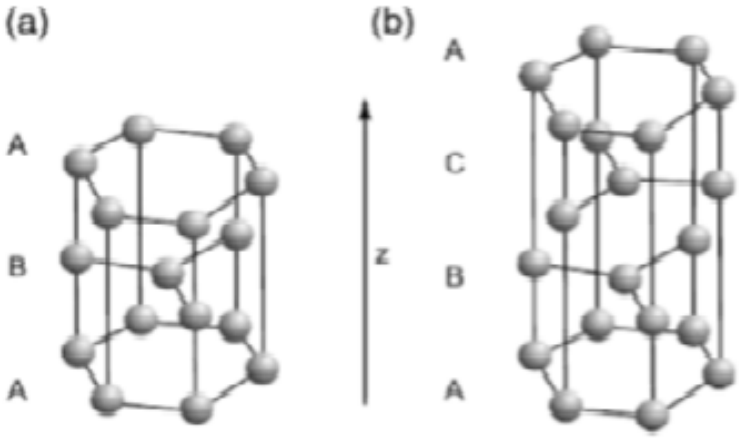

Fig. 2.9. Structures of (a) hexagonal and (b) rhombohedral of graphite. Taken from [Kru10]

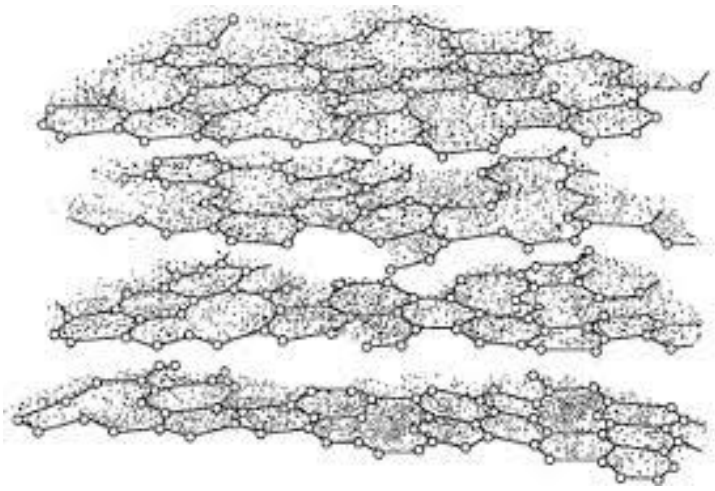

Fig. 2.10. A turbostratic form of graphite. Taken from [Kin11]

2.2.1.1 PROPERTIES OF GRAPHITE

Graphite properties not only strongly depend on its layered structure (i.e. the arrangement of carbon atoms) but also on the Van der Waals force between the layers [Fal07]. Rhombohedral graphite is not as stable as the hexagonal structure. So its layers will shift into a two sequence layer by heat treatment or treatment by acids [Pau66]. Physical properties of graphite was listed below:

Table 2.2. Physical properties of graphite [Pie93]

Crystalline form	hexagonal and rhombohedral
Lattice parameters (hexagonal)	$a_0 = 0.246$ nm $c_0 = 0.671$ nm
Color	Black
Density (at room temperature and in 1atm)	2.26 g/cm^3
Atomic number density	1.14×10^{23}
Atomic volume	5.315 cm^3/mol
Boiling point	4560 ^{o}K
Melting point (in 100 atm)	4200 ^{o}K
Sublimation point	4000 ^{o}K
Heat of vaporization to monoatomic gas	716.9 kJ/mol
Carbon-carbon bond distance	0.141 nm
Pauling electronegativity	2.5
Thermal conductivity (at room temperature)	In ab directions = 398 W/m.K In c direction = 2.2 W/m.K
Binding energy	7.4 eV/C atom
Band gap	-0.04 eV
Specific heat capacity (at room temperature)	0.690-0.719 kJ/kg.K
Magnetic susceptibility	0.141×10^{-6} cm^3/g

Graphite also has properties such as low density (depending on type, i.e. hexagonal and rhombohedral), low friction coefficient (for the hexagonal graphite), chemical stability (at ordinary temperature), high electrical and thermal reactivity and low thermal expansion coefficient [Pie93].

2.2.1.2 APPLICATION OF GRAPHITE

Since graphite has various allotrope properties, this makes it so applicable. Some applications of graphite are listed below [Pie93], [Ter10].

- ✓ Due to low capacitance of nano-ribbon graphite, it has been applied in the fabrication of chemical sensors, biosensors.
- ✓ From a material science point of view, they can be used in the fabrication of robust polymer composites as fillers.
- ✓ Because (the hexagonal) graphite is a good conductor, it has been applied to fabricate highly conducting transparent films and thermal conducting polymers.
- ✓ Graphite is able to embed electromechanically negative and positive ions. Therefore, it can be used in electromechanical applications such as battery electrodes for Li-ion batteries.
- ✓ In terms of chemical applications of graphite nano-ribbons, some of the applications are novel catalytic reactions, the assembly of heavy metal filters, drug delivery, etc.

2.2.2 DIAMOND

Diamond is one of the hardest solid materials known to scientists. It can be found in two structures, cubic and hexagonal (londsdaleite). The latter is rare in nature. The formation of cubic diamond is by arrangement of ABCABC stacking, while in hexagonal type it forms ABAB stacking. Figure 2.11 illustrates both diamond structures. Both forms can be interconverted only in special circumstances. These two forms of diamond are three dimensional and surrounded by four neighbors of other carbon atoms. Each carbon atom has the sp^3-hybridization. It strongly bonds to the neighbors and makes a tetrahedral network (see Figure 2.12) [Kru10], [Fal07].

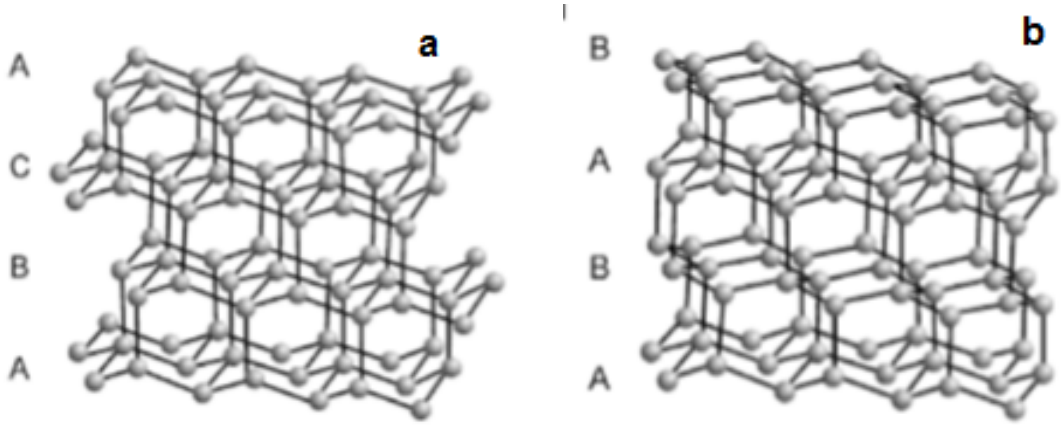

Fig. 2.11. The two types of diamond structures (a) hexagonal and (b) cubic. Taken from [Kru10]

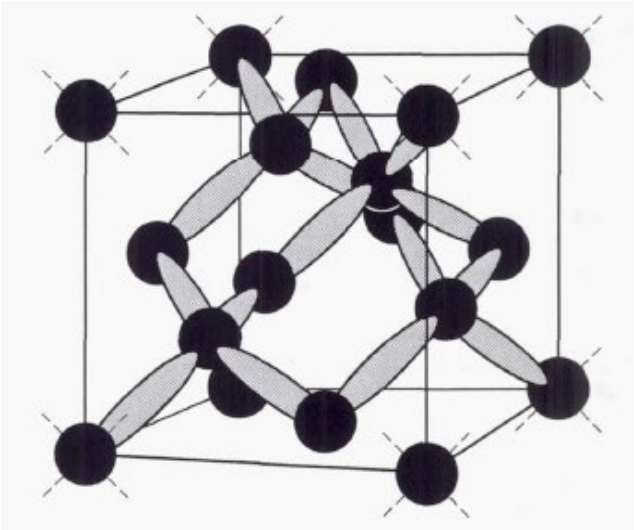

Fig. 2.12. The diamond lattice structure having sp^3 covalent bonding. Taken from [Miy98]

Diamond can transform thermodynamically into graphite under specific conditions. It will happen in vacuum or in an inert atmosphere, at low pressure and at temperatures above 1500 ^oC. In contrast, in some opposite conditions the formation of hexagonal and cubic diamond would be possible. It can be formed by compression of graphite at high pressure (> 15 GPa) and at high temperatures (500 ^oC-1700 ^oC) in vacuum [Fal07], [Pie93], [Niu12].

2.2.2.1 PROPERTIES OF DIAMOND

Diamond is a stable material in both structures, cubic and hexagonal (lonsdaleite). Because of the four neighbors and sp^3-hybridization, diamond has high values for hardness and thermal conductivity. It is well known as a good electrical insulator and as a wide bandgap semiconductor by doping some other elements such as nitrogen, boron, etc. [Kru10]. It is also has a high neutron radiation resistance. A main industrial application is based on its high refraction index [Pie93]. Some physical properties of diamond are stated below: [Kru10], [Miy98], [Ume10], [Zhu11]

Table 2.3. Physical properties of diamond

Crystal forms	cubic and hexagonal
Density	3.52 g/cm^3 (theoretical the same for both structures) [Bun67]
Lattice constants In face-central cubic (fcc) structure In hexagonal structure	 356.68 pm a_0 = 252 pm and c_0 = 412 pm
Band gap	~ 5.5 eV
Bond length (C-C)	154.45 pm
Interplanar distance of hexagonal structure	205 pm
Coefficient of thermal expansion (at room temperature)	1.06×10^{-6} $^oC^{-1}$
Thermal conductivity (at room temperature)	2000 W/m.K
Compressing strength	8.68-16.53 GPa
Hardness	10 Mohs or 5700-10400 kg/mm^2
Resistivity	$> 10^{18}$ Ω.m
Coefficient of friction In air In vacuum	 0.05-0.1 ~ 1

2.2.2.2 APPLICATION OF DIAMOND

Because of the remarkable properties of diamond it has many technological applications. Some of these applications are mentioned below.

- ✓ High thermal conductivity and a high carrier mobility. The former allows it to be used in electronic devices as heat sinks for semiconductor lasers. Both these properties are important when diamond is used in high power transistors [Bar14], [Har04].
- ✓ Because of its hardness and good stability from a thermodynamic point of view, diamond is a suitable material for abrasive devices and tribological applications [Fal07], [Miy98].
- ✓ Because of its high chemical and thermal inertness, and its transparency, diamond is useful for applications such as protective coatings for electronic, mechanical, optical and biomedical components [Lin11].
- ✓ Many applications of diamond are due to its hardness, toughness and chemical stability. Therefore, it is a perfect material in cutting and grinding tools, oil drilling bites and cutting ceramics and its composites [Pie93].

2.2.3 FULLERENE

Smalley and Kroto [Sma85] discovered the fullerene in 1985 by observing carbon atom clusters in molecular range of C_{30}-C_{100}. Theoretically, many structures of fullerene with hundred atoms are possible. However, five fullerene structures i.e. C_{60}, C_{70}, C_{76}, C_{78}, and C_{84} have been identified so far (see Figure 2.13). The C_{60} molecule consists of sixty carbon atoms. They form twenty hexagons plus twelve pentagons, shaped like soccer ball. C_{70} is like a rugby ball and has a red-orange colour in solution. C_{76} possesses an arrangement of pentagon and hexagon C atoms. It has a green-yellow colour in solution. The C_{78} is golden-yellow and chestnut brown and the C_{84} is olive-green in solutions. Unlike diamond and graphite (with cubic, hexagonal and rhombohedral crystalline structures), fullerene is not only one type of material. Its structure generally, is a cage-like spheroid form consisting of pentagon and hexagon networks. The sigma (σ) orbitals in fullerene no longer cover all of the s-orbital and the pi (π) orbitals and do not belong totally to purely p-orbital, as in graphite. Fullerene hybridization is not stable and not like the sp^3 or sp^2 hybridizations, in diamond and graphite. The hybridization in fullerene only depends on the carbon atom numbers in the

molecule. Fullerene is the first known carbon phase which can transform into diamond at room temperature. This will happen by fast compression of C_{60} powder in less than a second and at more than 150 atm [Pie93].

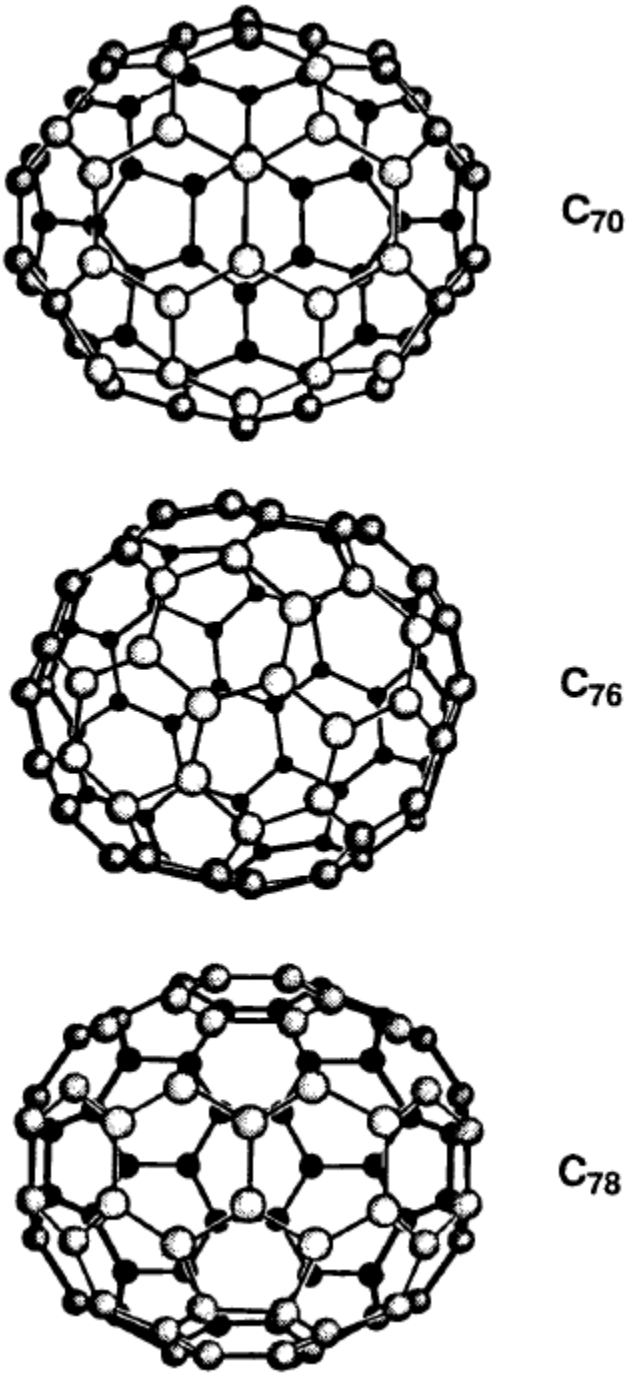

Fig. 2.13. Schematic illustrations of some fullerene molecules. Taken from [Pie93]

Fullerene can appear in other definitions such as single-walled nanotubes of carbon. In other word, when the dangling bonds of carbon atoms at the end (edge) of a finite layer of graphene connect together, the single-walled carbon nanotube or fullerene is formed. Both fullerene and nanotubes of carbon combine six carbon rings, which via its pentagonal structure, are connected together. The other appearance is carbon onions (rings) which are considered as fullerene. Among these cases, C_{60} is the most stable, dominant, famous, aromatic, and the most symmetric one of the fullerene molecules. Figure 2.14 shows a typical fullerene (C_{60}) molecule [Fal07], [Ter00], [Sat06].

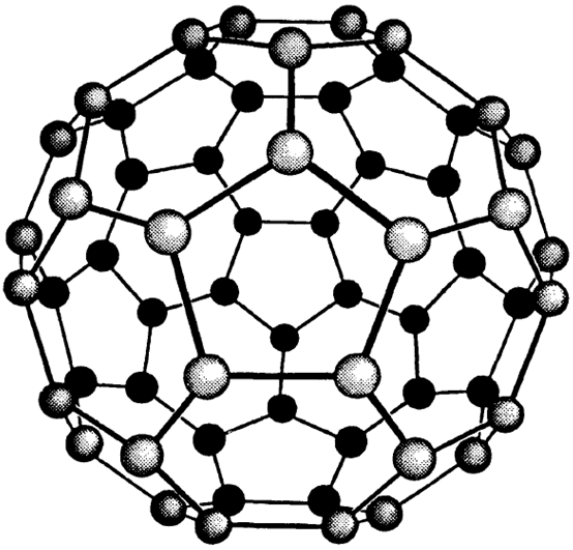

Fig. 2.14. A picture of C_{60} fullerene molecule. Taken from [Pie93]

2.2.3.1 PROPERTIES AND APPLICATION OF FULLERENE

C_{60} aggregates are considered to be the softest solid state of carbon. However, it could be harder than diamond if it is exposed to high pressure and compressed to 70% of its initial volume. From a physical point of view C_{60} aggregates are stable while chemically it is reactive by free radicals [Pie93]. On the basis of the interesting physical properties of C_{60}, biological and solar cells applications have been studied recently [Fal07]. Due to the solubility of fullerene in water, it has been found that it has pharmacological effects on body cells, organs, nucleic acid and enzymes. Also because of the pharmacological properties it has been applied in biomedicine since it has been discovered in 1985 [Sat06].

2.2.4 GLASSY CARBON

Glassy (vitreous) carbon was first introduced in early 1960s [Har04]. It is produced after a high temperature carbonization of a polymeric precursor. Glassy carbon is classified as a non-graphitizing carbon which has ribbon-like and tangled graphitic microstructure/crystallites [Jen71]. It is regarded as an amorphous carbon with a structure that includes sp^2 (trigonal) and sp^3 (tetragonal) bonds [Pie93]. Noda and Inagaki [Nod64] and Furukawa [Fur64] assumed that glassy carbon is composed of tetrahedral and graphite parts (Figure 2.15) [Kag65].

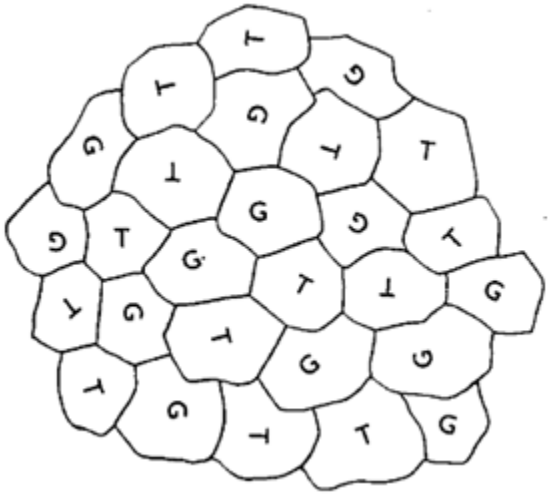

Fig. 2.15. The Noda, Inagaki and Furukawa model for the microstructure of glassy carbon. Taken from [Nod64], [Fur64]

A different model for glassy carbon, as illustrated in Figure 2.16 was proposed by Jenkins and Kawamura [Jen71]. They manufactured glassy carbon by slow, controlled transformation of certain polymers at the temperature range of 900-1000 ^{o}C. This model consisted of very narrow microfibers and twisted ribbon-like graphite. This model was widely accepted but it was imperfect. For instance, since glassy carbon is highly impermeable to gases, this model with its micropore structure is expected to be permeable [Har05], [Har04].

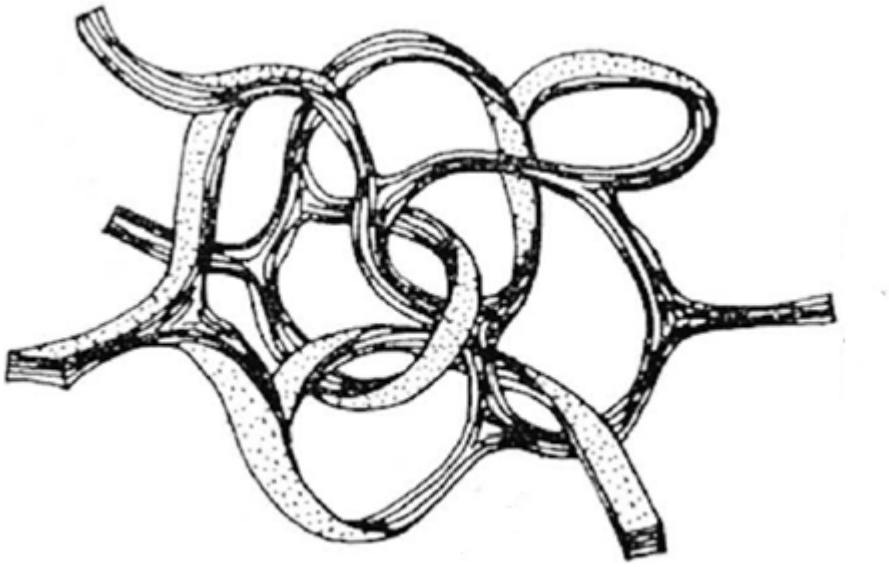

Fig. 2.16. The Jenkins and Kawamura model of glassy carbon. Taken from [Jen 71]

Sigradur is a glass-like carbon form which is often used for chemical and physical experiments. It has high quality texture, it is non-wettable, with very low levels of impurities [www18]. Other properties are summarized in Table 4. Two types of Sigradur glassy carbon have been manufactured. The difference between these two types is related to the temperatures at which they are manufactured. The first one is the glassy carbon, Sigradur K, which is manufactured at relatively low temperatures such as 1000 ºC. It consists of disordered microstructures. These microstructures include tightly curled carbon layers with nanopores of 1 nm in diameter (Figure 2.17 (a)). The second model pertains to Sigradur G, a glassy carbon which is produced at high temperatures such as 3000 ºC. It has the large pores of about 5 nm in diameter (Figure 2.17 (b)). Both types of Sigradur glassy carbons are bounded by curved graphitic walls and facets. Like other non-graphitizing carbons, glassy carbon also has fullerene-related structures [Har04].

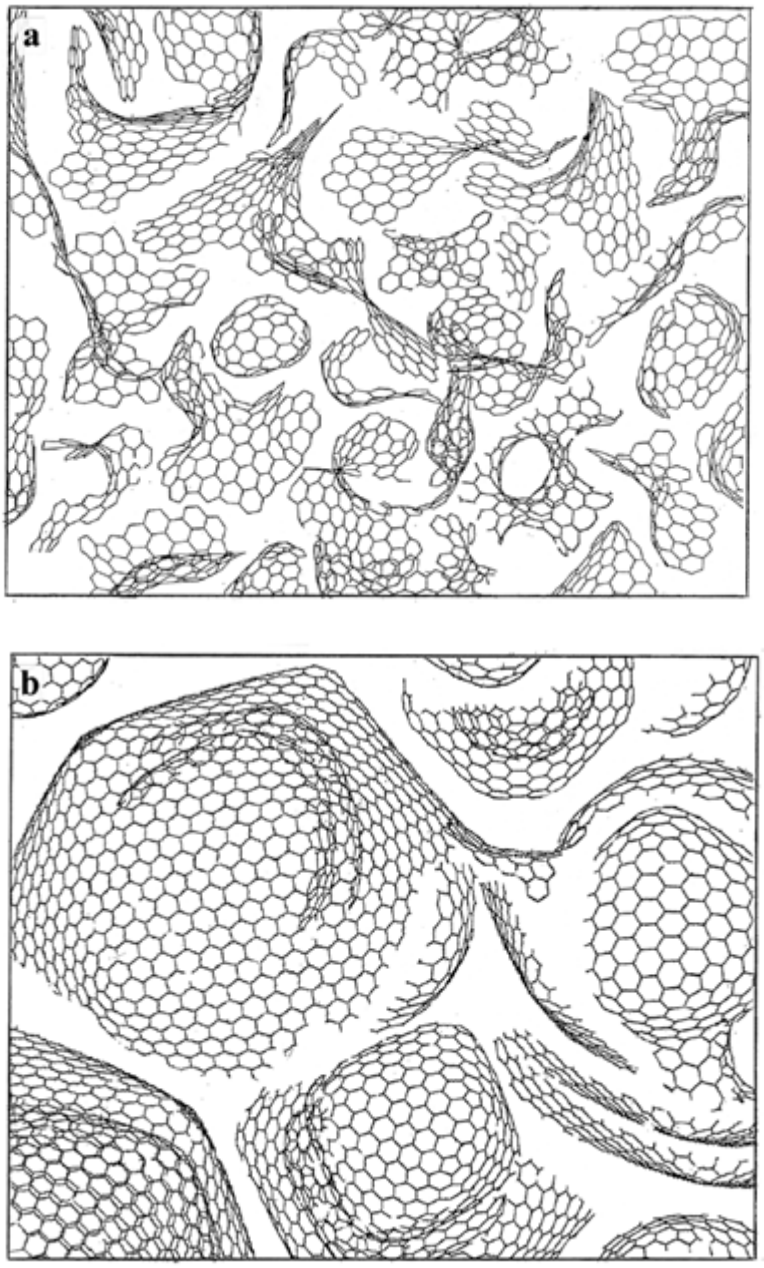

Fig. 2.17. Models for the structure of (a) Sigradur K and (b) Sigradur G. Taken from [Har04]

In terms of hardness and density Sigradur K glassy carbon has more applications than Sigradur G glassy carbon. However, in our study Sigradur G glassy carbon is used due to its higher thermal resistance (~ 3000 ^{o}C), higher corrosion and erosion resistance and high thermal conductivity compared to Sigradur K glassy carbon.

2.2.4.1 PROPERTIES OF SIGRADUR GLASSY CARBON

Due to the properties of glassy carbon, it is widely used in many technological applications. Some of the physical properties are summarized in Table 4: [Pie93], [Yam68]

Table 2.4. Physical properties of glassy carbon

Property	Sigradur K	Sigradur G
Density	1.54 g/cm^3	1.42 g/cm^3
Compressive strength	580 MPa	480 MPa
Tensile strength	190 MPa	130 MPa
Hardness	120 Moh	70 Moh
Flexural strength	210 MPa	260 MPa
Heat proof limit	Up to 1000 ^oC	Up to 3000 ^oC
Gas permeability	10^{-12} cm^2/s	10^{-7} cm^2/s
Thermal expansion coefficient (20-200 ^oC)	3.5 x 10^{-6} K^{-1}	2.6 K^{-1}
Thermal conductivity	4.6 W/m.K	6.3 W/m.K
Electrical resistivity	50 x 10^{-4} Ω.cm	35 x 10^{-4} Ω.cm
Spalling coefficient	21000 kcal/m.hr	17000 kcal/m.hr
Energy gap	10^{-2} eV	10^{-3} eV
Specific heat	5 kcal/kg.K	50 kcal/kg.K
Young's modulus of elasticity	35 GPa	35 GPa

Other properties of glassy carbon that should also be mentioned are a smooth surface and a relatively low electrical resistivity. Hence, glassy carbon has been proposed to be applied as microphone electrodes, lightning protectors for telephone circuits, and electrodes to produce metal films [Yam68].

Glassy carbon might also have nuclear reactor applications. This is because of its low impurity content. Our research group at the University of Pretoria has proposed glassy carbon as a container material to isolate nuclear waste. It has been considered as a suitable material for fabricating a nuclear storage cask because of the some remarkable properties such as high thermal resistance, chemical attack resistance, extreme corrosion and erosion resistance, strength and hardness [Pie93], [Har04].

The other advantages of using the glassy carbon as a diffusion barrier in nuclear reactors are summarized below.

- ✓ The impermeability to gases and liquids [Lin11]
- ✓ The high resistance to thermal shock and high stability against aggressive alkaline earth halides such as CaF_2 [Yam68]
- ✓ Low level of impurities, etc.

It was reported that ion implantation to different concentrations can improve some properties of glassy carbon such as wear resistance and mechanical properties [Iwa89], [McC94]. It has been suggested that due to the increase in the density of glassy carbon after implantation, it would be a good abrasive wear resistant. Ion implantation will discuss detailed in next chapter.

Our group at University of Pretoria, South Africa has published many papers about the application of glassy carbon as a diffusion barrier in nuclear reactor plants. Some of these include;

- ❖ Ion bombardment of glassy carbon [Mal18]
- ❖ Heat treatment behavior of xenon implanted into glassy carbon [Ism18]
- ❖ Surface changes after strontium ion implantation into glassy carbon [Odu18]
- ❖ Interface interaction of tungsten deposited on glassy carbon [Inn18]
- ❖ Annealing effects on the migration of cadmium ion implantation into glassy carbon [Hla17]
- ❖ Structural modification of indium implanted into glassy carbon [Njo17]

2.2.4.2 APPLICATIONS

Although the properties of glassy carbon depend on the processing conditions, generally it has many significant properties which makes it remarkable and very useful. Some applications due to these outstanding properties are stated as following:

- Chemically inertness (oxidation resistant): the oxidation rate of glassy carbon (in dry air) and its reaction with water vapor and carbon dioxide is less than other carbon allotropes. So it is useful to apply in navy missiles and supersonic combustion engines [Har04], [New93].
- Good electrical conductivity: the chemically inertness of glassy carbon accompanied with its good electrical conductivity makes it a suitable material for acid-battery electrodes [Pie93].
- High resistant to chemical attack: glassy carbon shows a significant resistance to attack by acids. For instance, glassy carbon will be unaffected in exposure of sulfuric and nitric acids at room temperature for several months. It is also not attacked by chromic and hydrofluoric acids. Due to its outstanding features, glassy carbon is being applied in electrochemistry as crucibles and electrodes [Pie93], [Har04].
- Extreme corrosion resistance: investigations on the compatibility of glassy carbon with other materials such as chloride fused salts and alkali metals such as Li, Na, K, etc. showed that it is an appropriate material in nuclear reactor application [Yam68]. In addition, glassy carbon is a biocompatible material which makes it fine for prosthetic devices [Har04].
- High temperature resistance: since glassy carbon's melting point is estimated to be around 4000 ^{o}K [Tok64], it is applied in electronic devices such as minute heaters [Yam68].
- High erosion resistance: this property makes glassy carbon useful in the mechanical field. It is applied as mandrels, rollers, equipment for glass working, etc. [Yam68].

REFERENCES

[Bar14] J. Barjon, F. Jomard, S. Morata, "Arsenic-bound excitations in diamond", Physical Review B: Condensed Matter and Materials Physics, 89(4), pp. 1–5, 2014.

[Bun67] F. Bundy, J. Kasper, "Hexagonal Diamond: A New Form of Carbon", Journal of Chemical Physics, 46(9), pp. 3437, 1967.

[Fal07] E. H. Falcao, F. Wudl, "Carbon allotropes: beyond graphite and diamond", Chemical Technology and Biotechnology, pp. 524–531, 2007.

[Fra51] R. E. Franklin, "Crystallite growth in graphitizing and non-graphitizing carbons", Proceedings of the Royal Society A: Mathematical, Physical and Engineering Sciences, 209(1097), pp. 196–218, 1951.

[Fur64] K. Furukawa, "Nippon Kessho Gakkaishi (in Japanese)", 1964.

[Har04] P. J. F. Harris, "Fullerene related structure of commercial glassy carbons", Philosophical magazine, 84(29), pp. 3159–3167, 2004.

[Har05] P. J. F. Harris, "New perspectives on the structure of graphitic carbons", Critical reviews in solid state and materials sciences, 30(4), pp. 235–253, 2005.

[He12] C. He, L. Sun, C. Zhang, X. Peng, K. Zhang, J. Zhong, "Four superhard carbon allotropes: A first-principles study", Physical Chemistry Chemical Physics, 14(23), pp. 8410–8414, 2012.

[Hla17] T. T. Hlatshwayo, L. D. Sebitla, E. G. Njoroge, M. Mlambo, J .B. Malherbe, "Annealing effects on the migration of ion-implanted cadmium in glassy carbon", Nuclear Instruments and Methods in Physics Research, Section B: Beam Interactions with Materials and Atoms, 395, pp. 34–38, 2017.

[Inn18] A. J. Innocent, T. T. Hlatshwayo, E. G. Njoroge, J. B. Malherbe, "Interface interaction of tungsten film deposited on glassy carbon under vacuum annealing", Vacuum, 148, pp. 113–116, 2018.

[Ism18] M. Y. A. Ismail, J. B.Malherbe, O. S. Odutemowo, E. G. Njoroge, T. T. Hlatshwayo, M. Mlambo, E. Wendler, "Investigating the effect of heat treatment on the diffusion behaviour of xenon implanted in glassy carbon", Vacuum, 149, pp. 74–78, 2018.

[Iwa89] M. Iwaki, K. Takahashi, K. Yoshida, Y. Okabe, "Improvement of wear properties of glassy carbon surface layer modified by ion implantations", Nuclear Inst. and Methods in Physics Research, B, 39(1–4), pp. 700–703, 1989.

[Jen71] G. Jenkins, K. Kawamura, "Polymeric carbons-carbon fiber, glass and char", Cambridge university press, 1971.

[Kag65] J. Kaginoki, "A model for the structure of glassy carbon", Acta crystal, 18(2–3), pp. 578–579, 1965.

[Kin11] K, Kingsley, C. Ho, H. Qian, A. Bismarck, "Carbon Fiber: Surface Properties", Wiley Encyclopedia of Composites, pp. 1–11, 2011.

[Kru10] A. Krueger, "Carbon Materials and Nanotechnology", Wiley-VCH Verlag GmbH, 2010.

[Li07] Z. Q. Li, C. J. Lu, Z. P. Xia, Y. Zhou, Z. Luo, "X-ray diffraction patterns of graphite and turbostratic carbon", Carbon, 45(8), pp. 1686–1695, 2007.

[Lin11] Y. Lin, L. Zhang, H. K. Mao, P. Chow, Y. Xiao, M. Baldini, J. Shu, W. L. Mao, "Amorphous diamond: A high-Pressure superhard carbon allotrope", Physical Review Letters, 107(17), pp. 30–33, 2011.

[Mal18] J. B. Malherbe, O. S. Odutemowo, E.G. Njoroge, D.F. Langa, T.T. Hlatshwayo, C.C. Theron "Ion bombardment of glassy carbon", Vacuum, 149, pp. 19–22, 2018.

[McC94] D. McCulloch, S. Prawer, A. Hoffman, "Structural investigation of xenon-ion-beam-irradiated glassy carbon", Physical review B, 50, pp. 5905, 1994.

[Miy98] K. Miyoshi, "Structures and mechanical properties of natural and synthetic diamonds", pp. 26, 1998.

[New93] R. W. Newman, "Oxidation-resistant high-temperature materials", Johns Hopkins APL Technical Digest (Applied Physics Laboratory), 14(1), pp. 24–28, 1993.

[Niu12] H. Niu, X. Q. Chen, S. Wang, D. Li, W. L. Mao, Y. Li, "Families of superhard crystalline carbon allotropes constructed via cold compression of graphite and nanotubes", Physical Review Letters, 108(13), pp. 31–35, 2012.

[Njo17] E. G. Njoroge, L. D. Sebitla, C. C. Theron, M. Mlambo, T. T. Hlatshwayo, O. S.

Odutemowo, V. A. Skuratov, E. Wendler, J. B. Malherbe, "Structural modification of indium implanted glassy carbon by thermal annealing and SHI irradiation", Vacuum, 144, pp. 63–71, 2017.

[Nod64] T. Noda, M. Inagaki, "The structure of glassy carbon", Materials Research Bulletin, 37, pp. 1534–1538, 1964.

[Odu18] O. S. Odutemowo, J. B. Malherbe, L. C. Prinsloo, E. G. Njoroge, R. Erasmus, E. Wendler, A. Undisz, M. Rettenmayr, "Structural and surface changes in glassy carbon due to strontium implantation and heat treatment", Journal of Nuclear Materials, 498, pp. 103–116, 2018.

[Pau66] L. Pauling, "The structure and properties of graphite and boron nitride", Proceedings of the National Academy of Sciences, 56(6), pp. 1646–1652, 1966.

[Pes11] G. Peschel, "Carbon - Carbon bonds: Hybridization", 2, pp. 1–6, 2011.

[Pie93] H. O. Pierson, "Handbook of carbon, graphite, diamond and fullerenes: Properties, processing and applications", Noyes, 1993.

[Sat06] M. Satoh, I. Takayanagi, "Review pharmacological studies on fullerene (C60), a novel carbon allotrope, and its derivatives", 518, pp. 513–518, 2006.

[She11] X. L. Sheng, Q. B.Yan, F. Ye, Q. R. Zheng, G. Su, "T-carbon: A novel carbon allotrope", Physical Review Letters, 106(15), pp. 2–5, 2011.

[Sma85] H. W. Kroto, J. R. Heath, S. C. O'Brien, R. F. Curl & R. E. Smalley, "C60: Buckminsterfullerene", 318, pp.162-163, 1985.

[Ter00] H. Terrones, M. Terrones, E. Hernández, N. Grobert, J. C. Charlier, P. M. Ajayan, "New metallic allotropes of planar and tubular carbon", Physical Review Letters, 84(8), pp. 1716–1719, 2000.

[Ter10] M. Terrones, A. R. Botello-Méndez, J. Campos-Delgado, F. López-Urías, Y. I. Vega-Cantú, F. J. Rodríguez-Macías, A. L. Elías, E. Muñoz-Sandoval, A. G. Cano-Márquez, J. C. Charlier, H. Terrones, "Graphene and graphite nanoribbons: Morphology, properties, synthesis, defects and applications", Nano Today, 5(4), pp. 351–372, 2010.

[Tok64] B. Tokiti, "The melting of glassy carbon", (002), pp. 1709–1710, 1964.

[Ume10] K. Umemoto, R. M. Wentzcovitch, S. Saito, T. Miyake, "Body-centered tetragonal C_4: A viable sp^3 carbon allotrope", Physical Review Letters, 2010.

[Www17] www.google.com, "s-orbital and p-orbital hybridizations", 2017.

[Www18] www.google.com, "Sigradure comercial glassy carbon", 2018.

[Yam68] S. Yamada, "A Review of Glasslike Carbons", 1968.

[Zhu11] Q. Zhu, A. R. Oganov, M. A. Salvadó, P. Pertierra, A. O. Lyakhov, "Denser than diamond: Ab initio search for superdense carbon allotropes", Physical Review B: Condensed Matter and Materials Physics, 83(19), pp. 1–4, 2011.

CHAPTER 3

ION IMPLANTATION

When a sample is bombarded by an energetic ions beam, it loses some of its ions due to sputtering but some of the incident ions will be retained in the sample. The retained ions of incident beam is also said to have been implanted and the technique is called ion implantation [Gib68]. Due to the elastic and inelastic interactions between the incident ion and the substrate, the ion loses its energy till it comes to rest in the substrate. The interactions will be collisions between the incident ion and electrons or nuclei of the substrate atoms resulting in the disruption of the lattice structure [Hic07].

Ion implantation is versatile technique which is applied to form new meta-stable materials in solid surface layers. Solid carbons such as diamond, graphite, amorphous carbon are favorable materials in engineering and surface material science. Ion implantation will be a good technique to improve the properties of these materials for more applications [Iwa89]. Ion implantation in semiconductors provides a doping technique with some advantages over more conventional doping methods. Some of the advantages are; i) the ability to induce the controlled amount of almost any desired impurity element into a substrate, ii) the ability to control the profile of doping by adjusting the energy, current and ion beam position in three dimensions and, iii) the possibility of avoiding detrimental effects which may accompany the high temperature diffusion process [Gib68].

Ion implantation is also used to experimentally, simulate radiation damage processes in materials for applications in nuclear reactors [Was07]. The simulation via ion implantation technique will take only hours or several minutes while neutron irradiation in a reactor usually takes several days. In addition, such irradiation in a reactor usually leads to radioactivity in the material which either entails very long cooling periods or specialized equipment to analyse the irradiated material. Generally, all implanters have an ion beam source, acceleration and target chamber. Ions are ionized, then electrostatically accelerated to a high energy and finally enter into the target chamber and implanted into the substrate surface. Figure 3.1 shows a schematic diagram of a typical ion implanter [Nas06].

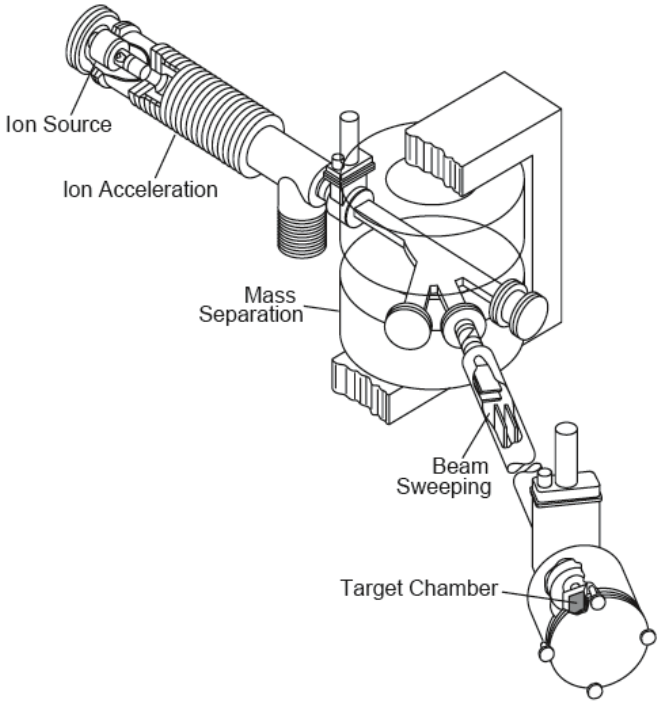

Fig. 3.1. General schematic diagram of an ion implanter. Taken from [Nas06]

3.1 ENERGY LOSS AND STOPPING CROSS-SECTION

When an incident energetic particle penetrates into a target, it will lose energy due to many collisions along its path. As the particle goes through the target, it slows down until it comes to rest. The amount of energy (ΔE) lost in a distance traveled (Δx) depends on the composition and deposition of target, projectile species and its velocity. The stopping force (often also termed stopping power) in a material is defined as [Chu78]:

$$\lim_{\Delta x \to 0} {}^{\Delta E}/_{\Delta x} \equiv \frac{dE}{dx}(x) \tag{3.1}$$

where E is the incident ion energy per penetration depth x. The energy range used frequently for backscattering spectroscopy of $^4He^+$ is between 0.5 and 3 MeV. The usual value of dE/dx for this range of energy is between 10-100 eV/Å. Assuming that the dE/dx is known at any energy, the particle energy i.e. E, at any depth of x below the surface is given by [Chu78]:

$$E = E_0 - \int_0^x \left(\frac{dE}{dx}\right) dx \tag{3.2}$$

where E_0, is the initial (i.e. incident) energy. Generally dE/dx, is given as a function of energy, E, not x. Equation (3.2) is not easy to calculate without knowledge of the energy as a function of *x*, E(x). This difficulty can be solved by regarding of *x* as a function of E (rather than E as a function of *x*). Then we have:

$$x = \int_E^{E0} \left(\frac{dx}{dE}\right) dE = \int_E^{E0} \left(\frac{dE}{dx}\right)^{-1} dE \qquad (3.3)$$

In a thin layer with thickness Δx, the number of exposed atoms to the beam is equal to SN Δx where N is the target atomic density and S is the area irradiated by the beam. A surface density produced by these atoms on the area S is SN Δx/S = NΔx. This quantity increases linearly with Δx as the energy loss, ΔE = (dE/dx) Δx, does. Setting therefore, the ΔE proportional to NΔx, stopping cross-section per atom is defined as the proportionality factor and is given by [Chu78]:

$$\varepsilon = -1/N\ (dE/dx) \qquad (eV.cm^2) \qquad (3.4)$$

The unit given in equation (3.4) is the typical one used in RBS analysis. Another related (but different) definition, which is prominently used in nuclear physics as stopping cross section is:

$$\varepsilon^* = -1/\rho\ (dE/dx) \qquad (keV.cm^2/atom) \qquad (3.5)$$

where ρ is target mass density with the unit of g/cm^3. The two equations above, i.e. (3.4) and (3.5) can be converted to each other by:

$$\rho = N\ (M/N_0) \qquad \rightarrow \qquad \varepsilon^* = \varepsilon\ (N_0/M) \qquad (3.6)$$

where M is the target atomic weight (g/mole) and N_0 is the Avogadro's number; 6.025×10^{23} (atom/mole).

3.2 ION STOPPING

Ion stopping in a substrate is defined as the average energy loss per unit path length at a particular depth of the particle due to its interactions with substrate atoms. The stopping force is given by [Bac12]:

$$S = -\ dE/dx \qquad (3.7)$$

where E is the kinetic energy of incident particle and x is the distance along the particle path in the substrate. The negative sign represents the decrease of energy after collisions along the ion trajectory. In the older literature the term used for equation (3.7) was stopping power. Even in some modern papers this incorrect term is still used.

An incident particle in a target can lose its energy by two ways; first by interaction with electrons of target atoms (electronic energy loss) and second by interaction to the nuclei of target atoms (nuclear energy loss). Therefore the stopping force will be the sum of both energy loss mechanisms and is given by [Bac12]:

$$S = S_n + S_e = - [(dE/dx)|_n + (dE/dx)|_e] \quad (3.8)$$

3.2.1 NUCLEAR STOPPING

From the nuclear collision mechanism, energy is transmitted from the incoming particle to a target nucleus. In this event energy is lost by interactions between a moving incident ion and a target atom nuclei. To calculate the nuclear stopping ion penetration in a material, the interatomic potential for the particular ion and substrate material is used [Zie88]. In nuclear stopping the average energy loss that comes from elastic collisions between target atoms nuclei and incident ion beam is considered. The nuclear stopping is the energy lost by a moving particle (due to elastic collisions) per length traveled in the target at a particular depth and it is given by [Nas06]:

$$S_n = \frac{dE}{dx}\Big|_n \quad (3.9)$$

For simplicity in the calculation of the nuclear stopping as an elastic collision, it is assumed that the interaction will be isolated, i.e. the interactions from other target atom nuclei or ions are ignored. The energy T transferred from the incident ion to the target atom is given by [Was07]:

$$T = \left[\frac{4E_0\, M_i\, M_t}{(M_i+M_t)^2}\right] \sin^2\left(\frac{\theta}{2}\right) \quad (3.10)$$

where M_i is the incident ion mass, the M_t is the target mass, E_0 is the kinetic energy of incident ion and θ is scattering angle. This equation contains the energy lost by the projectile and will lead to the stopping force of the incident particle when the energy loss cross section is evaluated. The nuclear stopping force is estimated as follows [Zie88]:

$$S_n(E) = \int_0^{\infty} T(E,b)2\pi db = 2\pi \frac{4M_1M_2}{(M_1+M_2)^2} E_0 \int_0^{b_{max}} \sin(\frac{\theta}{2})^2 \, b \, db \quad (3.11)$$

where *b* is the impact parameter, see Figure 3.2. The biggest problem in calculating the stopping force is to find the interatomic potential of repulsive interactions. The interatomic potential for binary (Fig. 3.2) and isolated (elastic collision) interactions of two positive particles, is given by:

$$V(r) = \frac{Z_1 Z_2 e^2}{4\pi\epsilon_0 r} \quad (3.12)$$

where Z_1 and Z_2 are the atomic numbers of incident ion and target atom respectively, e is the electronic charge, ε_0 is the permittivity of free space and *r* is the interatomic distance.

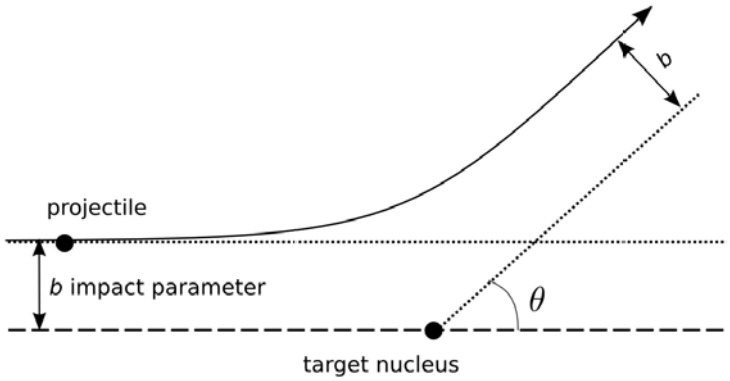

Fig. 3.2. A typical two-body scattering process with an impact parameter b. Taken from [Bac12]

For small atomic distances r, i.e. $0 < r \ll a_0$, where a_0 is Bohr's atomic radius in hydrogen (= 0.53 Å), the equation (3.12) is valid. The reason is that for small separations there are not any electrons between the two colliding nuclei, and the potential is totally repulsive and can be described by a Coulomb potential. In the cases when the distance between two atoms is longer, i.e. of the order of a_0 or larger, the Coulomb potential is no longer valid. It is due to the screening effect of the shell electrons in the region between two atoms nuclei [Wer06]. Therefore a screening function ($\Phi(r/a)$) is needed to estimate the interaction potential correctly. Then the new form of the repulsive potential is given by [Bac12]:

$$V(r) = \frac{Z_1 Z_2 e^2}{4\pi\epsilon_0 r} \Phi(r/a) \quad (3.13)$$

where *a* is the screening length which is in order of Bohr's atomic radius.

Firsov [Fir58] estimated the a value from some analytical results, which is given by:

$$a = \frac{a_0}{\sqrt[3]{(Z^{1/3} + Z^{1/3})^2}} \tag{3.14}$$

A so-called universal potential was developed by Ziegler et al., considering the *a* as below [Zie85]:

$$a = \frac{0.8854\, a_0}{(Z_1^{0.23} + Z_2^{0.23})} \tag{3.15}$$

Then the screening function obtained by [Zie88]:

$$\Phi(r/a) = 0.1818\, e^{-3.2\, r/a} + 0.5099\, e^{-0.9432\, r/a} + 0.2802\, e^{-0.4028\, r/a} + 0.02817\, e^{-0.2016\, r/a} \tag{3.16}$$

The nuclear stopping cross section for energy E is given by [Nas06]:

$$\varepsilon_n = -\frac{1}{N}\left(\frac{dE}{dx}\right)\Big|_n = \int_{T_{min}}^{T_{Max}} \frac{d\sigma(E)}{dT}\, dT \tag{3.17}$$

where $\frac{d\sigma(E)}{dT}$ is the energy transferred differential cross section. A highly accurate nuclear stopping cross section was calculated by Ziegler, Biersack and Littmark (ZBL), and given by [Zie85]:

$$\varepsilon_n = \frac{0.5\ln(1+1.13839\eta)}{(\eta + 0.01321\eta^{0.21226} + 0.19593\eta^{0.5})} \tag{3.18}$$

where η is the reduced energy is given by:

$$\eta = \frac{32.53 M_2 E_0}{Z_1 Z_2 (M_1 + M_2)(Z_1^{0.23} + Z_2^{0.23})} \tag{3.19}$$

3.2.2 ELECTRONIC STOPPING

Electronic stopping occurs when energy is transferred from an energetic ion to the target electrons. The interaction between the electrons in target atoms and charged particle is complicated. This makes this mechanism difficult to describe. The collision of the incident particles to the electrons of target atoms, leads to ionization or excitation of these electrons [Zie85], [Len 84].

Figure 3.3 shows a typical ratio between nuclear and electronic stopping force. It also shows the three energy regions for electronic stopping.

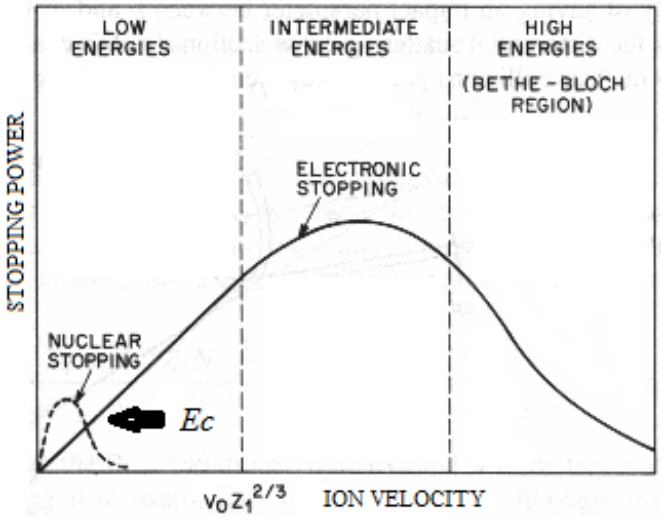

Fig. 3.3. Nuclear and electronic stopping force plot. Taken from [www18]

It can be seen that, at low energies, nuclear stopping dominates while at high energies electronic stopping dominates. Electronic stopping dominates above the critical energy, E_c, then reaches a maximum and decreases at the very high energy region (Bethe-Bloch region) [Chu78].

The first region in Figure 3.3 is the area (labeled as low energies), where the incident ion velocity $v_i \ll v_0 Z_1^{2/3}$ where Z_1 is atomic number of incident ion [Zie85]. For europium the term of $v_0 Z_1^{2/3}$ is about 3.5 x 10^7 m/s. In this study with 250 keV europium implanted, the initial ion velocity is about 5.6 x 10^5 m/s. It is clear that for this velocity and energy this is far from the Fermi velocity (v_F), which is between the 0.7 and 1.3 v_0, i.e. 1.54 – 2.86 x 10^6 m/s. It means for implanted europium in this study, as shown in Fig. 3.4, the implantation process involves in the first region, i.e. low energies and low velocity. Thus the nuclear stopping dominates in this study. One of the first successful theories of electronic stopping was by Fermi and Teller [Fer47]. Later it was established that this theory was only valid in in first region in Figure 3.3. They found that for heavy ions at low velocities the typical energy loss of per unit distance for particles is proportional to ion velocity; $dE/dx \sim v\rho_e^{1/3}$, where v is particle velocity and ρ_e is electron density. At low velocities (first region in Figure 3.3), Lindhard [Lin54] also found that the electronic stopping of a charged particle in the local density approximation to be given by:

$$S_e = \int L(v, \rho_e)\, Z_1^2\, \rho_e\, dV \qquad (3.20)$$

where S_e is the electronic stopping, L is the stopping interaction function of a particle of unit charge with velocity of v, Z_1 is the atomic number of the incident particle, ρ_e, is the electronic density of the target and V is the target volume. To achieve a solution for finding the electronic stopping and the related scattering cross-section, it has been suggested to assume three regimes of energies (see Figure 3.3) each with a different expression for the electron stopping cross-section. These energies are related to Bohr velocity, $v_0 \propto e^2/\hbar$, i.e. (2.2 x 10^6 m/s), where e and $\hbar$ are the electron charge and Plank's constant, respectively [Zie88].

In this region the electronic stopping cross section from Lindhard-Scharff formula is given by [Lin68]:

$$\varepsilon_e = 3.83 \frac{Z_1^{7/6} + Z_2}{\sqrt{(Z_1^{2/3} + Z_2^{2/3})^3}} \left(\sqrt{\frac{E}{M_1}}\right) \tag{3.21}$$

In second region (labeled as intermediate energies in Figure 3.3) the ion velocity is of the same order as Bohr's velocity, i.e. $v_i \approx v_0 Z_1^{2/3}$. As can be seen from Fig. 3.3, in this region the electronic stopping reaches a maximum. In this area, the ion velocity may have two regimes. For lower velocities, i.e. $1 \leq (v_i/v_0) \leq 5$, the ion velocity is greater than the Fermi velocity and the target inter-shell electrons can no longer be excited and the energy loss is confined mostly to interactions with the conduction electrons. In this part the electronic stopping cross section is the same as equation (3.21). For ion velocities greater than the substrate electron velocity the electronic stopping cross-section is calculated as same as the third region (higher velocity) [Zie88].

In the third region (labeled as high energies in Figure 3.3), $v_i \gg v_0 Z_1^{2/3}$. Here, the incident ion is fully stripped of its electrons. This area also is called Bethe-Bloch region. From their theory the energy loss is proportional to Z_1^2 [Bet30], [Blo33]. The electronic stopping cross section in this area is given by the formula below [Nas96]:

$$\varepsilon_e = \frac{2\pi e^4 Z_1^2}{E} N Z_2 \left(\frac{M_1}{m_e}\right) \ln\left(\frac{2 m_e v^2}{I}\right) \tag{3.22}$$

where N is the atomic density in the stopping target, m_e is electron mass, v_i is incident ion velocity. I is the average excitation energy (electron-volts) which for most elements (from Block's rule [Blo33]) is $\cong 10\, Z_2$ (Z_2 is the atomic number of stopping atoms).

Figure 3.4 shows the ion energy influence on the nuclear and electronic stopping for europium ion bombardment in glassy carbon. It can be seen that at low energies (< $E_{critical}$), nuclear stopping is the dominant stopping mechanism. At high energies (> $E_{critical}$) there is an opposite shift in energy loss mechanism and the electronic stopping is dominant. In this study, Eu ions were implanted at 250 keV which are lower than the critical energy value (1513 keV). The nuclear stopping, hence, was expected to be dominant during the implantation process.

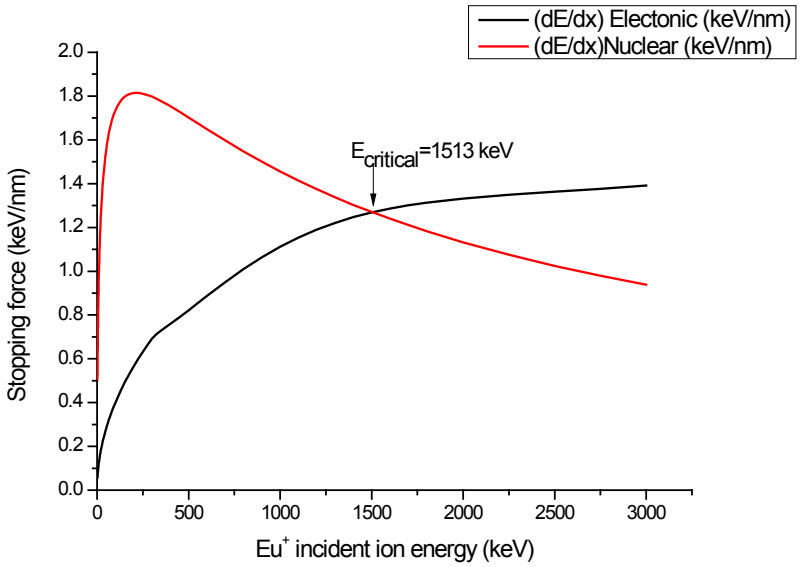

Fig. 3.4. Nuclear and electronic stopping plot for Eu^+ implanted in glassy carbon at room temperature obtained SRIM [Zie13]

3.3 ENERGY STRAGGLING

When an energetic ion penetrates into a target, it loses energy due to many interactions with target atoms. Identical energetic particles which all have the same initial energy, do not have the same energy after passing through a thickness of Δx in a homogenous target. It is due to different scattering angles of incident ions from interactions with target atoms. This phenomenon is known as energy straggling. Energy straggling places a limit on the precision with which energy loses can be determined and hence the depth resolution in backscattering spectroscopy, see Figure 3.5 [Chu78].

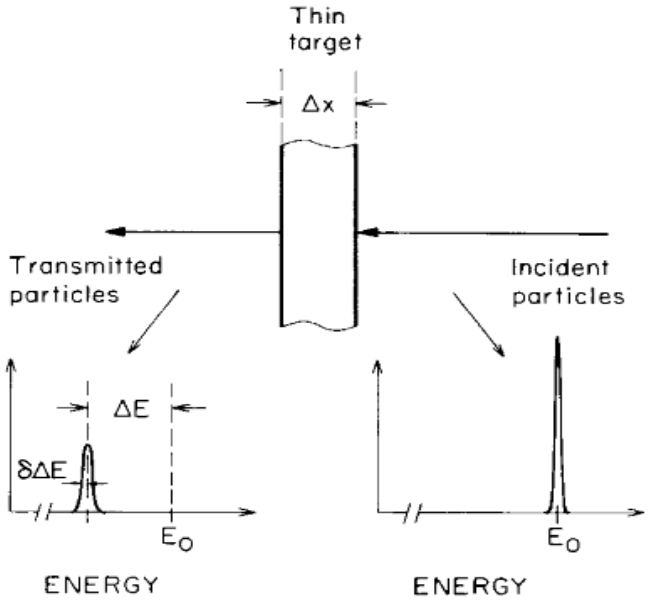

Fig. 3.5. A mono-energetic beam of energy E_0 loses energy ΔE after passing through the thickness of Δx. Obtained from [Chu78]

The simple classic model for energy straggling was introduced by Bohr in 1913 [Boh13]. Bohr's theory was assumed that [Har73]:

- Atoms in a target are randomly distributed.
- For a single interaction, the energy loss is much less than the whole energy loss over the total path.
- The projectile velocity is much higher than the electron velocity of the target atoms.

Then Bohr's model was extended by Lindhard and Scharff as follow [Wer06]:

$$\Omega^2 = 4\pi (Z_1 e^2)^2 N Z_2 t \qquad (3.23)$$

where Ω is energy straggling, t is a layer of thickness, Z_1 and Z_2 are the atomic mass of ion and target, respectively and N is atomic density. In this theory it was predicted that the energy straggling is independent of the beam energy. It depends on the electron density and atomic species [Chu78].

3.4 RANGE OF AN IMPLANT

As discussed in the previous sections, an implanted ion loses its energy by both electronic and nuclear interactions with target atom. The former encounters occur between the ion and target atom nuclei, while the electronic interactions are between the ion injected and the sea of electrons surrounding the target atom nuclei. For heavy ion implantations in the energy regime of ten to hundreds kilo electron volt, the nuclear stopping normally dominants and this is revealed in particular ion trajectories as ion comes to rest.

Knowing the stopping force and incident ion energy, E_0, the ion penetration depth can be estimated as below [Hic07], [Nas06], [Gib68]:

$$R = (1/N) \int_{E_0}^{0} \frac{dE}{dE/dx} \quad \rightarrow \quad R = (1/N) \int_{0}^{E_0} \frac{dE}{S_n(E)+S_e(E)} \tag{3.24}$$

Usually the implanted ion does not follow a straight trajectory till it comes to rest. The real path which ion passes is called range (R) and the straight distance which is perpendicular to the target surface is called projected range (R_p) [Nas06].

Because of ion scattering, the ion projected range (the ion range normal to the surface), R_p, is mostly smaller than the real ion range, R. This is due to a factor which is dependent on the scattering angles and the mean path of an individual ion (Figure 3.6). Furthermore, multiple collisions will cause an ion to deviate from its original path, making it to spread out. The average of all the ion ranges and ion projected ranges give the terms ion range R and projected range, R_p, for a particular substrate and ion with a specific initial energy.

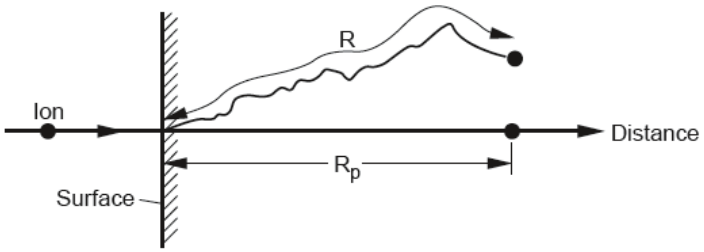

Fig. 3.6. An implanted ion with a particular path length R and projected range R_p. Obtained from [May70]

For a single element target, and for a light implanted ion ($M_1 \ll M_2$) the ratio R_p/R is $\ll 1$ due to high probability of backscattering of incident ion. This ratio is close to 1 for a heavy implanted ion ($M_1 \gg M_2$), because the heavy incident ion cannot be scattered backward but only forward [Tow87].

The depth distribution of monoenergetic, implanted ions and for moderate fluences in an amorphous substrate is approximately Gaussian in shape as shown in Figure 3.7 [Nas06].

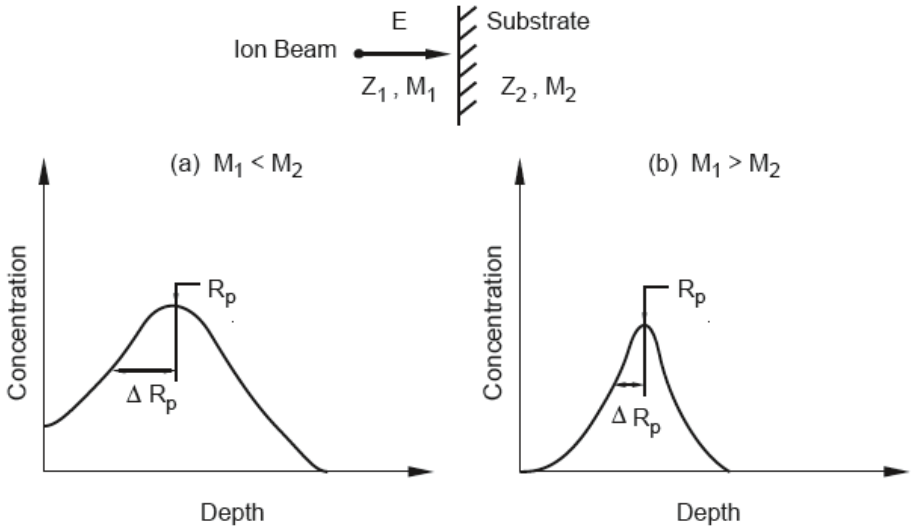

Fig. 3.7. The depth distribution of monoenergetic ions in an amorphous substrate (M_2) which is implanted by M_1 ions, in two cases; the ion mass is (a) less than target atom mass and (b) more than substrate mass atom. Obtained from [Nas06]

Due to the range straggling effect, the ion distribution profile as a function of depth is approximately Gaussian. The concentration of incident ions as a function of depth, x, is given as follows [Hic07]:

$$C(x) = C_p \exp\left(\frac{-(x-R_p)^2}{2\pi\Delta R_p^2}\right) \qquad (3.25)$$

where ΔR_p is the standard deviation of the distribution and C_p is the maximum concentration value/height in Gaussian ion distribution which is given by [Agu88]:

$$C_p = \frac{\varphi}{\sqrt{2\pi\, N\Delta R_p}} \qquad (3.26)$$

where the ion dose is φ (ion/cm^2) and the target atomic density is N. The range straggling is defined by:

$$\Delta R_p = 1/\varphi \int_{-\infty}^{\infty} (x - R_p)^2 \, C(x) \, dx \tag{3.27}$$

To characterize an implanted profile the following four parameters are usually applied, viz. the projected ion range (R_p), range straggling (ΔR_p), skewness (γ) and kurtosis (β). Skewness is defined as the asymmetry of the ion distribution profile to the Gaussian peak, while kurtosis is described as the contribution ion distribution profile tail over the flatness of the profile shape, with the values of γ and β is given by [Hic07]:

$$\gamma = \frac{\int_{-\infty}^{\infty} (x - R_p)^3 \, C(x) dx}{\varphi \Delta R_p^3} \tag{3.28}$$

$$\beta = \frac{\int_{-\infty}^{\infty} (x - R_p)^4 \, C(x) dx}{\varphi \Delta R_p^4} \tag{3.29}$$

The room temperature europium implanted depth profile in glassy carbon is shown in Figure 3.8. This profile was fitted to the Edgeworth distribution (to acquire the experimental values of R_p, ΔR_p, γ and β) given by:

$$N(x) = A \, f(x) e^{\left[\frac{(x - R_P)^2}{2\Delta R_p^2}\right]} \tag{3.30}$$

$$f(x) = 1 + \frac{\gamma}{6}\left[\left(\frac{x - R_p}{\Delta R_p}\right)^3 - 3\left(\frac{x - R_p}{\Delta R_p}\right)\right] + \frac{\beta - 3}{24}\left[\left(\frac{x - R_p}{\Delta R_p}\right)^4 - 6\left(\frac{x - R_p}{\Delta R_p}\right)^2 + 3\right] \tag{3.31}$$

From the fit the R_p and ΔR_p values acquired were 125 nm and 35 nm, respectively. Also the skewness and kurtosis were measured as 0.18 and 2.87, respectively.

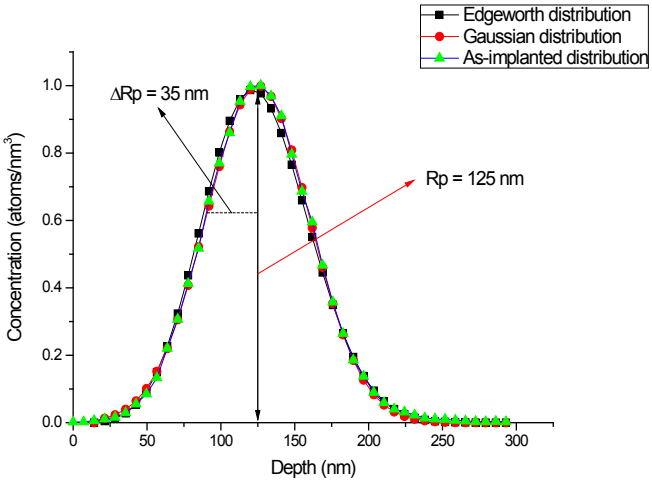

Fig. 3.8. Normalized distribution of 250 keV europium implanted in glassy carbon at room temperature as a function of depth. Values were obtained by fitting the as-implanted europium depth profile with a Gaussian distribution.

In Figure 3.8, the depth distribution of our as-implanted 250 keV europium ions in glassy carbon is given. Also depicted are the fits of a Gaussian and the Edgeworth functions to this distribution. As can be seen from the figure, within the resolution on the line thicknesses, these three curves agree with each other. This means that our as-implanted Eu has a Gaussian form. As will be discussed in the next chapter, this is a crucial point to allow the determination of the diffusion coefficient from our Rutherford Backscattering Spectrometry (RBS) depth profiles. In Chapter 7, we shall return to our as-implanted profiles to discuss them further.

3.5 IMPLANTATION INDUCED DEFECTS

Ion implantation causes the formation of damage. Radiation damage is produced when an energetic particle transfers sufficient energy to the target atoms to displace them from their lattice sites. Nuclear and electronic stopping forces are responsible for the energy loss. During the elastic (nuclear stopping) collisions, the energy lost by the implanted ion, is transferred from the incident ion to the target atom which results in it recoiling away from its lattice site and creating a defect site. To do this, incident ions need to have energy higher than the displacement energy (E_d) of the atoms in the target. In fact, by ion implantation the target lattice structure will be damaged. Also

ion implantation process produces some defects. Most damage in crystals is as a result of nuclear stopping due to ion implantation while the electronic stopping are responsible for damage in alkali halides when excitation energy is sufficient to form defects in the halogen substrates [Tow87]. The level of radiation damage during ion implantation depends on some factors such as type of ion, kind of target, implantation temperature and implantation fluence [Buk14], [McC94], [Lan12].
In crystals the defects are categorized as point defects, linear defects, planar defects, and volume defects [Nas06].

Table 3.1. Examples of defects due to ion implantation [Nas06].

Type of defect	**Examples**
Point	Vacancies, interstitials, impurity atoms
Line	Dislocations
Plane	Stacking faults, twins, grain boundaries
Volume	Precipitates and voids

Point defect is derived from a single point deviation in a periodic lattice. Other defect types such as dislocation, stacking faults and etc. extend through the lattice. Point defects are also formed due to thermal treatment, crystal growth and mechanical processes. Point defects are classified into two types (see Figure 3.9):

a) Native defects such as vacancies, interstitials.

b) Impurity-related defects which comes from any impurity in the lattice.

A Frenkel defect is formed when an atom is knocked out from its lattice site to a nearby interstitial position. The vacancy is the empty lattice site. Self-interstitial atom is defined as an occupied substrate lattice position by a substrate atom. Substitutional defects come from the occupied lattice site by an impurity atom (such as shallow dopant), e.g. As in Si. The vacancies and interstitial defects are formed in ion implanted materials [Nas06], [Gib72].

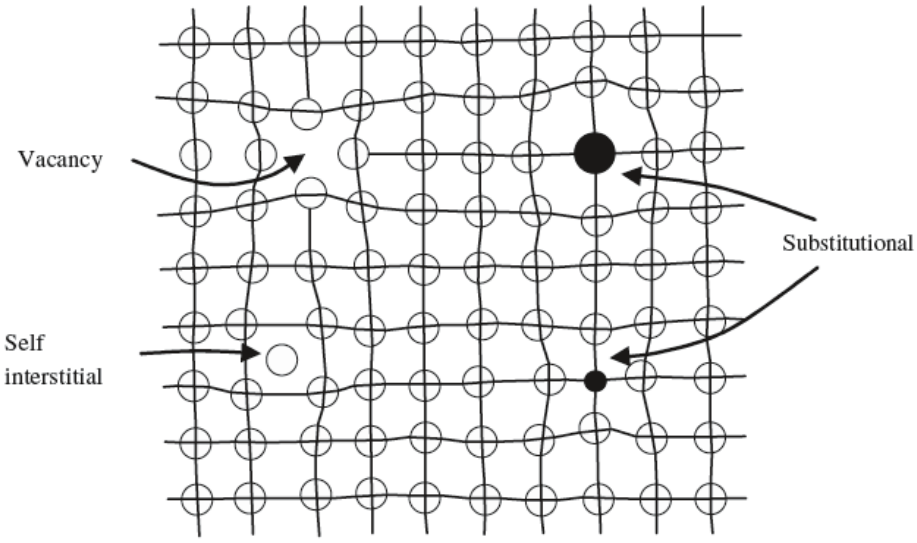

Fig. 3.9. Various point defects in a two-dimensional simple cubic lattice. Obtained from [Nas06]

In amorphous materials, the presented defects are the open volume defects (pores) such as vacancies or devacancies as well as the interstitials [Wil10]. The metallic glass which are known as amorphous materials (containing Fe, Ni or Co) also have their favorable properties (such as hardness and high tensile strength) due to lack of defects such as dislocations and grain boundaries [Meh07].

3.6 AMORPHISATION DUE TO ION IMPLANTATION

Ion implantation causes damage in materials. If the damage is beyond a certain point, it will cause the formation of an amorphous layer. During the ion implantation a disorder region is produced by each incident ion. Increasing the ion dose leads to an increase in the disorder untill all atoms have been displaced and an amorphous layer (over a depth of R_p) is generated [Nas06].

Amorphisation in a crystal solid occurs if the point defects concentration exceed over a critical value. This will change the material from crystalline into an amorphous phase. Amorphisation due to ion implantation leads to change in the material density. It is a complicated phenomenon due to

its high dependency on the dose rate, mass of the incident ion, mass of the target, energy and the temperature [Hic07].

Generally two theories were considered for amorphisation due to ion implantation. First when materials are irradiated by energetic ions, the ion induced disorder can result in a number of structural transformations, including crystallization and amorphisation. Irradiation in higher temperatures (higher than the room temperature) leads to increase the mobility of defects produced by ion beam. Second when irradiation is carried out at or lower than the room temperature, the produced disorder is stable because point defects are easily immobilized in the disordered region. In this situation, generated ion damage within the collision cascades builds up with ion dose, resulting in amorphisation in materials. At higher implant temperatures, defects start to move and interact during ion bombardment resulting in the annihilation of defects and it can be difficult to induce amorphisation [Wil10]. In this regime, amorphisation may occur at such as, at surfaces or at nano-cavities [Ave98]. Continued irradiation can lead to amorphisation layer by layer; however at higher temperature irradiation may not cause the amorphisation. In complete destroying of defects during ion implantation can lead to the formation of cluster defects (also may results in extended defects in other crystal matrix). Irradiation at higher temperature may lead to the recrystallization of previously amorphised layer [Wil10].

Some investigations show that by ion implantation the density of glassy carbon increases from 1.42 to 2.02 $\pm$ 0.2 g/cm^3 [Odu18], [Pie93]. Increasing the density by ion implantation results in the improvement of the wear resistance [Iwa89], [McC93], [McC94]. Thus, the wear resistance of glassy carbon could be improved by the ion implantation process.

In next Chapter (Chapter 4) the role of defects in diffusion will be discussed.

3.7 SIMULATED EUROPIUM ION IMPLANTATION IN GLASSY CARBON

The computer code SRIM (stopping and ion range in matter) [Zie13] is a common tool which is widely applied to simulate ion implantation distributions and damage in a target. It has been applied by some researchers [Ism18], [Odu18], [Njo17], [Hla14] to estimate theoretically the depth

of implanted ions and their distribution in solids such as Si and GC. In this study, the SRIM program was used to predict the behavior of europium implanted in glassy carbon. Then the obtained experimentally obtained values from Rutherford backscattering spectrometry (RBS), were compared with the predicted ones.

SRIM simulation program uses a binary collision algorithm and Monte Carlo method to estimate the ion implanted depth distribution (see Figure 3.10). This program does not consider the crystal structure and dynamic composition changes in target when the ion penetrates into the material. Some assumption made by SRIM are: [Zie13]

- ✓ The projected range prediction is only carried out by the simulation of a binary collision, and it neglects the effect of neighboring atoms.
- ✓ This program considers the target as an amorphous material.
- ✓ Recombination between vacancies and interstitial defects is ignored.

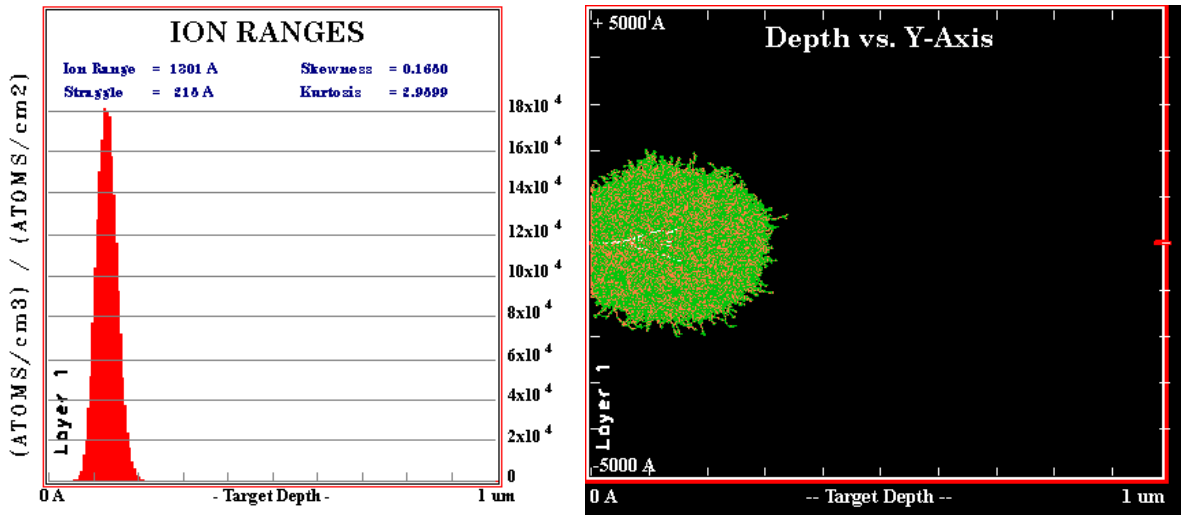

Fig. 3.10. SRIM [Zie13] simulation ion distribution (left) and ion trajectories (right) of 250 keV europium implanted in glassy carbon

REFERENCES

[Agu88] F. Agullo-Lopez, C. R. A. Catlow, P. D. Townsend, "Point defects in materials ", Academic press, 1988.

[Ave98] R. S. Averbach, T. Diaz de la Rubia, "Displacement damage in irradiated metals and semiconductors", Solid state physics, pp. 51, 1998.

[Bac12] M. Backman, "Effects of nuclear and electronic stopping power on ion irradiation of silicon-based compounds", Available at: https://helda.helsinki.fi/bitstream/handle, 2012.

[Bet30] H. Bethe, "To the theory of the passage of fast corpuscular rays through matter", Annals of physics, Wiley online library, (397), pp. 325–400, 1930.

[Blo33] F. Bloch, "For braking rapidly moving particles when passing through matter", Annals of physics, Wiley online library, 16, pp. 285, 1933.

[Boh13] N. Bohr, D. Phil, "On the theory of the decrease of velocity of moving electrified particles on passing through matter", The Philosophical Magazine: A Journal of Theoretical Experimental and Applied Physics, Taylor & Francis Online, 25(145), pp. 10–31, 1913.

[Buk14] S. S. Bukalov, Y. V. Zubavichus, L. A. Leites, A. I. Sorokin, A. S. Kotosonov, "Structural changes in industrial glassy carbon as a function of heat treatment temperature according to Raman spectroscopy and x-ray", Nanosystems: Physics, Chemistry, Mathematics, 5(1), pp. 186–191, 2014.

[Chu78] W. K. Chu, J. W. Mayer, M. A. Nicolet, "Backscattering Spectroscopy", Journal of Vacuum Science and Technology, 1978.

[Fer47] E. Fermi, E. Teller, "The capture of negative mesotrons in matter", Physical Review, 72(5), 1947.

[Fir58] O. B. Firsov, "Scattering of ions by atoms", Soviet Physics JETP, 34(7), pp. 308, 1958.

[Gib68] J. F. Gibbons, "Ion implantation in semiconductors (Part I): Range distribution theory and experiments", Proceedings of the IEEE, 56(3), pp. 295–319, 1968.

[Gib72] J. F. Gibbons, "Ion implantation in semiconductors (Part II): Damage production and

annealing", Proceedings of the IEEE, 60(9), pp. 1062–1096, 1972.

[Har73] J. M. Harris, W. K. Chu, M. A. Nicolet, "Energy straggling of ^{4}He below 2 MeV in Pt", Thin solid film, Elsevier Sequoia, (19), pp. 259–265, 1973.

[Hic07] D. P. Hickey, "Ion implantation induced defect formation and amorphization in the Group IV semiconductors: Diamond, silicon and germanium", Available at: http://etd.fcla.edu, 2007.

[Hla14] T. T. Hlatshwayo, N. G. van der Berg, M. Msimanga, J. B. Malherbe, R. J. Kuhudzai "Iodine assisted retainment of implanted silver in 6H-SiC at high temperatures", Nuclear Instruments and Methods in Physics Research, Section B: Beam Interactions with Materials and Atoms, 334, pp. 101–105, 2014.

[Ism18] M. Y. A. Ismail, J. B. Malherbe, O. S. Odutemowo, E.G. Njoroge, T.T. Hlatshwayo, M. Mlambo, E. Wendler, "Investigating the effect of heat treatment on the diffusion behaviour of xenon implanted in glassy carbon", Vacuum, 149, pp. 74–78, 2018.

[Iwa89] M. Iwaki, K. Takahashi, K. Yoshida, Y. Okabe, "Improvement of wear properties of glassy carbon surface layer modified by ion implantations", Nuclear Inst. and Methods in Physics Research, B, 39(1–4), pp. 700–703, 1989.

[Lan12] D. F. Langa, N. G. van der Berg, E. Friedland, J. B. Malherbe, A. J. Botha, P. Chakraborty, E. Wendler, W. Wesch, "Heat treatment of glassy carbon implanted with cesium at room and high temperatures", Nuclear Instruments and Methods in Physics Research, Section B: Beam Interactions with Materials and Atoms, 273, pp. 68–71, 2012.

[Len84] W. N. Lennard, D. Phillips, I. V. Mitchell, "Search for pre-equilibrium stopping for ^{4}He ions in thin carbon foils", Nuclear Instruments and Methods in Physics Research B, 2, pp. 116–118, 1984.

[Lin54] J. Lindhard, "On the properties of a gas of charged particles", Dan. Vid. Selsk Mat.-Fys, 8(28), 1954.

[Lin68] J. Lindhard, V. Nielsen, M. Scharff, "Approximation method in classical scattering by screened coulomb fields", Matematisk-Fysiske Meddelelser, 1968.

[May70] J. W. Mayer, L. Eriksson, J. A. Davies, "Ion implantation in semiconductors", Academic,

New York, 1970.

[McC93] D. McCulloch, S. Prawer, A. Hoffman, D. K. Sood, "Cross-sectional transmission electron microscopy investigation of xenon irradiated glassy carbon", Nuclear Inst. and Methods in Physics Research, B, 80–81(PART 2), pp. 1480–1484, 1993.

[McC94] D. McCulloch, S. Prawer, A. Hoffman "Structural investigation of xenon-ion-beam-irradiated glassy carbon", Physical Review B, 50, p. 5905, 1994.

[Meh07] H. Mehrer, "Diffusion in solids: fundamentals, methods, materials, diffusion-controlled processes", Springer series in solid-state sciences, 2007.

[Nas96] M. Nastasi, J. Mayer, J. K. Hirvonen, "Ion-Solid Interactions: Fundamentals and Applications", Cambridge university press, 1996.

[Nas06] M. Nastasi, J. W. Mayer, "Ion Implantation and Synthesis of Materials", Springer, 2006.

[Njo17] E. G. Njoroge, L. D. Sebitla, C. C. Theron, M. Mlambo, T. T. Hlatshwayo, O. S. Odutemowo, V. A. Skuratov, E. Wendler, J. B. Malherbe, "Structural modification of indium implanted glassy carbon by thermal annealing and SHI irradiation", Vacuum, 144, pp. 63–71, 2017.

[Odu18] O. S. Odutemowo, J. B. Malherbe, L. C. Prinsloo, E. G. Njoroge, R. Erasmus, E. Wendler, A. Undisz, M. Rettenmayr, "Structural and surface changes in glassy carbon due to strontium implantation and heat treatment", Journal of Nuclear Materials, 498, pp. 103–116, 2018.

[Pie93] H. O. Pierson, "Handbook of carbon, graphite, diamond and fullerenes: Properties, processing and applications", Noyes, 1993.

[Tow87] P. D. Townsend, "Optical effects of ion implantation", Reports on Progress in Physics, 50(5), 1987.

[Was07] G. S. Was, "Fundamentals of Radiation Materials Science : Metals and Alloys", New York: Springer science, 2007.

[Wer06] M. Werner, "Damage formation and annealing studies of low energy ion implants in silicon using medium energy ion scattering", Ph.D thesis, University of Salford, UK, 2006.

[Wil10] J. S. Williams, H. Bernas, "Ion-beam-induced amorphization and epitaxial crystallization

of silicon", Topics in applied physics; Materials science with ion beams, 116, pp. 73–111, 2010.

[Www18] www.google.com, "Nuclear and Electronic stopping power cross-section", 2018.

[Zie88] J. F. Ziegler, "Ion Implantation Science and Technology″, San Diego: Academic press, 1988.

[Zie13] J. F. Ziegler, "www.SRIM.org", USA, 2013.

[Zie85] J. F. Ziegler, J. P. Biersack, U. Littmark, "The stopping and range of ions in solids", Pergamon Press, New York, 1985.

CHAPTER 4

DIFFUSION AND SEGREGATION IN SOLIDS

Diffusion is defined as a mass transport process which is driven by a concentration (atom/molecules) gradient. This also happens in a substrate due to random molecular motions with the driving force being the minimization of the free Gibbs energy. Diffusion is influenced by thermal and/or mechanical energy and the difference in concentration between constituent molecules/atoms. Diffusion process in solids is much slower than in liquids and gases and equilibrium may not be reached in sensible periods of time (especially at lower temperatures). Increasing the time leads to better mixing of elements into the medium by the diffusion process and results in increased homogeneity [Wil00], [Gli99]. Mostly microstructure changes and chemical reactions occur due to diffusion processes.

4.1 DIFFUSION

In the condensed states, diffusion is known to occur due to a random process in which atoms or molecules are able to exchange position with neighbors due to random fluctuations. There are several processes which can lead to the displacement of atoms in a solid state substrate and subsequently promote diffusion. Two general processes are responsible for the diffusion, viz. volume diffusion (diffusion via lattice) and short circuits (diffusion via surface diffusion and grain boundaries) [Njo14]. Certain diffusion processes in solids occur due to the presence of defects in their solid structure. In Chapter 3, we said that ion implantation causes atomic replacement and mobility which lead to the formation of defects.

4.1.1 VOLUME/LATTICE DIFFUSION

Volume/lattice diffusion takes place by the movement of point defects through the lattice structure. Understanding the migration of defects at an atomic level is achieved by the theory of lattice defects. There are different types of point defects (as mentioned in Chapter 3) such as vacancy,

interstitial and impurity atoms [All87]. We will briefly discuss three common forms of the lattice diffusion mechanisms in the next sub-sections.

4.1.1.1 VACANCY DIFFUSION MECHANISM

Vacancies are not only presented in pure metals and alloys at all temperatures but also exist at a concentration of about 0.01% at the melting temperature [Gup04]. Vacancies play an important role in all process related to solid state diffusion, including grain growth, sintering, recrystallization and phase transformation [Ohr92]. If an impurity atom jumps into vacancy, see Figure 4.1, the atom diffuses via the vacancy mechanism. Of course the diffusion is opposite of the vacancy movement [Will78]. This movement leads to the breaking of bonds and new bonds to be formed. The probability of such an event is exp $(-E_f/k_BT)$, where E_f is the energy value of formation a vacancy in the lattice, k_B is Boltzmann's constant and T is absolute temperature [Nas06].

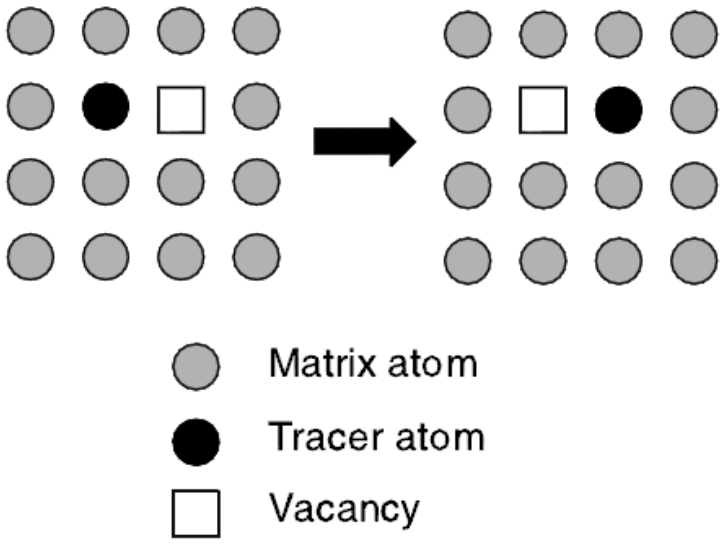

Fig. 4.1. Vacancy diffusion mechanism. Taken from [Meh07]

In amorphous materials it has been speculated that the diffusion occurs through the trapping of defects into pre-existence defects, surfaces or amorphous layers [Wil10]. Amorphous materials

may also have defects. Naturally it is not easy to define these defects. However, defects in amorphous solids can be defined on basis of the empty or densely packed local atomic neighborhoods. The properties of such defects can be shown to be similar to normal vacancies and interstitials in crystals [May03], [Nor05], [Ash12].

4.1.1.2 INTERSTITIAL DIFFUSION MECHANISM

In the interstitial mechanism (so-called direct interstitial mechanism), diffusion occurs by migration of species directly from one interstitial to another. In this case, the interstitial atom does not need a neighboring defect (such as vacancy) to jump into. Diffusion can easily take place by movement of interstitial sites (as shown in Figure 4.2) [Gup04], [Kos01]. In an impure solid, a solute atom which is considerably smaller than the host atoms can move interstitially through the lattice and nearly all interstitial atoms are separated from one another. With regards to diffusion, it means that the neighboring interstitial sites around a particular solute atom are often vacant. Therefore, these sites are available for a solute atom to jump into [Meh07]. For example, in the case of noble metals such as Cu and Au in the matrices of Pb and Sn (in group IV), it is believed that the rapid migration takes place through the interstitial sites [Ohr92]. Due to high required energy for the formation of interstitials in metals, the equilibrium concentration of interstitials is very small. Thus, in most cases, their contribution in diffusion is not important [Kos01].

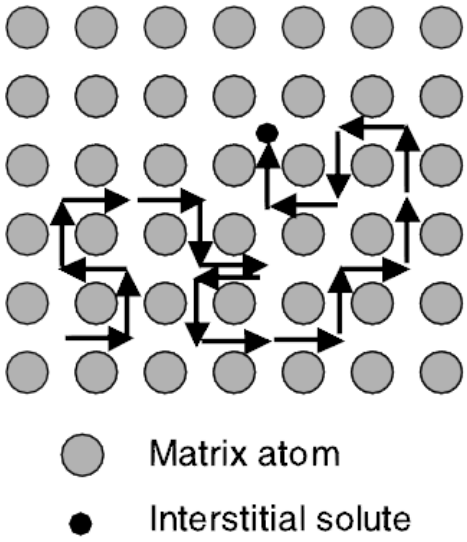

Fig. 4.2. Direct interstitial diffusion mechanism. Taken from [Meh07]

4.1.1.3 INTERSTITIALCY DIFFUSION MECHANISM

Interstitialcy diffusion occurs when a large atom (larger than the host atoms) or nearly in same size as the host lattice atom moves into an interstitial position. This migration produces a very large distortion in the lattice structure [Wil78]. In this mechanism (so-called indirect interstitial mechanism), a regular host atom moves to an interstitial position in target lattice whereas the interstitial impurity atom moves to a regular lattice atom site, see Figure 4.3. This mechanism probably takes place in materials with relatively large lattice constants (large voids) such as the anion lattice in the fluorite structure. In materials with high concentrations of interstitials, which may be introduced by irradiation (in metals) or doping (in oxides), interstitialcy diffusion dominates. This mechanism is negligible for diffusion at relatively low temperatures in metals. This is due to formation enthalpies of self-interstitials being higher than the formation enthalpies of vacancies [Meh07], [Kos01].

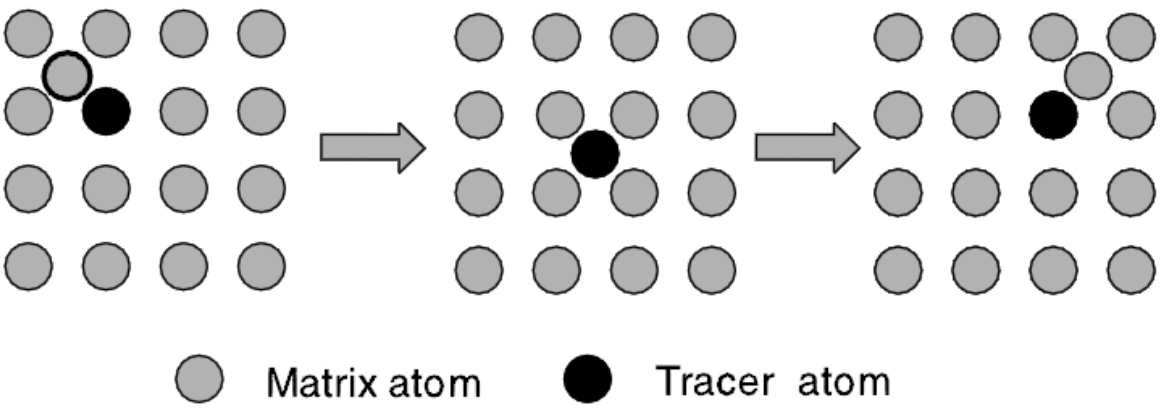

Fig. 4.3. Interstitialcy diffusion mechanism. Taken from [Meh07]

4.1.2 SHORT CIRCUIT DIFFUSION MECHANISM

Diffusion through grain boundaries, dislocations and surface diffusion causes the short circuit diffusion mechanism. This mechanism usually results in more rapid diffusion of impurities in a polycrystalline material compared to single crystal [Kiz99]. In solids, at lower annealing temperatures, e.g. up to and below 0.3 – 0.5 T_{mp} (melting point temperature), grain boundary (a short circuit diffusion mechanism) diffusion dominates the volume diffusion. At 0.5 T_{mp}, the short circuit diffusion is usually 5 to 6 orders of magnitude faster than volume diffusion [Lau03]. In modern technology short circuit diffusion is important because in many microelectronic devices depends on this type of diffusion. The short circuit diffusion is the diffusion process that affects the diffusion barrier between thin film layers in devices [Kum08].

4.2 MATHEMATICS OF DIFFUSION

In non-equilibrium thermodynamic systems, there is a naturally driving force to push materials toward the equilibrium. The flux of atoms diffusion, J, is a measure of how fast atoms diffuse. Flux is defined as the number of atoms or the mass of atoms (M) which diffuses through the unit area (A) and per unit time (t), see Figure 4.4. This is given by [Njo14]:

$$J = \frac{1}{A}(dM/dt) \qquad (4.1)$$

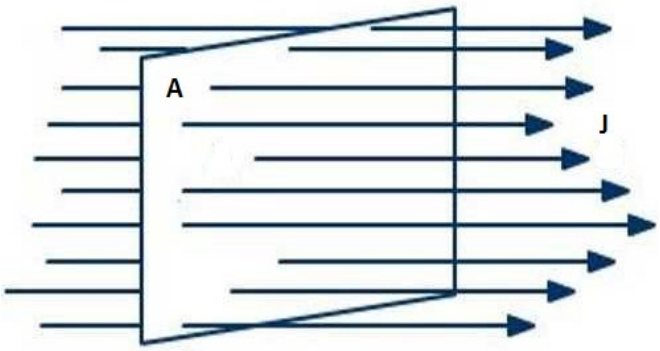

Fig. 4.4. Flux J through the unit area A. Taken from [www18]

In solids, the mass transportation is achieved by diffusion which is defined as the migration of molecular or atomic species due to a concentration gradient (from high concentration regions to low concentration regions) [Ohr92]. In solid state diffusion, flux (we shall return to give a fundamental and conventional definition) is given by the following relationship:

Flux = (diffusivity) x (concentration gradient)

Diffusivity or diffusion constant, D, is related to the atom/mass diffusion in solids, i.e. the movement of diffusing atom in a sample.

The diffusion process is classified into two types; steady state and non-steady state. Steady state diffusion is a time independent process and occurs at a constant rate. It means, the concentration does not change with time i.e. $dC/dt = 0$ and dC/dx = constant. Since solid state diffusion is a slow process, it is usually assumed to be the case in order to treat it by Fick equations which are discussed below. In contrast to steady state diffusion, a non-steady state diffusion process is dependent on the time. In this process, the concentration also varies by distance, i.e. $dC/dx \neq$ constant and $dC/dt \neq 0$ [Meh07], [Jac04]. Both states are described by Fick's law. The Fick's first law will be applied for both steady and non-steady state diffusions. But the Fick's second law only deals with the non-steady state diffusion.

4.2.1 FICK'S FIRST LAW (STEADY STATE DIFFUSION)

The usual representation of a diffusion process is provided by Fick's first law [Fic55] which is similar to the heat conduction law, i.e. flow is from the high concentration region to the low concentration region. For steady state diffusion, the connection between the concentration and diffusional transportation (in one dimension) is given by Fick's first law as following [Kos01]:

$$J = - D (dC/dx) \qquad \text{(atoms or ions or moles/cm}^3\text{)} \qquad (4.2)$$

where J is the flux, C is concentration, D is the diffusion coefficient (which will be discussed in the next section of this chapter) and x is the distance of atomic migration. The minus sign is due to the opposite directions of the atomic flux and the concentration gradient. The unit of diffusion flux is determined as the number of particles (or moles) travelling perpendicular to a unit area per unit time and concentration is the number of particles per unit volume.

Therefore, the unit of diffusivity is given as length^2 per unit time (typical units are cm^2/s or m^2/s). Equation (4.2) states that the diffusion flux tends towards zero as the sample becomes homogenous. In three dimensions the Fick's first law is generalized as below [Meh07]:

$$J = - D \nabla C \qquad (4.3)$$

In solid state diffusion measurements the Fick's first law is not useful due to the time dependency of concentration. It is only possible to measure the flux when the concentration does not change with time and the sample is in steady state [She89].

4.2.2 FICK'S SECOND LAW (NON-STEADY STATE DIFFUSION)

In real diffusion, the concentration gradient changes with both time and distance. It means the concentration is a function of distance, x, and time, t. This is referred to non-steady state diffusion. Therefore, this needs a new law and equation. The new law is known as Fick's second law and is derived from the first law, i.e. equation (4.2). Consider a volume element of a bar of a material with cross section A and a small length dx, then according to Figure 4.5 [Cam01]:

$$\frac{J_2 - J_1}{dx} = \frac{\Delta J}{\partial x} \qquad (4.4)$$

where J_1 is the flux entering the volume and J_2 is the flux leaving the volume. The concentration of the diffusing species in the volume will change if $J_1 \neq J_2$.

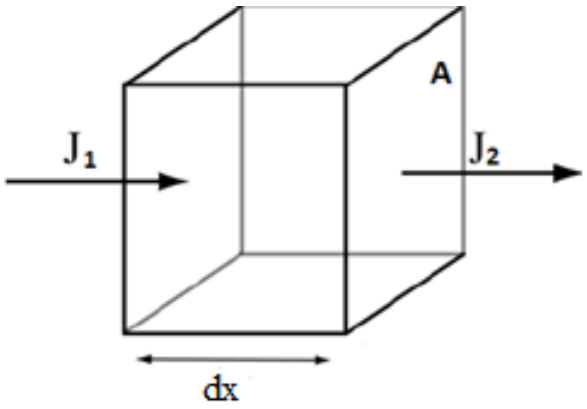

Fig. 4.5. A differential volume element of a bar with cross sectional area A. J_1 and J_2 are the entering and leaving flux, respectively. Obtained from [Cam01]

Note that the concentration in this volume is related to the cross sectional area and length, i.e. A.dx. Then the continuity equation is expressed as:

$$(A\ dx)\frac{\partial C}{\partial t} = -A\ (J_2 - J_1) = -(A\ \partial x)\frac{\partial J}{\partial x} \tag{4.5}$$

Equation (4.4) is also can be written as:

$$-\frac{\partial J}{\partial x} = \frac{\partial C(x.t)}{\partial t} \tag{4.6}$$

The Fick's first law in three dimensional is expressed as:

$$-\nabla J = \frac{\partial C(r,t)}{\partial t} \tag{4.7}$$

Inserting the J from the Fick's first law, i.e. equation (4.2), into (4.6) gives Fick's second law:

$$\frac{\partial}{\partial x}\left(D\frac{\partial C}{\partial x}\right) = \frac{\partial C(x.t)}{\partial t} \tag{4.8}$$

If the diffusion coefficient is independent of x (which is usually the case), then the equation (4.8) will be reduced to:

$$D\frac{\partial^2 C}{\partial x^2} = \frac{\partial C(x.t)}{\partial t} \quad (4.9)$$

The Fick's second law in three dimensional is expressed by:

$$D\nabla^2 C = \frac{\partial C(r,t)}{\partial t} \quad (4.10)$$

In limited temperature ranges, the diffusion coefficient approximately follows the Arrhenius equation:

$$D = D_0 \exp(-E_a/k_B T) \quad (4.11)$$

where D_0 is the temperature independent pre-exponential factor, E_a is the activation energy, k_B is Boltzmann's constant and T is the temperature in Kelvin.

Generally, most diffusion measurements in solids are based on the second Fick's law. It has been used in thin film, rods and plate samples geometry. It has also been applied to measure the diffusion along grain boundaries and dislocations in single crystal specimens [Gup04].

4.3 DETERMINING THE DIFFUSION COEFFICIENT

Several methods have been used to generally solve the diffusion equation (4.8) for the diffusion coefficient [Ste11]. The general solution for low concentrations of the diffusing impurity ($0 < x < \infty$) is given by Boltaks [Bol63]:

$$N(x,t) = \frac{1}{2\sqrt{\pi Dt}} \int_0^\infty \left[N(\xi,0)\exp\left(-\frac{(\xi-x)^2}{4Dt}\right) + N_I(-\xi,0)\exp\left(-\frac{(\xi+x)^2}{4Dt}\right)\right] d\xi \quad (4.12)$$

where N(x,t) is the number of diffusing particles per unit volume at time t at the distance x below the surface. The $N(\xi,0)$ is the original impurity distribution and $N_I(\xi,0)$ is the function which is determined from boundary conditions. Assuming N_0 is the number of diffusing particle per unit volume at $t > 0$ and x = 0 and it is constant and given by:

$$N_0 = N(0,t) = \frac{1}{2\sqrt{\pi Dt}} \int_0^\infty [N(\xi,0) + N_I(-\xi,0)]\exp\left(-\frac{(\xi)^2}{4Dt}\right) d\xi \quad (4.13)$$

For an isotropic material implanted with a mono energetic impurity atoms (such as in this study) the initial implanted profile is assumed to be Gaussian with projected range (R_p) and range straggling (ΔR_p) given by:

$$N(\xi,0) = A_0 \exp\left[\frac{-(\xi-R_p)^2}{2\Delta R_p^2}\right] \tag{4.14}$$

Malherbe *et al*. [Mal17] determined the following solution for equation (4.9):

$$N(x,t) = \frac{A_0 \Delta R_p}{2\sqrt{2Dt+\Delta R_p^2}} e^{\left[-\frac{(x-R_p)^2}{4Dt+2\Delta R_p^2}\right]} \left[1 + \operatorname{erf}\left[\frac{2DtR_p + x\Delta R_p^2}{\Delta R_p \sqrt{2(2Dt)^2+4Dt\Delta R_p^2}}\right] - k e^{\left[-\frac{xR_p}{Dt+\Delta R_p^2/2}\right]} \left\{1 + \operatorname{erf}\left[\frac{2DtR_p - x\Delta R_p^2}{\Delta R_p \sqrt{2(2Dt)^2+4Dt\Delta R_p^2}}\right]\right\}\right] \tag{4.15}$$

where k is a constant ($-1 < k < 1$) and is given by:

$$k = 1 - \left[\frac{\left[\frac{2C_0\sqrt{2Dt+\Delta R_p^2}}{A_0.\Delta R_p} \exp\left(\frac{R_p^2}{4Dt+2\Delta R_p^2}\right)\right]}{1+\operatorname{erf}\left[\frac{R_p\sqrt{Dt}}{\Delta R_p\sqrt{2Dt+\Delta R_p^2}}\right]}\right] \tag{4.16}$$

There are two special cases for k. k = 1 represents a perfect sink at the substrate meaning that the arrived impurity at the surface is immediately sublimated while k = -1 represents a perfect reflecting boundary at x = 0 and zero flux at origin meaning no impurity is lost from the surface. In our calculations, k was a fitting variable.

4.4 SEGREGATION IN SOLIDS

Surface segregation is a phenomenon of the enrichment of an impurity from the bulk of the substrate to its surface, interfaces or grain boundaries. The difference between the chemical potential of the bulk and of the surface of a given sample is the fundamental reason for segregation. The segregation enrichment depends on the concentration of component in the bulk, the temperature and the time during which segregation takes place. The impurities brought to the

surface by diffusion from bulk as well as impurities adsorbed by the sample from the ambient environment can also affect the segregation process [Dow87].

REFERENCES

[All87] A. R. Allnatt, A. B. Lidiard, "Statistical-theories of atomic transport in crystalline solids", Reports on progress in physics, 50(4), pp. 373–472, 1987.

[Ash12] Y. Ashkenazy, R. S. Averback, "Irradiation induced grain boundary Flow: A new creep mechanism at the nanoscale", Nano Letters, 12(8), pp. 4084–4089, 2012.

[Bol63] B. I. Boltaks, "Diffusion in semiconductore*s*", London: Infosearch Limited, 1963.

[Cam01] S. A. Campbell, "The Science and Engineering of Microelectronic Fabrication", Oxford University Press, pp. 688, 2001.

[Dow87] P. A. Dowben, A. H. Miller, R. W. Vook, "Surface segregation from gold alloys", Gold Bulletin, 20(3), pp. 54–65, 1987.

[Fic55] A. Fick, "Annalen der Phyik und Chemie", Philosophical Magazine, 1855.

[Gli99] M. E. Glicksman, "Diffusion in Solids: Field Theory, Solid-State Principles, and Applications", New York, Wiley, 1999.

[Gup04] D. Gupta, "Diffusion Processes in Advanced Technological Materials*″*, New York: Springer- Andrew William, Inc., 2004.

[Jac04] K. A. Jackson, "Kinetic Processes; Crystal Growth, Diffusion, and Phase Transitions in Materials, Phase Transitions". Wiley-VCH Verlag GmbH & Co, 2004.

[Kiz99] M. Kizilyalli, J.Corish, R. Metselaar, "Definitions of Terms for Diffusion in the Solid State", Pure and Applied Chemistry, 71(7), 1999.

[Kos01] G. Kostorz, "Phase Transformations in Materials, Computational Materials Science". Edited by E. Lifshin and D. Raabe. Zürich: WILEY-VCH Verlag GmbH,Weinheim, 2001.

[Kum08] S. P. Kumar, "Diffusion Barriers in Semiconductor Devices/Circuits", William andrew, Inc.*,* pp. 239–281, 2008.

[Lau03] T. Laurila, J. Molarius, "Reactive Phase Formation in Thin Film Metal/Metal and Metal/Silicon Diffusion Couples", Critical Reviews in Solid State and Materials Sciences, 2003.

[Mal17] J. B. Malherbe, P. A. Selyshchev, O. S. Odutemowo, C. C. Theron, E. G. Njoroge, D. F.

Langa, T. T. Hlatshwayo, "Diffusion of a mono-energetic implanted species with a Gaussian profile", Nuclear Instruments and Methods in Physics Research, Section B: Beam Interactions with Materials and Atoms, 406, pp. 708–713, 2017.

[May03] S. G. Mayr, Y. Ashkenazy, K. Albe, R. S. Averback, "Mechanisms of Radiation-Induced Viscous Flow: Role of Point Defects", Physical Review Letters, 90(5), pp. 4, 2003.

[Meh07] H. Mehrer, "Diffusion in solids: fundamentals, methods, materials, diffusion-controlled processes", Springer series in solid-state sciences, 2007.

[Nas06] M. Nastasi, J. W. Mayer, "Ion Implantation and Synthesis of Materials", Springer, 2006.

[Njo14] E. G. Njoroge, "Solid-state interaction between Zr thin films and SiC", University of Pretoria, 2014.

[Nor05] K. Nordlund, Y. Ashkenazy, R. S. Averback, A.V. Granato, "Strings and interstitials in liquids, glasses and crystals", Europhysics Letters, 71(4), pp. 625–631, 2005.

[Ohr92] M. Ohring, "The materials science of thin films", Hoboken, New Jersey: Academic press, 1992.

[She89] P. Shewmon, "Diffusion in solids″, Warrendale, Pennsylvania: Minerals, Metals and Materials Society, 1989.

[Ste11] H. Stenlund, "Three Methods for Solution of Concentration Dependent Diffusion Coefficient", pp. 1–6, 2011.

[Wil00] S. D. Wilkinson, "Mass Transport in Solids and Fluids", University Press, Cambridge, 2000.

[Wil10] J. S. Williams, "Ion-Beam-Induced Amorphization and Epitaxial Crystallization of Silicon", Topics in applied physics; Materials science with ion beams, 116, pp. 73–111, 2010.

[Wil78] A. F. Willoughby, "Atomic diffusion in semiconductors", Reports on Progress in Physics, 41, pp. 1665, 1978.

[Www18] www.google.com, Flux, 2018.

CHAPTER 5

ANALYSIS TECHNIQUES

This chapter will discuss the analytical techniques used in this study. These were Rutherford backscattering spectrometry (RBS), Raman spectroscopy and scanning electron microscopy (SEM).

5.1 RUTHERFORD BACKSCATTERING SPECTROMETRY (RBS)

Rutherford backscattering was first used in 1913 to prove Rutherford's proposed model of the atom [Rut12]. Nuclear physicists again applied RBS after World War II. Using particle accelerators by this method they recognized contaminates in their samples. The backscattered ions from target atoms appeared as a "parasitic" effect in the nuclear reaction particle spectra [Tol49], [Gro84]. In 1968, Turkevich *et al*. [Tur68] used an alpha-scattering particle experiment to analyze the elemental composition of lunar soil samples. Rutherford backscattering analysis has capability to distinguish the elements atomic mass and their distribution in depth as a function of detected energy from backscattered particles. It represents a sensitive tool which is applied to study the solid surface compositions. It also provides quantitative determination and depth profiling of elements [Per87].

RBS is also a powerful non-destructive technique which is capable to providing its results in a short analysis time (about 15 minutes). RBS can also be used to determine depth profiles at the surface and interface [Kus92] and therefore can be applied to characterize the composition of thin film layers. It can also easily determine the depth distribution on implanted ions, especially if the ion mass is much larger than the substrate atomic mass [Lav08]. It is ideal for ion implantation experiments, diffusion studies and analysis of thin film layers with reasonable depth resolution, e.g. a few 100 Å [Chu78]. RBS is also capable of giving the depth profiles of minor and major constituents near the surface region of thin films as a function of detected energy [Jey97].

An advantage of using RBS is that it can quantitatively identify atoms present in a sample in a timely and accurate manner. However, the main disadvantage of RBS is its low sensitivity to the light elements such as hydrogen, oxygen and carbon in comparison to heavier elements such as silicon, etc. [Alo93]. RBS also has other disadvantages such as its inability to determine the chemical state of a compound. However, it can determine the absolute amounts of various elements in a sample independent of their chemical state (nature of the atomic bonds). The other disadvantage of RBS is the decrease of its depth and mass resolution when the mass of target atoms increases (i.e. for heavy elements such as Au, Pb, Hg). Also an ambiguity can exist for very close masses in some compounds (yttria-stabilized zirconia) [Per87].

5.1.1 PRINCIPLES OF OPERATION

RBS uses the bombardment of a target by mono-energetic positive ions. These positive ions are usually $^4He^+$ ions with energy ranging between 1 and 3 MeV. The collimated beam of energetic ions is focused on to a target which is in a high vacuum scattering chamber. The energy of the backscattered ions is measured from scattering events at the surface and a depth. The typical scattering angle, which is optimized for mass resolution, is in the range $160^o \leq \theta \leq 170^o$ [Chu73]. RBS technique is based on three principle factors; kinematic factor, scattering cross section and the depth profile [Ear94]. In next sections these three factors will be briefly discussed.

For channeling measurements, the target must be mounted on a goniometer to control the rotation and tilting [Mat85].

In this study energetic $^4He^+$ (1.6 MeV) with a backscattering angle of 165^o to a solid state detector (SSD) was applied and only the backscattered particles were detected. The RBS spectrum showed a backscattering yield as a function of channel number (energy distribution). The results and acquired spectra from RBS in this study will be discussed in Chapter 7.

5.1.2 RBS INSTRUMENTATION

Figure 5.1 shows an illustration of the Rutherford backscattering spectrometry instrument that is available at University of Pretoria. This set up consists of four main components; helium ions source, a Van de Graaff accelerator, scattering chamber and a detector. The accelerator is used to convert the low energy helium ions to high energy alpha particles and the detector (a surface barrier detector (SBD)) is used to detect the energetic backscattered ions. A RF (radio frequency) source generates positively charged He ions at energies of up to 100 keV. Afterwards, these charged particles are accelerated to high energies by applying a large potential difference across an accelerator tube. The potential difference is generated by a Van de Graaff accelerator [Gra31]. The Van de Graaff accelerator consists of an RF source, a high voltage generator and a continuous carrier belt which transports electrostatic charges. A Van de Graaff accelerator generally can produce a He ions beam with energies between a few hundred kilo-electron-volts and a few mega-electron-volts. The accelerator used at University of Pretoria can produce a beam with energy of up to 2.7 MeV, however in this study the maximum energy used was 1.6 MeV.

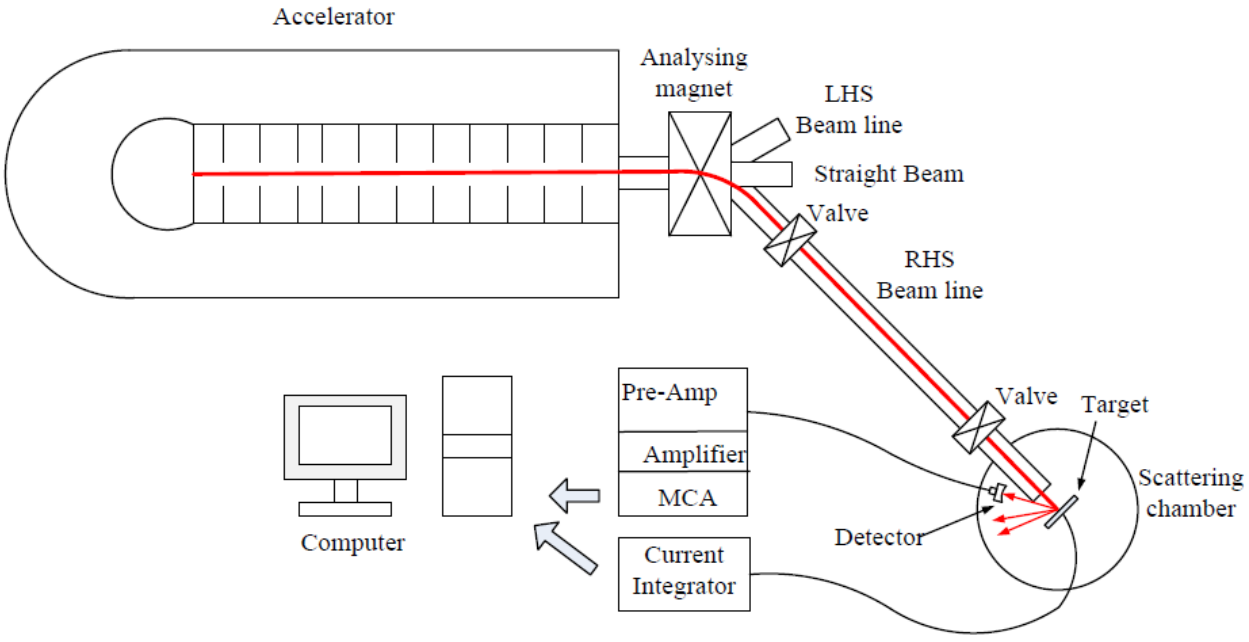

Fig. 5.1. Schematic of RBS set up at University of Pretoria. Adapted from [Njo14]

A high DC potential is kept by a continuous charge flowing to the ground via a voltage insulator of very high resistance. The generated positive ions by RF source, is accelerated through the accelerator tube and then extracted as ionized gas inside the terminal (a positive ion source). In this process, different ionic charge states (of helium) are produced by the accelerator which are then separated by a dipole magnet. The dipole magnet separates any He^- or He from the He^+ beam. The magnet deflects the beam to the right or left side of the straight beam line. Then the mass, energy and charge selected beam goes through a vacuum beam line and is focused on the target by magnetic slits. The scattering chamber contains a stage for mounting the sample. The scattering chamber is also connected to a three axis goniometer to control the tilting and rotating of the sample, a solid state detector, 1 mm diameter collimator (connecting the beam line) and a vacuum pump. The vacuum pump system includes a turbo pump and a fore pump. The fore pump system can produce a pressure in range of 10^{-3} mbar and the turbo pump decreases this pressure to the range of 10^{-7} mbar in the chamber, effectively creating a high vacuum environment. The backscattered projectile energy is detected by a solid state detector (SSD). The backscattered He ions from target form electron-hole pairs in the detector. These pairs are separated by a reverse bias of 40V electric field and create a charge pulse [Chu78]. The solid state detector is connected to an amplifier and the output signal is fed to an analogue to digital convertor. A multichannel analyzer recognizes the energy and the number of scattered He ions. The multichannel analyzer is connected to a computer. The data is displayed as counts versus channel number spectrum. Converting the signal height (which is proportional to energy) into 512 channels is carried out by multichannel analyzer, where energy range is from 0 to 1.6 MeV for our spectra. In each channel the recoiled He^+ ions having a specific limited energy range are collected and read. The RBS spectrum is shown as a yield of He particles as a function of their energy [Chu 96].

5.1.3 KINEMATIC FACTOR

When a moving mass (M_1) with initial energy of E_0 collides with a stationary mass (M_2), energy will be transferred from the moving particle to the stationary particle. Also the M_1 particle will be scattered at an angle of θ and energy E_1. Furthermore, the mass M_2 will move away with energy E_2 and at an angle of φ (see Figure 5.2) [Njo14]. In backscattering analysis it is considered that the M_1 is the projectile atom from a beam line and M_2 is the target atom. Assuming that this event is

an elastic collision between the two particles and by applying the principle of conservation of energy and momentum, the energy of the backscattered particles is given by [Chu78]:

$$E_1 = KE_0 \quad \rightarrow \quad 0 < K < 1 \tag{5.1}$$

where K is known as kinematic factor and is the ratio of the projectile energy before (E_0) and after (E_1) the scattering event. This factor is estimated as:

$$K = E_1/E_0 \quad \rightarrow \quad K = \left[\frac{M_1\cos\theta + \sqrt{M_2^2 - M_1^2\sin^2\theta}}{M_1 + M_2}\right]^2 \tag{5.2}$$

In general, the kinematic factor is used for calibration of the RBS spectrum. Using the kinematic factor and standard beam energy, the backscattered particle's energy can be estimated. This can also be applied to determine the mass of an unknown target atom from measured energy E_1 and consequently identifying the target atoms [Chu78]. Kinematic factor increases with the target mass and tends toward unity for heavy masses, thus the mass separation on the RBS energy spectrum decreases when the mass increases.

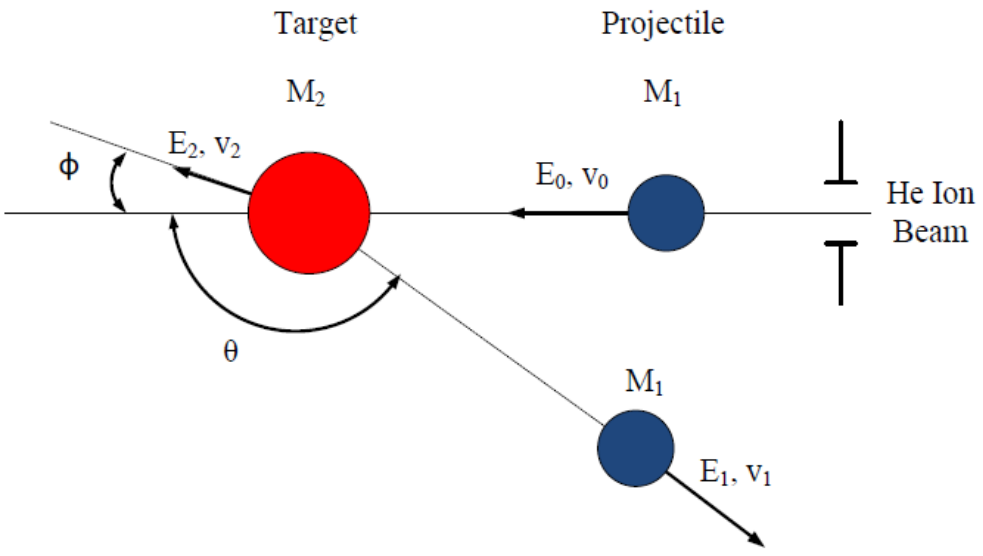

Fig. 5.2. A typical schematic of scattering between projectile and target atom. Adapted from [Njo14]

5.1.4 DEPTH PROFILING

The depth scale gives the relationship between the energy of backscattered particle (E_1) and the depth x of the incident ions inside the sample. In Figure 5.3, the particle incident energy is E_0, the energy immediately before scattering at a depth of x is E and the energy of exiting particle from the surface is E_1. The energy lost before the scattering of particles at depth of x (along the inward path; ΔE_{in}) is E_0-E while the energy loss along the outward path; ΔE_{out} is KE-E_1 [Chu78].

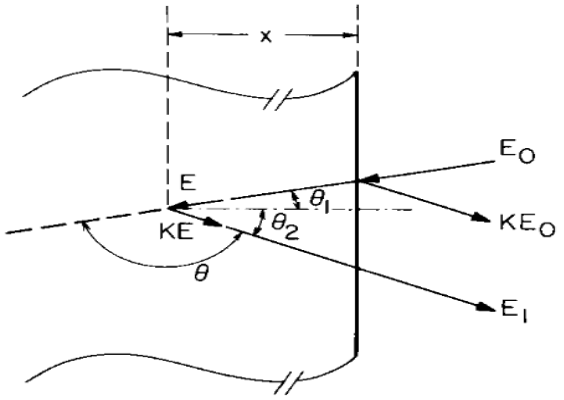

Fig. 5.3. A schematic diagram description of backscattering event in a sample consisting of a monoisotopic element. Obtained from [Chu78]

As discussed in Chapter 3 regarding energy loss, by assuming a constant value for dE/dx along the inward and outward paths, we can obtained the energies as below [Chu78]:

$$E = E_0 - \frac{x}{\cos\theta_1} \left.\frac{dE}{dx}\right|_{in} \tag{5.3}$$

$$E_1 = KE - \frac{x}{\cos\theta_2} \left.\frac{dE}{dx}\right|_{out} \tag{5.4}$$

where 'in' and 'out' refers to the (constant) dE/dx values along the inward and outward paths. By eliminating E from both equations we obtain:

$$KE_0 - E_1 = \left[\frac{K}{\cos\theta_1} \left.\frac{dE}{dx}\right|_{in} + \frac{1}{\cos\theta_2} \left.\frac{dE}{dx}\right|_{out}\right] x \tag{5.6}$$

KE_0 is the energy of the backscattered particles from the atoms in the target surface. Considering the backscattering energy loss factor, S, as:

$$S = \left[\frac{K}{\cos\theta_1}\frac{dE}{dx}\Big|_{in} + \frac{1}{\cos\theta_2}\frac{dE}{dx}\Big|_{out}\right] \quad (5.7)$$

The equation (5.6) can be written as a relationship between depth and backscattering energy loss factor as:

$$\Delta E = [S]x \quad (5.8)$$

where ΔE is the energy difference between E_1 and KE_0.

5.1.5 RBS CALIBRATION

The obtained RBS spectra were calibrated with the surface channels of elements such as Si, C, Ag and Pd. To obtain the surface energy values (KE_0), the surface channel numbers of these elements were obtained from the raw RBS spectra. Then by multiplying the incident beam energy (E_0) and the corresponding kinematic factor (K) of these elements, we estimated the surface energy values. The scattered He ions energy at the detector is a linear function of channel number represented by the equation below:

$$E = ax + b \quad (5.9)$$

where *a* is the energy conversion factor in keV/ch and b is the offset in keV. A typical energy calibration plot obtained in this study is shown in Figure 5.4.

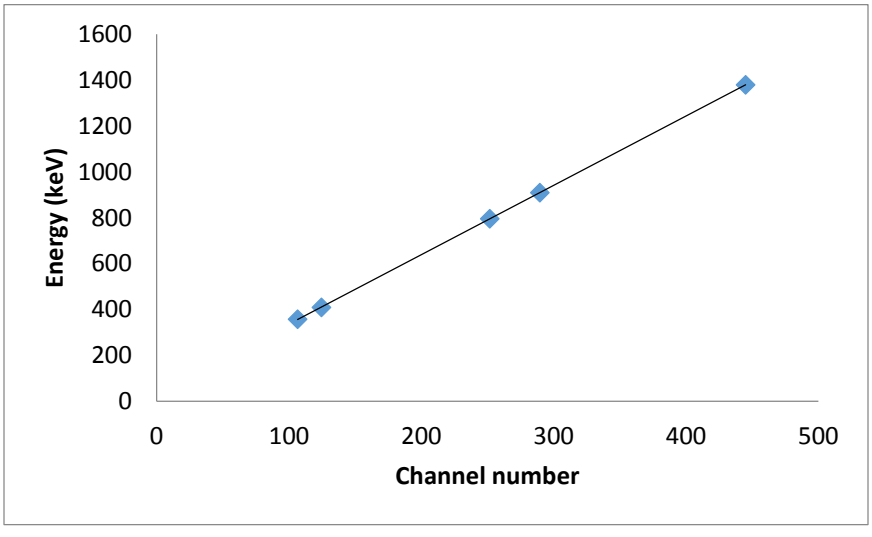

Fig. 5.4. RBS energy calibration graph

5.1.6 SCATTERING CROSS-SECTION

In general, only a small fraction of incoming particles from the incident ion beam are backscattered from target atoms to the detector. The exact fraction of backscattered particles from target atoms at an angle of θ (from the direct incident ion path) into the differential solid angle dΩ is given in terms of the differential scattering cross section (dσ/dΩ) (see Figure 5.5). If Q is the total number of projectiles which have hit the target and dQ is the number of particles recorded by the detector, then dσ/dΩ is expressed as [Chu78]:

$$d\sigma/d\Omega = \frac{1}{\rho_v t}\left[\frac{dQ/d\Omega}{Q}\right] \tag{5.10}$$

Where ρ_v is the volume density of atoms in the target and t is its thickness. Thus $\rho_v t$ is the number of target atom per unit area. The definition assumes that the solid angle dΩ is so small that the scattering angle θ is well defined. The solid angle Ω is about (10^{-2} sr or less), thus it is convenient to introduce the average scattering cross section as:

$$\sigma = 1/\Omega \int \left(\frac{d\sigma}{d\Omega}\right) d\Omega \tag{5.11}$$

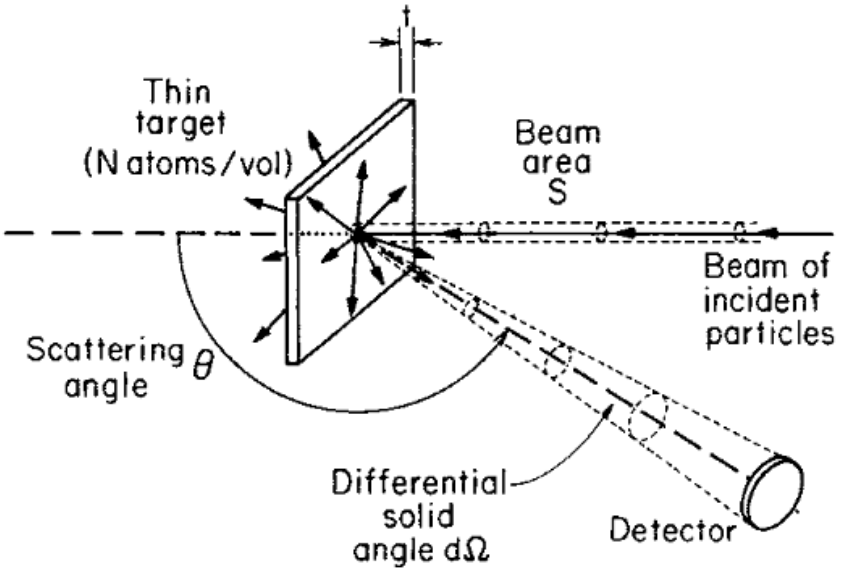

Fig. 5.5. A layout of a laboratory set up to explain the concept of differential scattering cross section with differential solid angle dΩ. Taken from [Chu78]

In the laboratory reference frame [Gro84], the differential scattering cross section is given by:

$$\frac{d\sigma}{d\Omega} = \left[\frac{Z_1 Z_2 e^2}{4E_0}\right]^2 \frac{4}{\sin^4\theta} \frac{\left[\cos\theta + \sqrt{1-(\frac{M_1}{M_2}\sin\theta)^2}\right]^2}{\sqrt{1-(\frac{M_1}{M_2}\sin\theta)^2}} \quad (5.12)$$

where Z_1 and Z_2 are the atomic numbers and M_1 and M_2 are the masses of projectile and target atoms, respectively. The scattering cross section (σ) is usually used in RBS measurements to determine the average value of dσ/dΩ over the dΩ (solid angle) determined by the detector.

5.2 RAMAN SPECTROSCOPY

Raman spectroscopy involves illuminating a sample with monochromatic light and using a spectrometer to examine the scattered light by the sample. It was first discovered by Dr. C. V. Raman in 1928. He used sunlight as the source, a telescope as the collector and his eyes as the detector. He discovered that sunlight is scattered inelastically and produces layout for different materials. This inelastic light scattering was named Raman Effect.

Raman spectroscopy is used to observe the vibrational, rotational and other low frequency modes in a sample. Due to specific vibrational frequencies and symmetry for any type of chemical bonds of a molecule, Raman spectroscopy provides a structure fingerprint by which molecules can be identified. It is also used as the surface analysis technique which helps to study chemical bonding and intermolecular bonds. In solid state physics, Raman spectroscopy is used to characterize materials and find the crystallographic orientation of a sample [Gar89].

At the molecular scale photons interact with samples either by scattering or absorption. The incident light interacts with the atom or molecule and distorts its electronic shell forming a "virtual state". Due to instability of this state, the photon is re-emitted as scattered light while the stimulated electrons return to their stable states. Scattering occurs elastically and inelastically. In elastic scattering, the scattered photons have the same frequency and wavelength as the incident photons. The elastic scattering is called Rayleigh scattering while the inelastic scattering is termed Raman Effect (see Figure 5.6). In inelastic scattering, the scattered light does not have the same frequency as the incident light. Raman scattering phenomenon happens when the sample exchanges energy with photons. Subsequently, the system falls to levels of vibrational energy which is above or

below the initial state. The shifted frequency is caused by energy difference between scattered and incident photons which is called Raman shift. The Raman shifts provide information about vibrational, rotational and electronic energy of a molecule or crystal [Sha10].

The upward or downward shift of the scattered photon relative to that of the incident photon (the Raman shift) depends on whether the system has gained or lost energy. The up-shifted and down-shifted components are termed *anti-Stokes* and *Stokes* lines, respectively (Figure 5.6). Raman spectrum contains a plot of detected number of photons versus the Raman shift (from the incident laser energy). Raman spectroscopy is a useful technique for identifying chemicals, because different chemicals have different vibrational modes and, consequently, different characteristic Raman spectra.

Figure 5.6 shows that in Rayleigh (elastic) scattering there is no exchange of energy. In this process an electron in ground state is momentarily excited to a higher energy state before returning to its initial state. In this phenomenon both the incident and scattered light have the same wavelength. Similarly, in Stokes (inelastic) Raman scattering, the electron is excited from the ground state by absorbing the energy of the incident photon, however, after the emission process, falls to a vibrational state instead of its ground state. In this case the scattered light has less energy and, thus, a longer wavelength than the incident light. Contrary to Stokes scattering, in anti-Stokes (inelastic) Raman scattering, an already excited electron in a vibrational level, absorbs the energy of the incident photon but subsequently falls back to its ground state (most energetically stable compared to its initial state) by emitting a scattered photon. In this process, the scattered light is more energetic than the incident light (higher frequency and shorter wavelength) [www16].

In general, Raman spectroscopy is non-destructive; however it can be destructive depending on the output power of the laser. Focusing a laser beam on a small point for long durations can burn, alter or anneal the sample [Wer97].

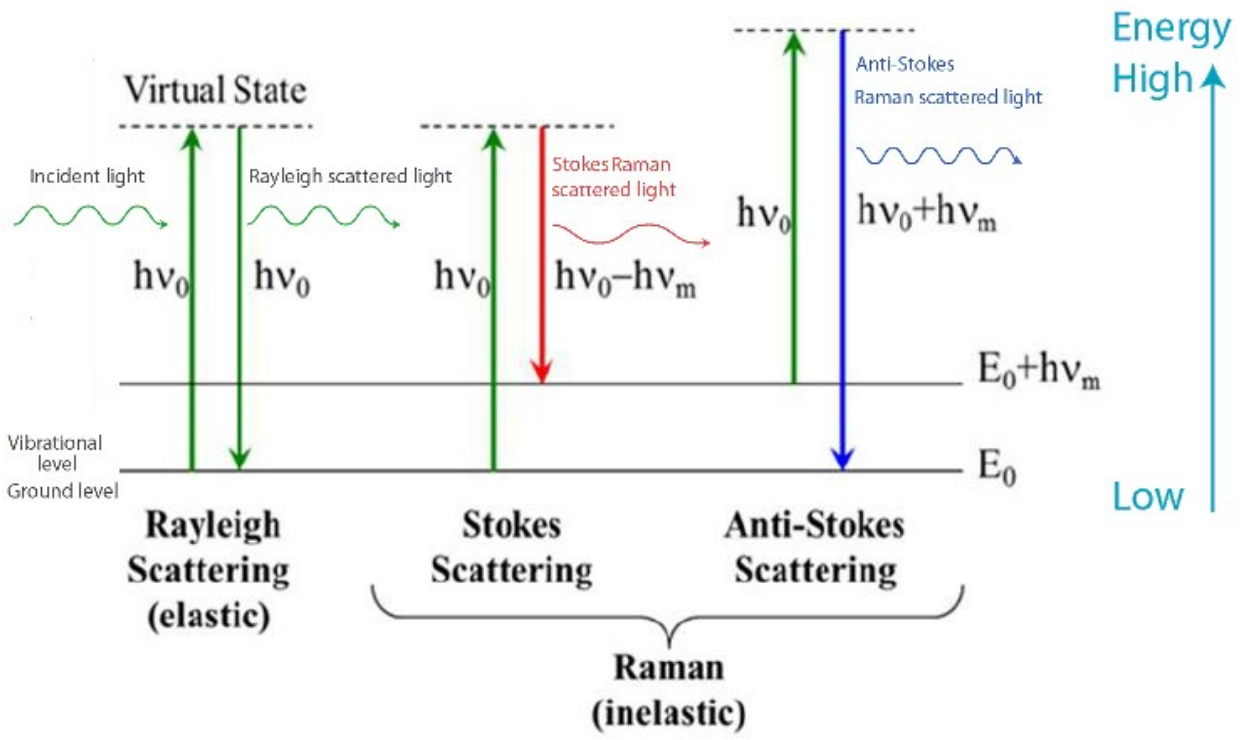

Fig. 5.6. A diagram showing energy transitions for Rayleigh and Raman scattering. Taken from [Htt18]

5.2.1 RAMAN SPECTROSCOPY APPLICATIONS AND ADVANTAGES

Raman spectroscopy has been recognized as a versatile technique and as an important analysis tool for numerous applications. Because of its potentially non-destructive nature and high sensitivity, Raman is applied in many fields such as biology, physics, chemistry, geology, material science and etc. [Nic08]. Because of the sensitivity of Raman spectroscopy to structural changes, it is a powerful technique to monitor the microstructure changes in materials and also in carbon based materials [Kni88]. The main advantage of Raman spectroscopy is its ability to distinguish between different chemical states of a particular compound.

For example, Raman spectroscopy has been used for understanding the microstructure changes in diamond and graphite after ion irradiation [Dre92], to investigate the effect of graphitization in both graphitizing and non-graphitizing carbon materials [Les84], to show the sp^2 and sp^3 content in DLC materials [Fer00], for the characterization of the graphite surface [Tui70], studying

amorphous carbons [Wad80], [Rou83], [Wag89] and glassy carbon (nano-graphite ribbons) [Can04].

Raman spectroscopy also offers some advantages such as [Nic08]:

- Minimal or no sample preparations
- Non-destructive analysis, i.e. the sample can be used for other analyses
- Analysis not affected by atmospheric particles such as CO_2 or H_2O
- Non-intrusive (no damage) analysis

5.2.2 RAMAN INSTRUMENT

The main Raman scattering components are an excitation source (usually a laser), a dispersive spectrometer and a charged couple device (CCD) for detection, see Figure 5.7. The most common choice is visible laser excitation. The radiation is arranged to hit the notch filter. The notch filter is a band stop (or rejection) filter with narrow stop band. It is a type of frequency selective circuit which works in exactly opposite way of band pass filter. The notch filter is common used as a filter which passes most frequencies unaltered but, attenuates those in a specific range to very low levels (compared with cut-off frequencies). The cut-off frequency for a low-pass filter is that frequency at which the output (load) voltage equals 70.7% of the input (source) voltage. Above the cutoff frequency, the output voltage is lower than 70.7% of the input, and vice versa. The notch filters are used as interference filters which work when the beam is perpendicular to the plane of the filter. The notch filter is also used to reduce the Raman spectrometers size and improve their efficiency. Furthermore, the notch filter collects the scattered light. For the angles shown in the diagram (Figure 5.7) the laser radiation contacts the filter so that the light is completely reflected into the microscope. When the scattered radiation is collected back through the same optics from the microscope, the beam is incoming into the filter at an ideal angle for transmission of scattered radiation. Finally this light is passed through a monochromator and onto the CCD detector.

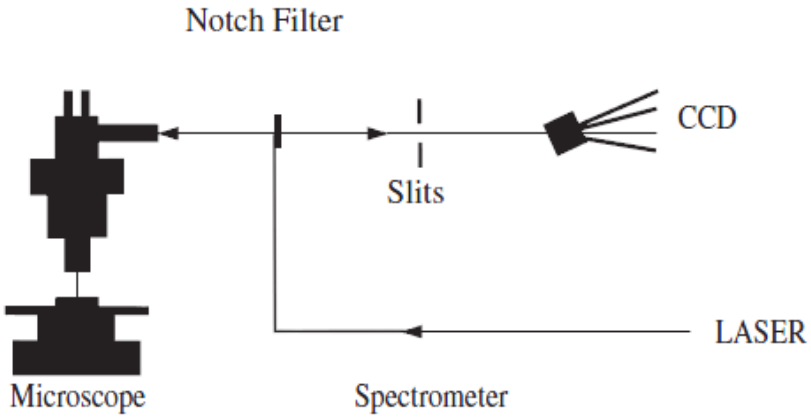

Fig. 5.7. Raman spectrometer and microscope, using visible laser, notch filter, spectrometer and CCD detector. Obtained from [Smi05]

Improving the Raman sensitivity is possible by applying the highest possible frequency. This means the working region would be in UV (ultra violet) region. The other advantage of UV excitation is that there is less fluorescence compared to visible excitation. But the disadvantage of using UV Raman is that many compounds absorb UV radiation. This and the high energy of UV photons means there is a high risk of sample degradation through heat damage or photo-induced chemical reactions on the exposed surface. It also means that due to resonance with any electronic transition which causes adsorption, the Raman spectra may be different from normal Raman spectra. The main disadvantage of using visible excitation is fluorescence. This is a much bigger problem in visible region than in UV region [Smi05].

5.2.3 RAMAN SPECTROSCOPY THEORY

As discussed in the previous section, in Rayleigh (elastic) scattering the rotational and vibrational energy of the molecule is unchanged. But in inelastic Raman scattering the molecule's vibrational and rotational energy is changed. This change of energy is expressed as the difference between the energy of incident photon and the energy of backscattered photon, ΔE_m, and given by:

$$\Delta E_m = h\nu_i - h\nu_s \qquad (5.13)$$

where h is Plank's constant, ν_i is the frequency of the incident photon ($h\nu_i$ is the incident photon energy) and ν_s is the frequency of the scattered photon ($h\nu_s$ is the scattered photon energy). If the molecule gains energy, then $\Delta E_m > 0$ and $\nu_s < \nu_i$ (Stoke lines in Raman spectrum). By contrast, if the molecule loses energy, then $\Delta E_m < 0$ and $\nu_s > \nu_i$ (anti-Stoke lines in Raman spectrum) [Col75]. At room temperature most molecules are in the ground vibrational state. Therefore Stokes lines have greater intensities than anti-Stokes lines that originated from an excited level with a lower population. The ratio of the intensities of the Stokes and anti-Stokes Raman scattering depends on the number of molecules in excited and ground vibrational levels. From the Boltzmann equation this ratio is given by [Smi05]:

$$\frac{N_n}{N_m} = \frac{g_n}{g_m} \exp\left[\frac{-(E_n - E_m)}{k_B T}\right] \tag{5.14}$$

where N_n is the number of molecules in the excited vibrational energy state (n), N_m is the number of molecules in the ground vibrational energy state (m), g is the degeneracies of the n and m states, and E_n-E_m is the energy difference between the vibrational energy states and k_B is the Boltzmann constant.

When a molecule is exposed to the electric field of electromagnetic radiation, its protons and electrons will experience forces in opposite directions. As a result, the nucleus is displaced relative to the electrons and the polarized molecule has an induced dipole moment caused by the external field. The relation between the electric field, E, and induced dipole moment, μ, is given by [Col75]:

$$\mu = \alpha E \tag{5.15}$$

where α is the polarizability. The electric field (E) of the electromagnetic radiation in the neighborhood of the molecules is given by:

$$E = E_0 \sin 2\pi\nu t \tag{5.16}$$

where E_0 is a constant (the maximum value of the field), ν is the frequency and t is time. By combining equations (5.15) and (5.16) we achieved:

$$\mu = \alpha E_0 \sin 2\pi\nu t \tag{5.17}$$

The polarizability (α) of molecules is not constant and changes with certain rotations and vibrations. For small displacements, the polarizability can be expanded into a Taylor series as:

$$\alpha = \alpha_0 + \frac{\partial \alpha}{\partial Q} Q + \cdots \quad (5.18)$$

where α_0 is the equilibrium polarizability and $\frac{\partial \alpha}{\partial Q}$ is the rate of change of polarizability with respect to Q measured at the equilibrium configuration. In the harmonic approximation, the higher order terms of equation (5.18) are neglected. The displacement (Q) of the molecule around its equilibrium position due to vibrational mode is given by:

$$Q = Q_0 \sin 2\pi\nu_v t \quad (5.19)$$

where ν_v is the vibration frequency of Q and Q_0 and is a constant (the maximum value for Q). Combining equations (5.18) and (5.19), gives:

$$\alpha = \alpha_0 + \frac{\partial \alpha}{\partial Q} Q_0 \sin 2\pi\nu_v t \quad (5.20)$$

Substitution of this value for α into equation (5.17) yields:

$$\mu = \alpha_0 E_0 \sin 2\pi\nu t + \frac{\partial \alpha}{\partial Q} Q_0 E_0 (\sin 2\pi\nu_v t)(\sin 2\pi\nu t) \quad (5.21)$$

Making use of a trigonometric identity, it is written as:

$$\mu = \alpha_0 E_0 \sin 2\pi\nu t + \frac{\partial \alpha}{\partial Q} \frac{Q_0 E_0}{2} (\cos 2\pi(\nu - \nu_v)t - \cos 2\pi(\nu + \nu_v)t \quad (5.22)$$

From this equation it can be seen that the dipole moment μ changes with ν_v, $\nu - \nu_v$ and $\nu + \nu_v$. These three frequencies are important in Raman scattering and are attributed to Rayleigh scattering, Stokes and anti-Stokes Raman scattering, respectively [Col75].

5.2.4 SOME CARBON MATERIALS RAMAN SPECTRA

Raman spectroscopy is highly sensitive to a slight microstructural changes, internal stress and bonds present in carbon materials. It is widely applied to the study of all carbon based materials [Fer00]. As an example, the Raman spectrum of natural diamond consists of a zone center mode (T_{2g}) at 1332 cm^{-1} [Kni88], and is shown in Figure 5.8. This figure shows the first order peak which is well fitted by a Lorentzian function. The full width at half maximum (FWHM) is typically ≤ 2 cm^{-1} [www18a].

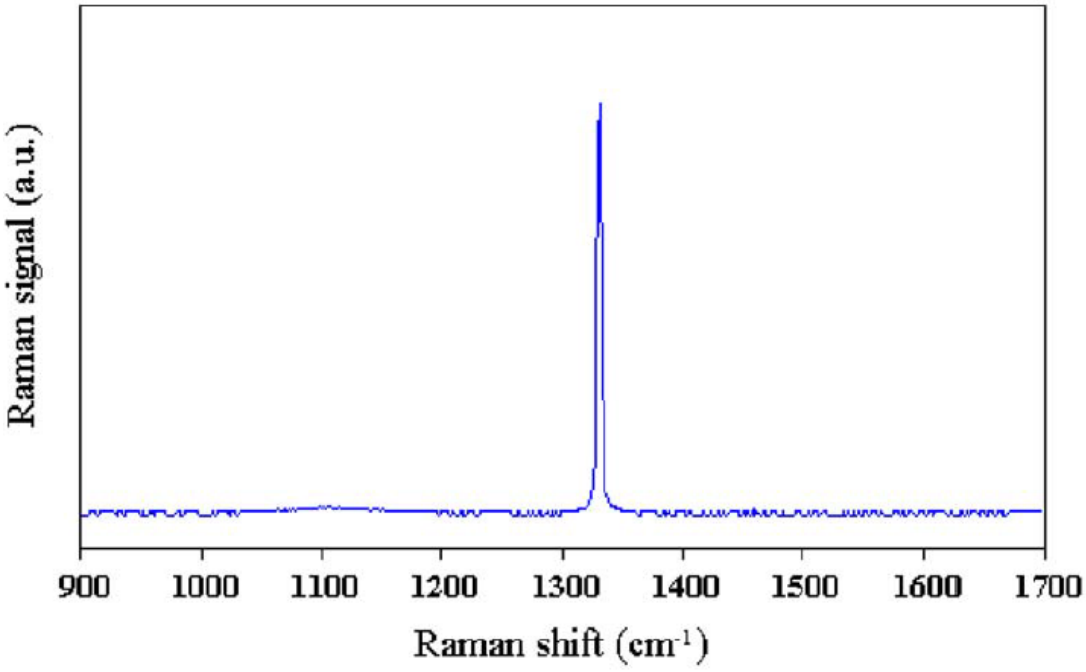

Fig. 5.8. Raman spectrum of natural diamond, showing the reference band and absence of other background features. Taken from [www18a]

Figure 5.9 shows the Raman line at 1575 cm^{-1} which is present in all graphite samples. However, a slight frequency shift of 15 cm^{-1} toward higher wavenumber was found in some studies with extremely small crystal sizes. The observed Raman band in single crystals of graphite is attributed to the symmetry E_{2g} mode (so called G peak) [Tui70].

Figure 5.10 shows the Raman spectra of various non-crystalline, mainly graphitic carbons. The pair of the D peak (attributed to the breathing mode, A_{1g}) and the G peak are seen in this figure. However, there are small shifts in the wavenumber of these bands [Dil84].

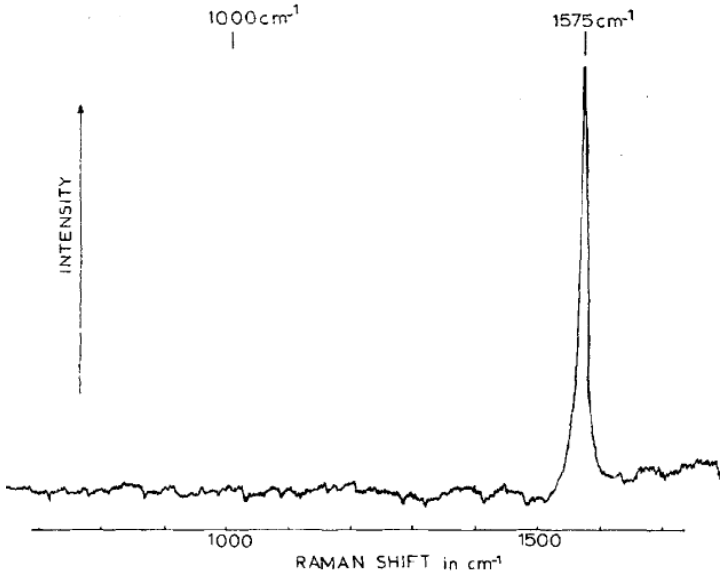

Fig. 5.9. Raman spectrum of single crystal graphite. Obtained from [Tui70]

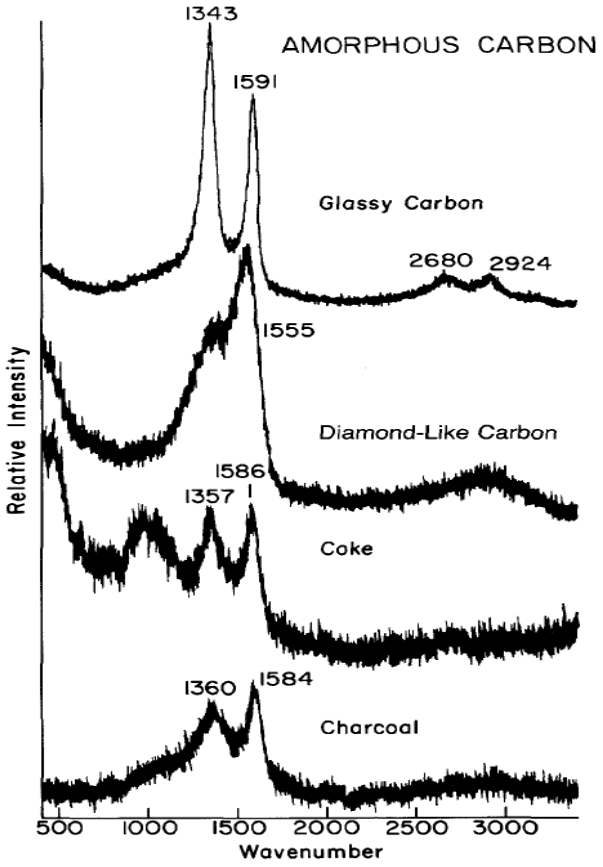

Fig. 5.10. Raman spectra of some amorphous carbon. Taken from [Kni88]

5.3 SCANNING ELECTRON MICROSCOPY (SEM)

Electron microscopy is specified as a specialized field of instrumentation which applies the electron microscope as a tool. Ernest Ruska and Max Knoll developed the first electron microscope about 40 years ago. Ruska's efforts were recognized in 1986 with a Noble Prize in Physics. The scanning electron microscope (SEM) produces an image that gives the impression of three dimensions. This type of microscope operates by focusing a beam of electrons into a 2 or 3 nm wide spot that scans the surface of the sample. This results in the generation of secondary electrons that are emitted from the sample and are subsequently detected by a sensor. It is one of the main techniques available for the analysis and examination of the materials morphology [Boz99]. A typical SEM instrument consists of an electron gun, electromagnetic lenses, scanning system and detectors, all housed within an ultra-high vacuum chamber as well as a TV scanner, see Figure 5.11.

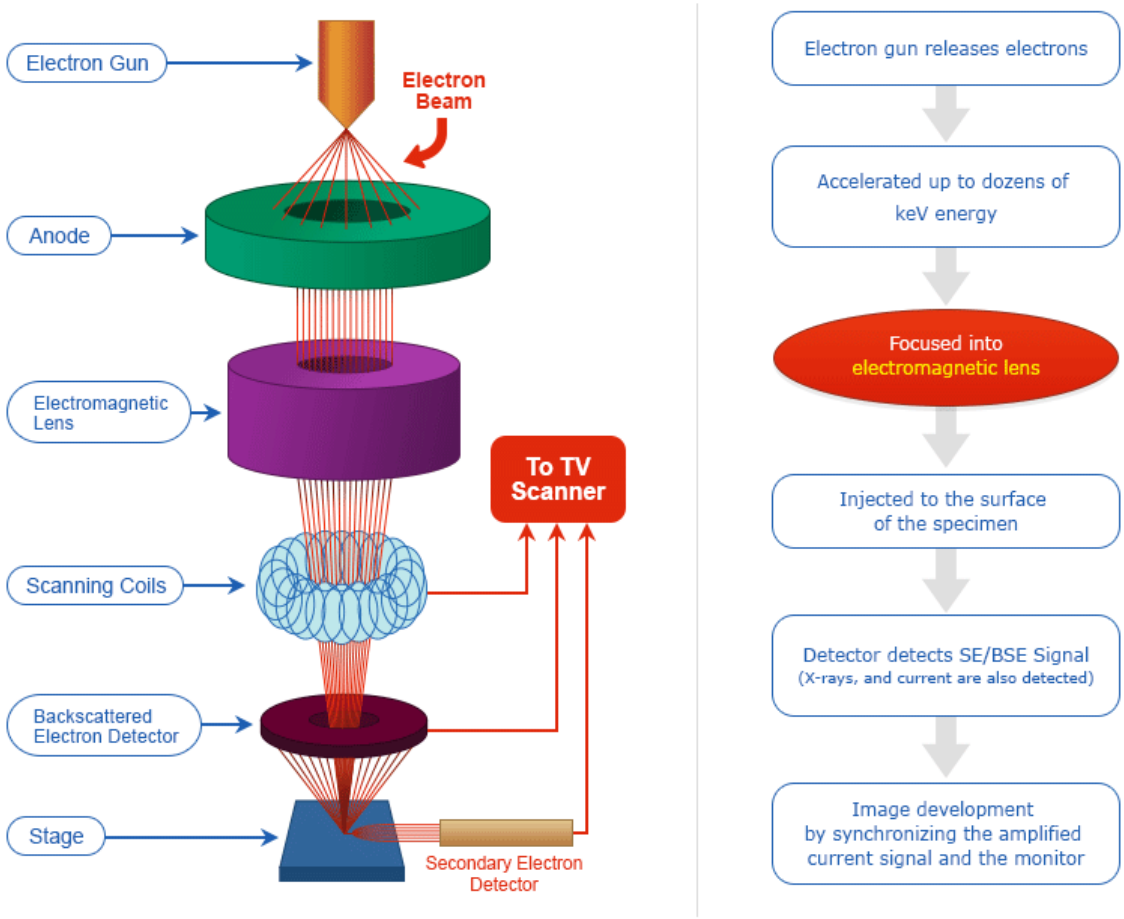

Fig. 5.11. A schematic diagram of the internal components of an SEM. Adapted from [www18b]

In a SEM setup the electron gun produces a beam of primary electrons. The electron gun often consists of a thin tungsten, LaB_6 or CeB_6 wire as a cathode filament which is typically located above the sample chamber. Field emission cathodes provide a relatively high current electron probe which has a high brightness, a low energy spread and a small virtual source diameter, especially at low accelerating voltage. The accelerated electrons can move from beam source to the sample and subsequently detector. Electromagnetic lenses and the scanning coils focus and direct the electron beam. They make a concentrated, small electron probe on the surface of the sample with the spot size of the beam less than 10 nm in diameter. The electron beam interaction depth is estimated to be typically 1 μm. However, this depth value depends on the sample characteristics and energy of the primary electrons [Pos94], [Ege05].

The formation of the SEM image depends on the acquisition of signals produced from the detection of the secondary electrons that are produced from interactions of the electron beam with the specimen. Backscattered electrons occur due to elastic collisions of electrons with target atoms. The elastic collision is usually defined by negligible energy loss during the collision. The scattering cross-section for backscattering is higher for heavy elements (higher atomic numbers) compared to the light elements (low atomic numbers). Therefore, heavy elements appear brighter in the backscattered SEM images. Thus backscattered SEM is used to detect contrast between areas with different chemical composition.

In this study, because europium was implanted uniformly over and into the glassy carbon surface, there is not any area with a different composition on the sample surface. Thus, backscattered electron microscopy is not very useful to apply for the investigation of implanted europium in glassy carbon.

Inelastic interactions happen through a variety of interactions between the incident electrons and sample atoms and electrons. There are a number of signals are produced when an electron beam strikes a sample, including the secondary electrons (SEs), the emission of characteristic X-rays, Auger electrons, see Figure 5.12.

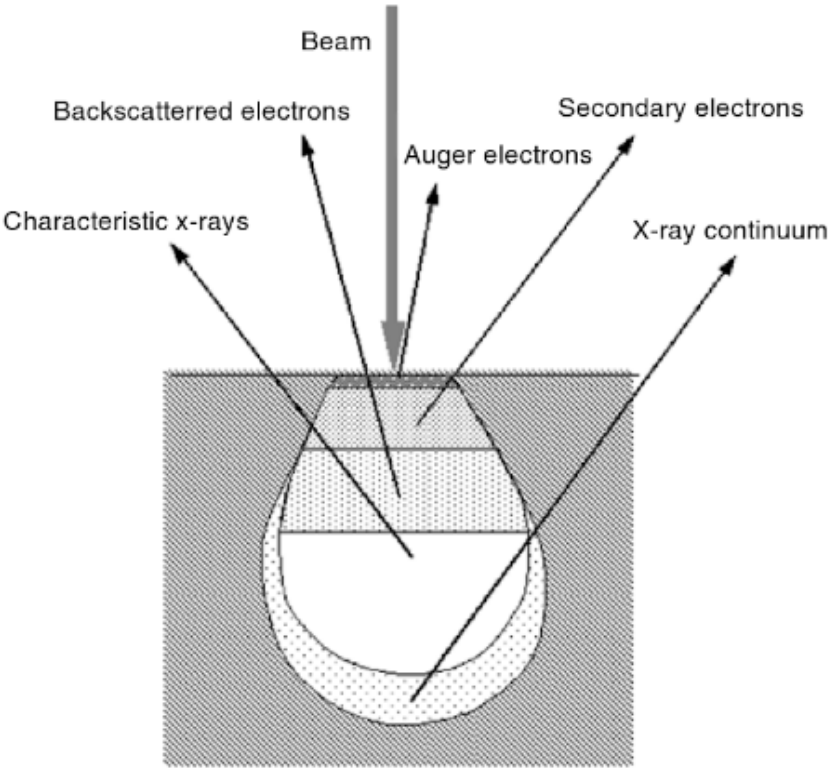

Fig. 5.12. An illustration of several generated signals by the electron beam with sample interaction regions in SEM and the areas from where the signals can be detected. Taken from [Zho06]

- Secondary electrons; the secondary electron emission signal is a widely used signal which is produced by the interaction of electron beam with the sample. Secondary electrons are generated when the incident electrons transfer all or part of their energy to the electrons in the specimen, resulting in their separation from the influence of their nuclei (ionization). These free electrons can have energy values of up to 50 eV and are the electrons that are detected by the detector.
- Auger electrons; Auger electrons are produced following the ionization of an atom by the incident electron beam causing an electron from the outer shell to fill a vacancy in the inner shell. The released energy by this process may be transferred to a third electron, i.e. the Auger electron. Due to the characteristic energy of this electron, it is used to provide the chemical information of the surface. Auger electrons are only emitted near the surface because of their low energies.

- Characteristic X-rays; another class of produced signals by the interaction of the initial electron beam with the sample. The provided chemical information by characteristic x-rays is the most widely used micro-analytical technique in SEM. When an electron in the inner shell is displaced by a collision with a primary electron, an electron in outer shell may fall into the inner shell. If the vacancy due to the creation of the secondary electron is filled from a higher orbital, an x-ray characteristic of that energy transmission is produced [Zho06].

5.3.1 IN-LENS DETECTOR

The in-lens detector is placed above the objective lens above the sample. It is capable of detecting the scattered electrons from the surface which are directly in the beam path. The In-lens detector can be complimentary to the main secondary electron detector to form a SEM image [Ege05]. Images from the in-lens detector are more sensitive to the scattering electrons (SEs) with lower energies. The in-lens image is mainly composed of electrons having energies less than 40 eV. These electrons are readily attracted by generated electrostatic field generated by boosting voltage (U_B in Figure 5.13). This can be the reason why in-lens detector images have high surface sensitivity [Izq10].

In-lens detector is used to map the actual surface of the sample through the detection of the first group of scattered electrons (SE1). The SE1 are the electrons which leave the surface of the sample directly at the spot where the electron beam is focused on, see Figure 5.13. Because the SE1 electrons originate from the surface or near-surface region, they contain only information directly related to the surface of the target. Furthermore, since SE1 electrons are generated directly below the beam path; they are more efficiently detected by the in-lens detector [www18c].

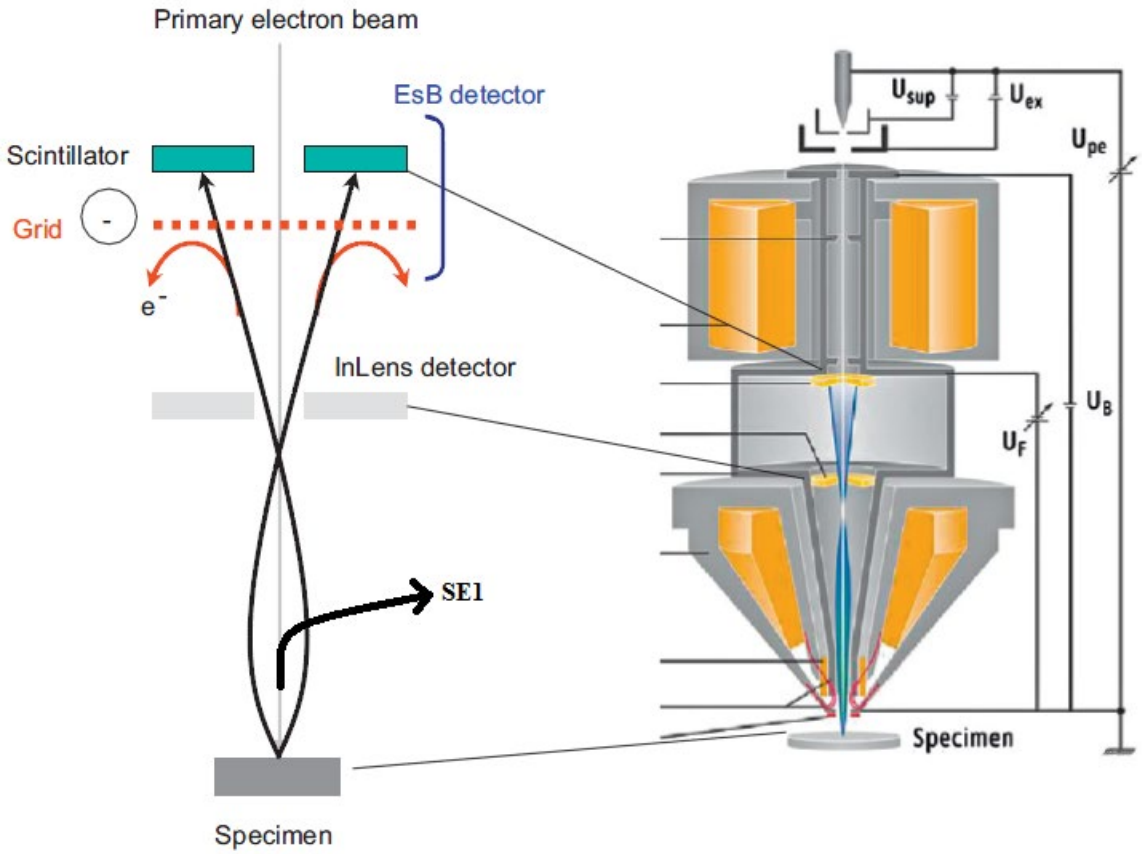

Fig. 5.13. A schematic diagram of in-lens detector. Obtained from [Nag13]

REFERENCES

[Alo93] P. Aloupogiannis, A. Travlos, "Rare-earth silicide thin film study. Comparison of heavy ion and conventional RBS", Vacuum, 44(1), pp. 37–39, 1993.

[Boz99] J. J. Bozzola, L. D. Russell, "Electron Microscopy: Principles and Techniques for Biologists". Second Edi. Jones and Bartlett Publishers,Inc., 1999.

[Can04] L. G. Cançado, M. A. Pimenta, B. R. A. Neves, G. Medeiros-Ribeiro, Toshiaki Enoki, "Anisotropy of the Raman spectra of nanographite ribbons", Physical Review Letters, 93(4), pp. 047403-1, 2004.

[Chu73] W. K. Chu, J. W. Mayer, M. A. Nicolet, "Principles and applications of ion beam techniques for the analysis of solids and thin films", Thin Solid Films, 17, pp. 1–41, 1973.

[Chu96] W. K. Chu, J. R. Liu, "Rutherford backscattering spectrometry: Reminiscences and progresses", Materials Chemistry and Physics, 46(2–3), pp. 183–188, 1996.

[Chu78] W. K. Chu, J. W. Mayer, M. A. Nicolet, "Backscattering Spectroscopy", Journal of Vacuum Science and Technology, 1978.

[Col75] B. N. Colthup, L. H. Daly, S. E. Wiberley, "Introduction to Infrared and Raman Spectroscopy". Academic press, 1975.

[Dil84] R. O. Dillon, J. A.Woollam, V. Katkanant, "Use of Raman scattering to investigate disorder and crystallite formation in as-deposited and annealed carbon films", Physical Review B, 29(6), 1984.

[Dre92] M. S. Dresselhaus, R. Kalish, "Ion Implantation in Diamond, Graphite and Related Materials", Springer-Verlag, 1992.

[Ear94] L. G. Earwaker, "Rutherford backscattering and nuclear reaction analysis", Vacuum, 45(6–7), pp. 783–803, 1994.

[Ege05] R. F. Egerton, "Physical Principles of Electron Microscopy-An Introduction to TEM, SEM and AFM", Springer Science & business media, 2005.

[Fer00] A. C. Ferrari, J. Robertson, "Interpretation of Raman spectra of disordered and amorphous

carbon", Physical Review B, 61, 2000.

[Gar89] D. J. Gardiner, P. R.Graves, H. J. Bowley, "Practical Raman spectroscopy", Springer-Verlag, 1989.

[Gra31] R. J. Van De Graaff, "A 15000000 Volt electrostatic generator", Physics Review, 1931.

[Gro84] J. J. Grob, P. Siffert, "Rutherford Backscattering Spectroscopy (RBS)", Progress in crystal growth and characterization, (1–2), pp. 59–106, 1984.

[Htt18] Http//:bwtek.com, "Theory of Raman Scattering", 2018.

[Iza10] G. A. Izquierdo, "New features observed with SEM in-lens detector in the vicinity of breakdown crater", 2010.

[Jey97] C. Jeynes, Z. H. Jafri, R. P. Webb, A. C. Kimber, M. J. Ashwin, "Accurate RBS measurements of the Indium content of InGaAs thin films", Surface and Interface Analysis, 25, pp. 254–260, 1997.

[Kni88] D. S. Knight, W. B. White, "Characterization of diamond films by Raman spectroscopy", Materials Research Laboratory, 1988.

[Kus92] K. Kusao, M. Satoh, K. Morita, "An area ratio method for RBS compositional analysis of thin films", Surface and interface analysis, 18, pp. 417–420, 1992.

[Lav08] V. Lavrentiev, J. Vacik, H. Naramoto, "Structural phenomena in glassy carbon induced by cobalt ion implantation", Applied Physics A: Materials Science and Processing, 92(3), pp. 673–680, 2008.

[Les84] P. Lespade, A. Merchant, M. Couzi, F.Cruege, "Characterization of carbon materials by Raman microspectrometry", Carbon, 22(4–5), pp. 375–385, 1984.

[Mat85] H. Matzke, "Application of ion beam techniques to solid state physics and technology of nuclear materials", Journal of Nuclear Materials, 136(2–3), pp. 143–153, 1985.

[Nag13] M. Nagoshi, T. Aoyama, K. Sato, "Ultramicroscopy Extraction of topographic and material contrasts on surfaces from SEM images obtained by energy filtering detection with low-energy primary electrons", Ultramicroscopy, Elsevier, 124, pp. 20–25, 2013.

[Nic08] C. Z. Nicolet, "Introduction to Raman spectroscopy", Thermo Fisher Scientific, 2008.

[Njo14] E. G. Njoroge, "Solide-state interaction between Zr thin films and SiC", University of Pretoria, 2014.

[Per87] J. Perriere, "Rutherford backscattering spectrometry", Vacuum, 37(5/6), pp. 429–432, 1987.

[Pos94] M. T. Postek, "Critical Issues in Scanning Electron Microscope Metrology", Journal of Research of the National Institute of Standards and Technology, 99(5), 1994.

[Rou83] J. N. Rouzaud, A. Oberlin, C. Beny-Bassez, "Carbon films: Structure and microtexture (optical and electron microscopy, Raman spectroscopy)", Thin Solid Films, 105(1), pp. 75–96, 1983.

[Rut12] E. Rutherford, "The scattering of α and β particles by matter and the structure of the atom", Philosophical Magazine, 92(4), pp. 379–398, 2012.

[Sha10] M. Sharon, "Carbon Nano Forms and Applications", McGraw-Hill Publisher, 2010.

[Smi05] E. Smith, G. Dent, "Modern Raman Spectroscopy-A Practical Approach, Journal of the American College of Surgeons", John Wiley & sons, Ltd., 2005.

[Tol49] A. V. Tollestrup, W. A. Fowler, C. C. Lauritsen, "Energy release in beryllium and lithium reactions with protons", California Institute of Technology, (1), pp. 4–6, 1949.

[Tui70] F. Tuinstra, J. L. Koenig, "Raman spectrum of graphite", Journal of chemical physics, 53(3), 1970.

[Tur68] A. L. Turkevich, J. H. Patterson, E. J. Franzgrot, "The chemical analysis of the lunar surface",56(4), pp. 312–343, 1968.

[Wad80] N. Wada, P. J. Gaczl, S. A. Solin, "Diamond-like 3-fold coordinated amorphous carbon", Journal of Non-Crystalline Solids, 35, pp. 543–548, 1980.

[Wag89] J. Wagner, M. Ramsteiner, Ch. Wild, P. Koidl, "Resonant Raman scattering of amorphous carbon and polycrystalline diamond films", Physical Review B, 40(3), pp. 1817–1824, 1989.

[Wer97] T. Werninghaus, "Micro-Raman Spectroskopy Investigation of Hard Coatings", the Faculty of Natural Sciences of the German University of Chemnitz-Zwickau, 1997.

[Www16] www.nanophoton.net, "Raman spectroscopy", 2016.

[Www18a] www.chm.bris.ac.uk, "Film Characterisation Techniques", 2018.

[Www18b] www.nanoimages.com, "SEM Technology Overview: Scanning Electron Microscopy, 2018.

[Www18c] www.iitk.ac.in, "Image Formation and Interpretation SEM Imaging Process", Indian Institute of Technology, Kanpur, 2018.

[Zho06] W. Zhou, Z. L. Wang, "Scanning Microscopy for Nanotechnology: Techniques and Applications", Springer Science & Business Media, 2006.

CHAPTER 6

EXPERIMENTAL PROCEDURES

The 50 mm x 10 mm Sigradur® G glassy carbon samples with 2 mm of thickness were implanted by europium (a fission product element). The preparation of sample, annealing of radiation damage, diffusion behavior, structural changes and surface modification were investigated by RBS, Raman spectroscopy and SEM. This chapter will discuss the experimental procedures details.

6.1 SAMPLE PREPARATION

The glassy carbon samples used in this study was provided by Hochtemperature-Werkstoffe (HTW), Germany. The samples were polished mechanically by a polisher, an ATM Saphir 500, before being polished by a diamond solutions of 1 and 0.25 μm respectively. Next, the samples were placed in an ultrasonic bath and cleaned in an alkaline soap solution. The samples were then transferred into a beaker container including de-ionized water to remove the soap solution. This procedure was done twice and each time for ten minutes. Next, to remove the de-ionized water from the samples, methanol was used for 5 minutes. The samples were then dried by blowing nitrogen gas over them. Finally they were placed in an oven at 50 ^{o}C for 1h so that the volatile impurities on the glassy carbon surface could be removed.

6.2 IMPLANTATION OF EUROPIUM

After cleaning, the glassy carbon sample were implanted by europium ions at four different temperatures, i.e. at room temperature (RT), 100 ^{o}C, 150 ^{o}C and 200 ^{o}C. This was done using the 400 keV ion implanter Romeo at the Institut für Festkörperphysik, Friedrich-Schiller Universität Jena, Germany. The europium implantation at all four different temperatures was performed at the energy of 250 keV with a fluence of 1×10^{16} Eu^{+}/cm^{2}. Because our study also investigated radiation

damage as a result of the ion implantation, the flux was kept at 10^{12} ions/cm^{2}s. This was also done to avoid the annealing of some damage due to the increase of the sample temperature during implantation.

After implantation, the samples were cut manually. Since the cutting instrument in our laboratory (Accutom cutter) works with water, we could not use that set up to cut our implanted samples.

6.3 SAMPLE ANNEALING

Investigation of diffusion behavior as a result of different temperatures was performed by annealing. Isochronally annealing was done for all four different temperature implanted samples. The implanted samples were annealed in a quartz tube furnace at a vacuum condition. Figure 6.1 shows a schematic diagram of the annealing set up at University of Pretoria (UP). The sample was placed in a quartz tube sample holder.

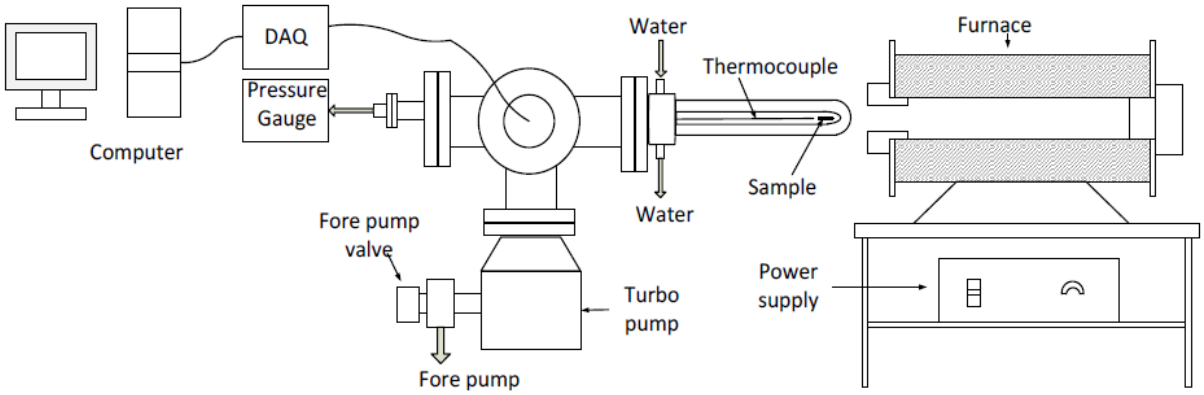

Fig. 6.1. A tube furnace annealing set up in UP. Obtained from [Njo14]

One end of the thermocouple is connected to the sample inside the tube and the other end goes through the chamber and into the DAQ (data acquisition) system for measurement. The thermocouple was connected to a data acquisition system which was interfaced to a computer to store and collect the annealing data. The fore pump initially evacuated the quartz tube up to 10^{-3} mbar and then the turbo pump was switched on. The two pumps together were running and after few minutes the vacuum reached 10^{-6} mbar. The preset annealing temperature (after the furnace

was switched on), allowed to obtain the stable and desired temperature. The quartz tube with the sample inside was then pushed into the furnace. Data acquisition was running on the computer during all the steps. After finishing the annealing, the quartz tube was pulled out from the furnace to allow the sample to cool down and reach room temperature. All four sets (i.e. different implanted temperatures) of samples were annealed from 200 to 1000 ºC in steps of 100 ºC for 1h. In addition, one of the room temperature europium implanted sample was annealed isochronally from 300 to 500 ºC in steps of 25 ºC for 2h. Figure 6.2 shows the typical annealing curves at 500 and 900 ºC for 1h. The RBS, Raman spectroscopy and SEM analysis were done after every step of annealing to investigate any structural (surface) changes.

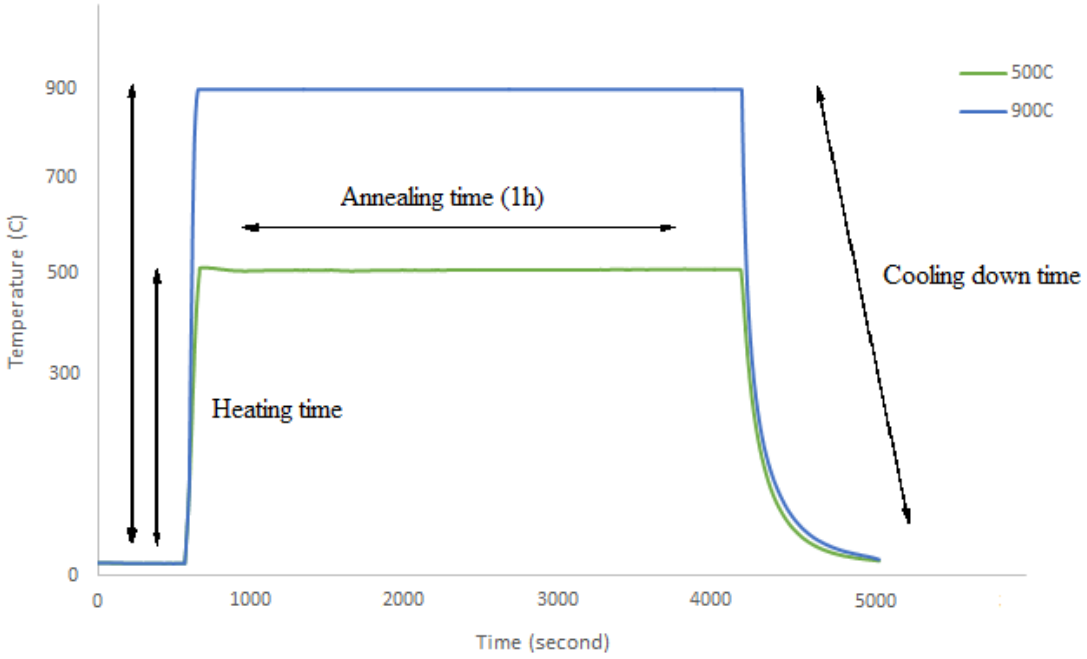

Fig. 6.2. Graph showing the typical annealing process at different temperatures for 1h.

6.4 MEASUREMENT CONDITIONS

6.4.1 RBS MEASUREMENT CONDITIONS

The europium implanted glassy carbon was analyzed using Rutherford backscattering Spectrometry (RBS) measurement after every step of annealing. The samples were irradiated by 1600 keV alpha particles ($^{4}He^{+}$ ions) in a Van de Graaff accelerator at University of Pretoria. The

beam current was kept between 10-15 nA to minimize heating. The charge during every single measurement was controlled to be 8 μC. To ensure the accuracy and decrease of noise of the measurement, the RBS measurement was done three times and the average of the three sets of the RBS data was taken at each channel number. A solid angle of 3.41 msr for a surface detector barrier was located at a scattering angle of 165^{o} to the beam direction.

6.4.2 RAMAN SPECTROSCOPY MEASUREMENT CONDITIONS

Using a Jobin Yvou Horiba TX64000 Raman spectroscopy, located at University of Pretoria, the structural changes after ion implantation and heat treatment was investigated. The excitation laser used was a gas laser comprising of a mixture of Ar/Kr to emit a beam with the wavelength of 514.5 nm. The objective magnification of the optical microscope was selected to be 50X for all measurements to be ensure identical measurement conditions for all data sets. In order to prevent sample heating, the laser power was held at $\leq$ 10 mW.

6.4.3 SEM MEASUREMENT CONDITIONS

Surface modification of implanted and annealed samples was investigated using the Zeiss Ultra Plus scanning electron microscope (SEM) at the University of Pretoria. An analyzing voltage of 2kV was applied in this study. SEM images were obtained before and after the implantation of the glassy carbon samples by europium and after every annealing step. In-lens SEM images were obtained to study of surface changes. The micrograph scale of 10, 2, 1 μm and 200 nm was acquired for all samples in each step of experiment. The working distance (between the surface of the sample and the detector) was also kept between 1.6 and 3.5 nm.

REFERENCE

[Njo14] E. G. Njoroge, "Solide-state interaction between Zr thin films and SiC", University of Pretoria, 2014.

CHAPTER 7

INVESTIGATION OF IMPLANTED EUROPIUM IN GLASSY CARBON

In this chapter, the europium (Eu) implantation into glassy carbon and its heat treatment are presented and discussed. The diffusion behavior of europium implanted at different temperatures and post-implanted annealing was investigated by Rutherford backscattering spectrometry (RBS). The microstructural modification of the samples was investigated by Raman spectroscopy while the surface morphology of the samples was studied by scanning electron microscopy (SEM).

7.1 EU-IMPLANTED RESULTS

7.1.1 AS-IMPLANTED EUROPIUM DEPTH PROFILE

Figure 7.1 shows a comparison between the 250 keV europium implanted depth profile at room temperature and the SRIM [Zie13] simulated profile. The reason using of SRIM was to compare the theoretical and experimental results and showing that the R_p value from the experimental results is almost in agreement with that from the SRIM program (ignoring the error measurement). The other using of SRIM is to calculate the average vacancy concentration by the atomic density of GC. Essentially, the dpa parameter is proportional to the energy density deposited by the incoming ion in nuclear collisions. Because SRIM does not take into account dynamic annealing or the effect of multiple impacts, the dpa parameter almost certainly overestimates the actual damage density for a given ion dose [McC94].

The SRIM simulation was carried out considering the glassy carbon density of 1.42 g/cm^3. This value is for Sigradur glassy carbon used in this study. As was discussed in section 3.4, in order to extract the four moments of the experimental profile, an Edgeworth function was fitted to as-implanted profile. A comparison between the four moments of the two profiles is given in Table 7.1. From the Figure 7.1 it can be seen that the experimental as-implanted profile is slightly shifted towards the surface. This is also confirmed by the different values for the projected ranges of the two distributions, see Table 7.1.

The as-implanted profile is significantly broader than the SRIM profile, as also shown by the range straggling values. The experimental projected and straggling range for the room temperature implanted europium were 125 nm and 35 nm, respectively. While the R_p and ΔR_p values for room temperature implanted sample calculated by SRIM were 130 nm and 21.5 nm, respectively. The discrepancy in the projected ranges was about 4% (the experimental R_p was less than the one by SRIM). The two projected ranges are effectively in agreement with each other because the experimental error (about 5-10%) for depth profile. From Table 7.1 there is a discrepancy between the projected range straggling calculated by SRIM and the one obtained from the experimental data. The reason for the difference in the experimental and theoretical (obtained by SRIM) values can be attributed to some assumptions made in the SRIM program (as mentioned in Chapter 3) such as;

- The SRIM program assumes only binary collisions and the effects of neighbouring atoms are neglected.
- The SRIM program considers the target as an amorphous material with random atom locations. Thus the properties of the crystal lattice are ignored. (It must be noted that glassy carbon has a fullerene-related structure.)
- The recombination of vacancies and interstitial atoms resulting from bombardment processes is neglected by the SRIM program.

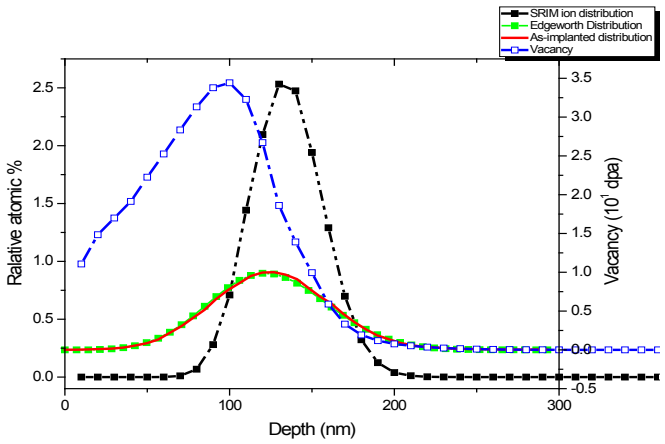

Fig. 7.1. A comparison between the 250 keV europium implanted depth profile at room temperature (red line), the fitted Edgeworth distribution (green dots) and the SRIM simulated profile (black dotted line). Also shown in blue dots is the vacancy distribution as calculated by SRIM.

For this study, another important aspect follows from the values of the third and fourth moments of the as-implanted profile. They show that this profile is very near to a Gaussian profile. From equations (3.30) and (3.31), it follows that a perfect Gaussian profile the skewness $\gamma = 0$ and the kurtosis $\beta = 3$ for the Edgeworth function. The as-implanted values of $\gamma = 0.17$ and $\beta = 2.89$ are very near these ideal ones. The profile is nearly symmetric because a γ value between $-0.5 < \gamma < 0.5$ is generally accepted to give a fairly symmetric profile. A positive sign for γ implies that the depth profile was skewed behind R_p. The fact that the as-implanted profile is nearly Gaussian is important for this study because it means that to determine the diffusion coefficient D from annealed samples/profiles, the solution to the Fick diffusion equation for an initial Gaussian profile by Malherbe *et al*. [Mal17] can be used.

Figure 7.1 also shows the vacancy distribution obtained by SRIM. From this figure it can be seen that the maximum of the vacancy distribution is at about 100 nm below the surface of the glassy carbon substrate. This is less than the projected range of the experimental depth profile of room temperature as-implanted europium in glassy carbon. The vacancies distribution was skewed towards the surface of the glassy carbon substrate.

The number of vacancies produced as a result of Eu implanted in glassy carbon was shown in 7.1. The figure shows that most of the damage introduced in glassy carbon due to Eu bombardment are mostly concentrated towards the glassy carbon surface.

Table 7.1. The experimental R_p, ΔR_p, γ and β values of europium implanted glassy carbon at room temperature with SRIM obtained values

	Projected range (Rp)	**Range straggling (ΔR_p)**	**Skewness (γ)**	**Kurtosis (β)**
SRIM simulation	130 nm	21.5 nm	0.16	2.96
As-implanted profile	125 nm	35 nm	0.17	2.87

7.1.2 RAMAN SPECTRUM OF PRISTINE GLASSY CARBON AND GLASSY CARBON IMPLANTED WITH EU AT ROOM TEMPERATURE

In disordered carbons, the Raman spectra are dominated by two significant peaks, the D peak and G peak. These modes of graphite appear even when the carbon does not have particular graphitic order [Fer04]. The σ- and π- bonds (explained in Chapter 2) have different energies. The σ-bond has a higher energy than that the π-bond, which makes it less polarizable. This causes the sp^3 sites to have a smaller Raman cross-section than the sp^2 sites which leads to the dominance of sp^2 sites [Rob02]. The presence of the G and D peaks illustrate the sp^2 and sp^3 carbon network, respectively.

Figure 7.2 shows the Raman spectra of pristine glassy carbon. The first peak is the D (so-called disorder) peak at 1348 cm^{-1} and the second peak is the G peak at 1594 cm^{-1}. The G peak is defined as the E_{2g} mode of graphite and the D peak is attributed to the disorder mode of graphite. Both the D and G peaks appear in the Raman spectra of carbon based materials with sp^2 bonds which are accompanied by disorder. To analyse the obtained Raman spectra, both the G and D peaks were fitted by the Breit-Wigner-Fano (BWF) function. The Raman spectrum of pristine glassy carbon is in agreement with those from McCulloch *et al.* [McC94]. They found the D peak and G peak positions at 1355 cm^{-1} and 1590 cm^{-1}, respectively. Although they fitted the Lorentzian function to the D peak and the BWF function to the G peak, in our study the BWF function gave excellent fits for both D and G peaks (see Figure 7.2).

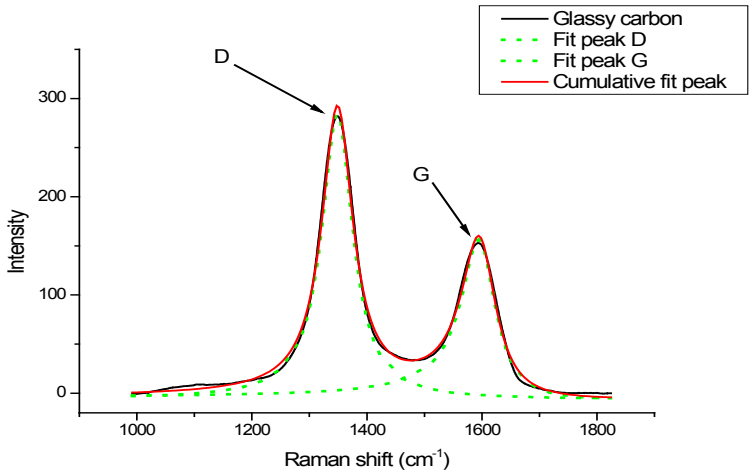

Fig. 7.2. Raman spectra of virgin glassy carbon which was obtained at 514.5 nm excitation wavelength. The coloured lines in spectra show the BWF fitting.

The height of D and G peaks were taken as their intensities. To estimate the crystal size of pristine glassy carbon, Tuinstra-Koenig (TK) relation was used which is given by [Tui70]:

$$\frac{I_D}{I_G} = \frac{C_\lambda}{L_a} \tag{7.1}$$

where C_λ for the 514.5 nm laser light is from previous studies [Tui70], [Mat99], [Lav08] equal to 44 Å. The Tuinstra-Koenig relationship is valid for a wide range of carbon materials with sp^2 bonds over the range of 2 nm $<$ L_a $<$ 300 nm when using the 514.5 excitation wavelength [Tui70]. The I_D/I_G ratio in this study for the pristine glassy carbon was calculated about 1.8. Thus, the average crystal size of glassy carbon (L_a) was 2.5 nm. This value for the crystal size of glassy carbon means that glassy carbon can be categorized as the nano-crystalline graphite [Fer07].

Figure 7.3 shows the Raman spectra after ion bombardment. Implantation caused the two distinct peaks (D and G peaks) to merge into a single broad peak. This is an indication that the implanted layer became amorphous, see e.g. [Fer04], [McC94], [Lav08], [Odu16], [Njo17], [Hla17], [Fer00], [Lan12], [Odu18]. Using the BWF fitting, the G peak shifted to lower position at 1540 cm^{-1} while the D peak position increased to 1360 cm^{-1}. The G peak position after ion implantation is similar to the G position of ion beam-sputter deposited carbon films [Dil84]. Several studies on ion bombardment of glassy carbon (i.e. by Sr [Odu16], In [Njo17], Cd [Hla17] and Ti [Tak85]) have shown that when the implanted region becomes amorphous then there is a reduction in the G peak wavenumber accompanied with an increase in the FWHM of the G peak.

In this study, the G peak moved to a lower wavenumber (from 1594 to 1540 cm^{-1}) and the FWHM of the G peak also increased from 71.5 (pristine glassy carbon) to 212 cm^{-1} after europium implantation. This is another proof that 250 keV Eu ion bombardment caused the amorphisation of the implanted region of the glassy carbon.

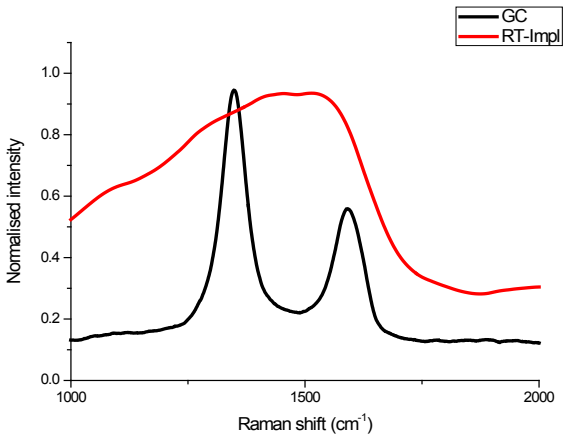

Fig. 7.3. Normalised Raman spectra for pristine glassy carbon and 250 keV europium implanted at room temperature in glassy carbon

Figure 7.4 shows the fitting of the Eu implanted Raman spectra with both BWF and Lorentz functions. It can be seen that in both fittings, the implanted Raman spectra cannot be fitted well with the applied functions. But applying both functions showed the reduction of G peak to lower wavenumber (1540 cm^{-1} for BWF fitting and 1545 cm^{-1} for Lorentz fitting). By fitting the Raman spectra with the BWF function, (we have chosen BWF fitting because it fitted the pristine glassy carbon Raman spectra well) the I_D/I_G ratio after ion implantation decreased significantly from 1.8 (pristine glassy carbon) to 0.67. The decrease of the I_D/I_G ratio after europium ion bombardment can be explained by the amorphisation trajectory [Yan91]. Amorphisation trajectory relates the sp^3 content in carbon materials to the I_D/I_G ratio. The drop of I_D/I_G after europium ion implantation suggests that about 15% of the sp^2 bond was converted to the sp^3 bonds.

To calculate the content of sp^2 and sp^3 bonds, we need to use Electron Energy Loss Spectroscopy (EELS). We did not use the EELS measurement in this study, however it will be the next plan in future. Some studies [Lav08] and [McC94] measured the converting of sp^2 to sp^3 in glassy carbon after ion bombardment at a dose of 1×10^{16} ions/cm^3. They also reported a decrease of the I_D/I_G ratio. For example, McCulloch *et al*. [McC94] reported that I_D/I_G ratio decreased from 1.2 to 0.2 after xenon bombardment in glassy carbon. Lavrentiev *et al.* [Lav08] also showed that this ratio decreased from 1.5 to 0.69 after the implantation of cobalt in glassy carbon. They showed that

about 15 % of the sp^2 bond was converted to the sp^3 bond. In this study the I_D/I_G ratio decreased from 1.8 to 0.67 which is in agreement with the Lavrentiev *et al.* report.

According to the Three-stage model [Fer00], the decrease in I_D/I_G ratio and the shifting of the G peak to a lower wave number suggests also a relative increase in the number of sp^3 bonds and a reduction of the sp^2 content in the implanted glassy carbon substrate. Using the equation (7.1) to calculate the crystal size after ion implantation a value of about 6.5 nm was obtained. Above it was shown that the Eu ion bombardment led to an amorphous surface. This paradox (amorphous surface and increasing the crystal size after ion implantation), can be attributed to the fact that the Raman spectra after ion implantation could not be fitted well by the BWF functions (Figure 7.4).
In our results there are errors in measurement set up and fitting functions (BWF, Lorentz, etc.).
One of the most obvious sources of error in Raman scattering is the limited resolution of the spectrometer. However, the main source of error lies in the monochrometer [Gor10].
According to Juang *et al.* [Jua88], the limiting resolution DR is given by equation below:

$$\text{Depth Resolution (DR)} = 2.2\pi\lambda / n\,(NA)^2 \qquad (7.2)$$

where *n* is the refractive index of the immersion medium, λ is the laser wavelength, and NA is the numerical aperture of the focusing lens. In the other word, optical calculations for depth resolution of an optical microscope state that DR is proportional to $\lambda/(NA)^2$ [Ada10].
The sample displacement along the *z*-axis was defined by the symbol Δ. In practical terms it corresponds to the displacement of the microscope stage, in micrometers, relative to the position where the laser is focused on the sample top surface. If Δ = 0, the laser beam is focused on the air–sample interface, and positive values of Δ imply sample movement opposite to the beam propagation direction (that is, moving the laser focus into the sample) [Gor10].
In case of systematic error, for a confocal Raman microscopy, as it is usually practiced, has a much worse depth resolution than is commonly assumed, by an order of magnitude or more. This performance degradation occurs when depth profiling by the ‘‘optical sectioning’’ approach, whereby one focuses the laser beam onto the surface of a sample, records a spectrum, and then moves the focus incrementally deeper into the material, obtaining a spectrum at every point.
For convenience, the most important quantitative results are summarized below [Eve00]:
(i) The refraction-limited depth resolution (i.e., the length of the region illuminated by the laser beam) is given by Equation below:

$$DR = \Delta \left[\left[\frac{NA^2(n^2-1)}{(1-NA^2)} + n^2\right]^{\frac{1}{2}} - n\right] \quad (7.3)$$

where in which NA is the numerical aperture of the objective, n is the refractive index of the sample, and it is assumed that the laser beam just fills the objective. Thus the depth resolution (DR) gets worse linearly with Δ.

This equation (equation (7.3)) is very important. For example, it predicts that for a 0.95 NA objective and a sample index $n \sim 1.5$, the depth resolution is ~ 2.2Δ.

(ii) All points within the illuminated region lie much deeper than the nominal point Δ; even paraxial rays originating near the center of the objective are focused to a point $z = n\Delta$, rather than at $z = \Delta$ (z-axis is assumed to be normal to the sample surface). Marginal rays are focused even deeper, with the entire illuminated region being bounded by $z = n\Delta$ and $z = (n\Delta + DR)$. This effect is very important; e.g., for a 0.95 NA objective and $n \sim 1.5$ sample, data are actually acquired from a broad region, centered about 2.5 X deeper than the apparent depth Δ. Interpreting the structure of a multilayer sample from z-scan Raman data is impossible unless refraction is taken into account, and this has apparently rarely been done in the literature.

(iii) The use of a confocal aperture does not significantly improve the depth resolution. Refraction allows (some) rays emanating from the whole focal volume to pass through the pinhole.

(iv) For coatings deposited on thick substrates, the substrate intensity rises relatively slowly as we increase Δ. This make the interfacial thickness appear broad even for very sharp interfaces. The z-scanning approach is not recommended for studying interfacial phenomena.

(iiv) An immersion objective with a suitable index matching fluid should minimize refraction at the sample surface, and should improve the depth resolution by focusing all rays close to the apparent depth Δ [Eve00].

In our study λ (Laser wavelength) = 514.5 nm, NA = n sinθ where n = 1.78 (for glassy carbon [Dul84]) and θ = 9º (according to Raman measurement at University of Pretoria). Then we have:

$DR = 514.5 / (1.78 \sin 9^o)^2 = 6769.7$ nm = 0.67 µm

Equation (7.3), taken literally, implies that the depth resolution improves monotonically as NA increases. Our result is in agreement with the Barbillat *et al.* report [Bar94] with a 514.5 nm laser and an objective with NA = 0.95, the expected depth resolution is 0.6 µm. Tabaksblat *et al.* [Tab92] made calculations and practical determinations of the depth resolution as a function of the

numerical aperture of the objective, the microscope magnification, and the size of the pinhole, and concluded that a resolution of ~ 2 μm was obtained with a 100X objective and a 100-μm pinhole. Before taking any data, the Rayleigh peak was located. Because this is the peak that occurs when the incident and scattered photon have the same wavelength, it occurs at the same wavelength for all of the samples. Thus, this was a systematic error that needed to be corrected.

The fitting results depends on the operator which it has been used. For example McCulloch et al. [McC94] reported that applying the Lorentzian + BWF led to the best fitting for pristine glassy carbon Raman spectra (D and G peaks). But in our study the BWF fitting led to the best result for pristine glassy carbon. Furthermore as it can be seen in figure 7.4, there is not a good fitting for both peaks, D and G peaks. However, between the Lorentzian and BWF fitting after ion implantation, the BWF led to better fitting. Thus we choose the BWF fitting for better comparison between the pristine glassy carbon and that as implanted.

As stated in the thesis the "irrational" result of a crystal size after irradiation being larger than before irradiation is probably due to the poor fit of the spectra. We are not aware of any publication reporting that the appearance of sp^3 bonds affecting the Tuinstra-Koenig formula via negative way. In fact, the D peak used in this formula is partially due to sp^3 bonds.

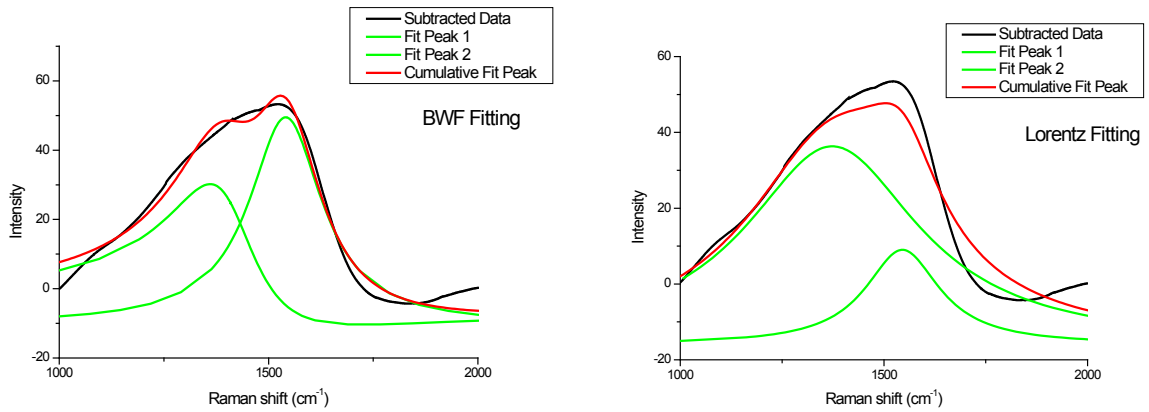

(a) (b)

Fig. 7.4. Raman spectra of europium implanted glassy carbon at room temperature fitted to (a) the BWF, and (b) Lorentzian functions. The red line is the cumulative peak and the green lines are the individual fitted peaks.

7.2 ROOM TEMPERATURE IMPLANTED AND ANNEALED RESULTS

7.2.1 RBS RESULTS OF GLASSY CARBON IMPLANTED WITH EU AT ROOM TEMPERATURE AND ISOCHRONALLY ANNEALED FOR 1H

To investigate the diffusion behaviour of europium implanted in glassy carbon at higher heat treatment behaviour, a room temperature implanted sample was sequentially annealed from 200-1000 ^{o}C in steps of 100 ^{o}C for 1h. RBS depth profiles were measured after each annealing step shown in Figure 7.5 (a). Figure 7.5 also shows Gaussian fitting plots of samples annealed at 200 and 400 ^{o}C annealing 7.5 (b). As can be seen, there are two different diffusion processes. Annealing up to 300 ^{o}C resulted in general broadening of the Eu depth profiles, i.e. normal Fickian diffusion. To extract the diffusion coefficients from the RBS depth profiles at 200 ^{o}C and 300 ^{o}C, the depth profiles were fitted to the solution of the Fick diffusion equation for an originally Gaussian profile [Mal17].

The diffusion coefficients of Eu at 200 ^{o}C and 300 ^{o}C annealing temperatures are $D = 2.3 \times 10^{-19}$ m^2/s and $D = 1.2 \times 10^{-19}$ m^2/s, respectively. Both these two diffusion coefficient are at the limit which can be determined with this method and would have an error of about 20%. What is particularly interesting about these two values is the decrease in the diffusion coefficient at the higher temperature compared to the one at the lower temperature. This is contrary to normal diffusion and is an indication that the microstructure of the glassy carbon was different during the two measurements. The sample annealed at 200 ^{o}C was taken from its as-implanted (amorphous) state to it annealing temperature. The same sample was, after RBS, Raman and SEM measurements, then annealed at 300 ^{o}C. Although not really visible (only for the 300 ^{o}C annealed sample) in the Raman spectrum (discussed in next section), this first annealing at 200 ^{o}C for 1 h caused enough microstructural changes to have led to decrease in the diffusion coefficient.

The depth profiles changed for the samples annealed at 400 ^{o}C and higher. The europium profiles are deeper inside the glassy carbon as can be seen in Figure 7.5. In this figure the data points were also fitted to a Gaussian function. From the good fit, the position of the maximum of the profile was determined to be at 138 nm while for the 300 ^{o}C profile it was at 115 nm. The 400 ^{o}C profile also became significantly more narrow, i.e. with a ΔR_p ($=\sigma$) = 31 nm while for the 300 ^{o}C profile a Gaussian fit to the experimental points gave ΔR_p = 49 nm. Furthermore, there was also no

increased broadening (i.e. ΔR_p remained around 31 nm) of the profiles with increasing annealing temperatures above 400 ºC. The latter is contrary to what is expected of normal Fickian diffusion [Fer04]. This behavior is not uncommon in other systems (e.g. see [Mal13] for examples in SiC) and depends on changes in the microstructure of the substrate in which the diffusion occurs. However, the shifting of the profiles deeper inside the glassy carbon is much more problematic to explain. It is probably due to stress between the damaged layer and the pristine bulk leading to a migration of the profile as a whole.

We expected the more diffusion to the surface at higher temperatures. But we saw the inverse. We planned to repeat this experiment to be sure about our result. One reason for this value (30%) europium loss at 400 ºC – 1000 ºC may be the RBS error measurement (5-10%). Another reason can attributed to the europium compounds (with O or C) which have small contents compared with the pure europium ions. These contents were indicated in RBS profiles as small peaks (which were not shown in thesis).

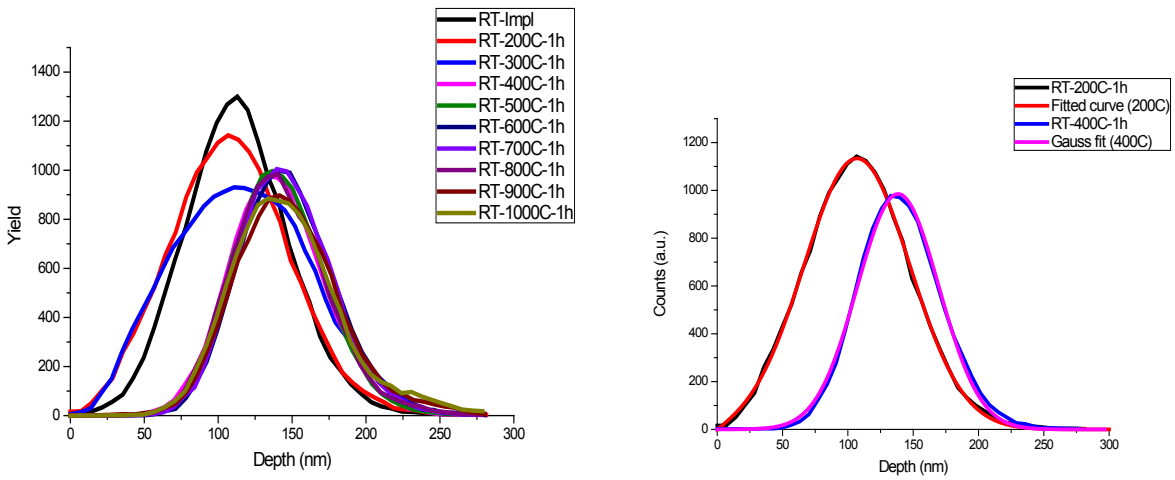

(a) (b)

Fig. 7.5. (a) The RBS yield as a function of depth of europium implanted at room temperature in glassy carbon, and after heat treatment. (b) A fit of the equation in [Mal17] to the europium RBS depth profiles after the samples were annealed at 200 ºC and after 400 ºC.

Figure 7.6 shows the retained europium after annealing at some temperatures between 200 and 1000 °C. This was done by comparing the areas under the profiles to that of the room temperature implanted profile. For the 200 and 300 °C samples there was a slight increase in these areas. The gained values were about 5 and 8%, respectively. This may because of the error of measurement, which we estimate to be between 5 to 10%. Annealing at 400 ºC led to europium lost about 30%. The europium retained value (70%) at higher annealing temperatures almost constant and similar to that at 400 ºC, see Figure 7.6.

There are two possible sources for this loss. Some of the europium was lost through diffusion to the surface and subsequent sublimation into the vacuum. The SEM images, discussed in section 7.2.3, confirmed this explanation. There is also another possibility for this loss. As mentioned above, annealing at 400 ºC also resulted in a narrowing of the Eu profile. The Eu in the original, broader tails of the profiles probably also dissolved and diffused in the glassy carbon to levels below the detection limit of RBS. In this respect, it must be noted that Eu reacts with carbon to form a carbide. Annealing at the higher temperatures did not result in any further loss of the europium because the profiles remained static at these temperatures, probably because of the carbide formation.

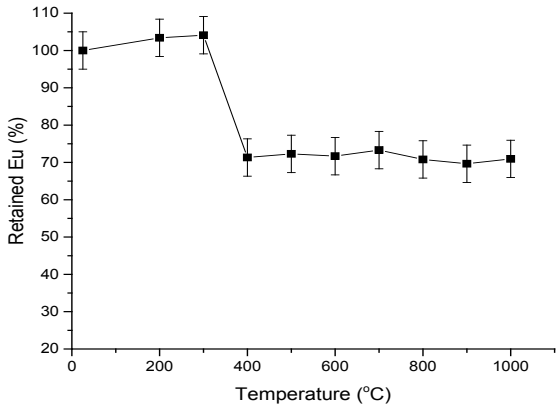

Fig. 7.6. Retained value of Eu-implanted at room temperature (with an estimated 5% error bar) after annealing at 200-1000°C for 1h.

7.2.2 RAMAN RESULTS OF GLASSY CARBON IMPLANTED WITH EU AT ROOM TEMPERATURE AND ISOCHRONALLY ANNEALING FOR 1H

To investigate the ion beam induced damage effects, glassy carbon was implanted by 250 keV europium ions. The Raman analysis for pristine glassy carbon, room temperature implanted glassy carbon and post-implanted annealing at 200-1000 °C for 1h was done using a 514.5 nm laser. Figure 7.7 shows the normalized Raman spectra for some of the annealing temperatures. In section 7.1.2, we mentioned that after ion implantation the two distinct peaks merged as a single broad peak and discussed the reason for this. In this section we shall only discuss the Raman results after heat treatment. From Figure 7.7, it can be seen that after annealing at 300 and 400 ^{o}C, the two peaks (D and G peaks) can be slightly distinguished. By increasing the temperature to 900 and 1000 ^{o}C the two peaks reappeared but still superimposed on the broad merged peak. This means that partial recovery of glassy carbon structure occurred.

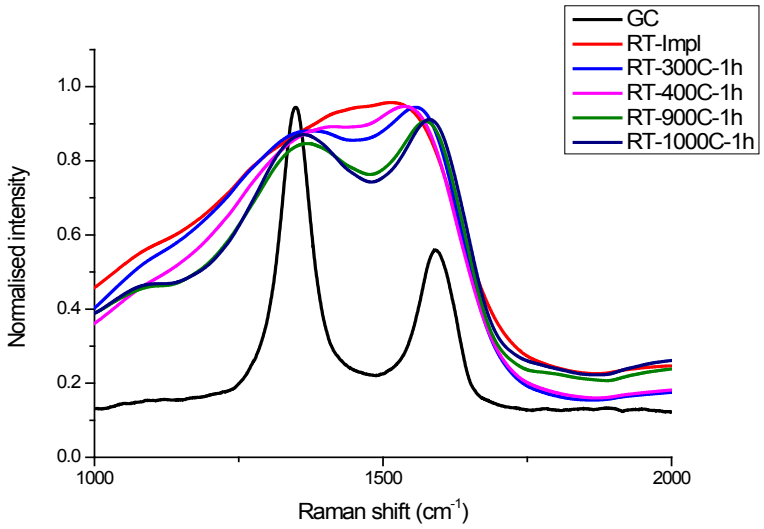

Fig. 7.7. Raman spectra of pristine glassy carbon implanted at room temperature and annealed at 300, 400, 900 and 1000 °C for 1h.

Using the BWF fitting, the G peak wavenumber changed from 1540 cm^{-1} for the room temperature implanted sample to 1549 cm^{-1} for the implanted sample annealed at 300 ^{o}C. The G peak position

also increased from 1549 cm^{-1} at 300 ºC to 1587 cm^{-1} at 1000 ºC. The D peak position decreased from 1360 cm^{-1} (as-implanted) to the 1349 cm^{-1} at 300 ºC and then increased to the 1375 cm^{-1} at 1000 ºC (Figure 7.8). As discussed in section 7.1.2, these two facts imply partial recovery of glassy carbon structure. However annealing at 1000 ºC for 1h, did not cause the G peak position reached to that of the pristine glassy carbon (1594 cm^{-1}). This means that the annealing temperature/time was not sufficient to recover totally the glassy carbon structure.

From a BWF fitting the peak heights of the D and G peaks, viz. the I_D and I_G values, can be obtained. The I_D/I_G ratio at room temperature was about 0.67 which increased to 0.86 at 300 ºC. From equation (7.1), the crystal size at 300 ºC was obtained about 5.3 nm. Then the I_D/I_G ratio reduced from 0.86 to 0.83 at the 400 °C. At this temperature the crystal size increased (by a small amount, which is with the experimental error of 5-10%) to the 5.4 nm. The I_D/I_G ratio reached 0.74 at 1000 ºC heat treatment for 1h. Using the equation 7.1, the crystal size obtained was about 5.9 at this temperature. Increasing the D peak position (Figure 7.8) shows that the glassy carbon structure was more disordered from 400-1000 ºC. The results are given in Figure 7.9. The difference of the crystal size after annealing at 400 ºC compared at 1000 ºC is about 0.5 nm (not large).

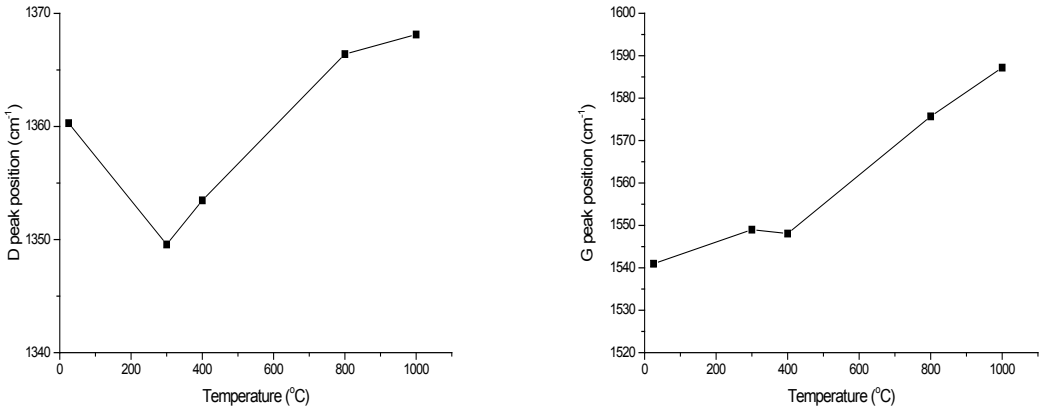

Fig. 7.8. G and D peak positions obtained from Raman spectra after fitting with the BWF function for RT-implanted and annealed between 200-1000 ºC for 1h

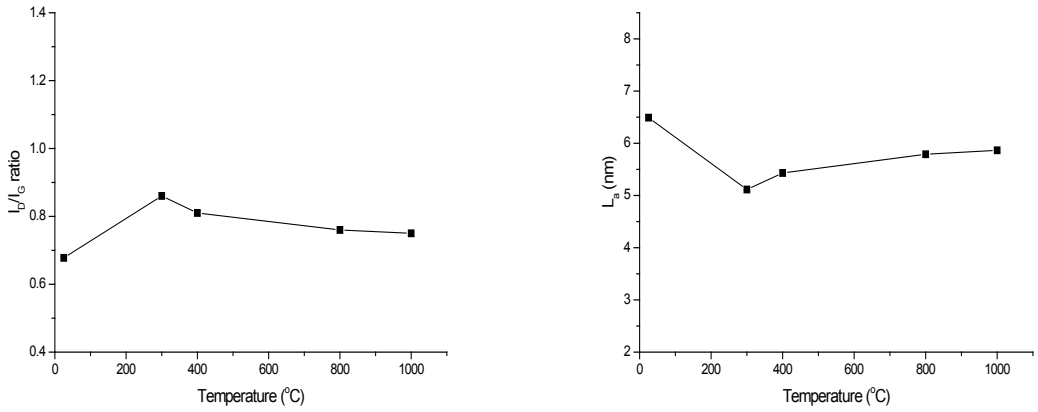

Fig. 7.9. I_D/I_G ratio and L_a values obtained from Raman spectra after fitting with the BWF function for RT-implanted and annealed between 200-1000 °C for 1h

7.2.3 SEM IMAGES OF GLASSY CARBON IMPLANTED WITH EU AND ISOCHRONALLY ANNEALING FOR 1H

To investigate the surface topography of the glassy carbon before and after the europium ion implantation, and after the isochronal annealing, SEM analysis was done on the samples. Figure 7.10 shows the SEM images of (a) pristine glassy carbon, (b) room temperature implanted europium in glassy carbon, and annealed for 1h at (c) 300 °C and (d) 1000 °C, respectively. The SEM image of pristine glassy carbon shows a smooth surface with scratches due to mechanical polishing. The reason for the smooth surface of pristine glassy carbon can be stated that during the mechanical polishing some of loosened glassy carbon particles the polished particle were deposited in the scratch marks. This means that polishing and then subsequent cleaning the surface did not remove the particles from the scratch marks.

After ion bombardment (Figure 7.10 (b)) those polishing marks became more prominent. This can be explained by enhanced sputtering in the scratch areas. According to the Sigmund theory [Sig69] the sputter yield of a solid surface depends (inter alia) on the surface binding energy of the surface atoms. The mechanical polishing particles damaged the surface which led to stress in the damage region. Thus the binding energy of surface atoms in this region reduced which led to an enhanced sputtering rate compared to the neighbouring regions and thereby exposed the polishing lines.

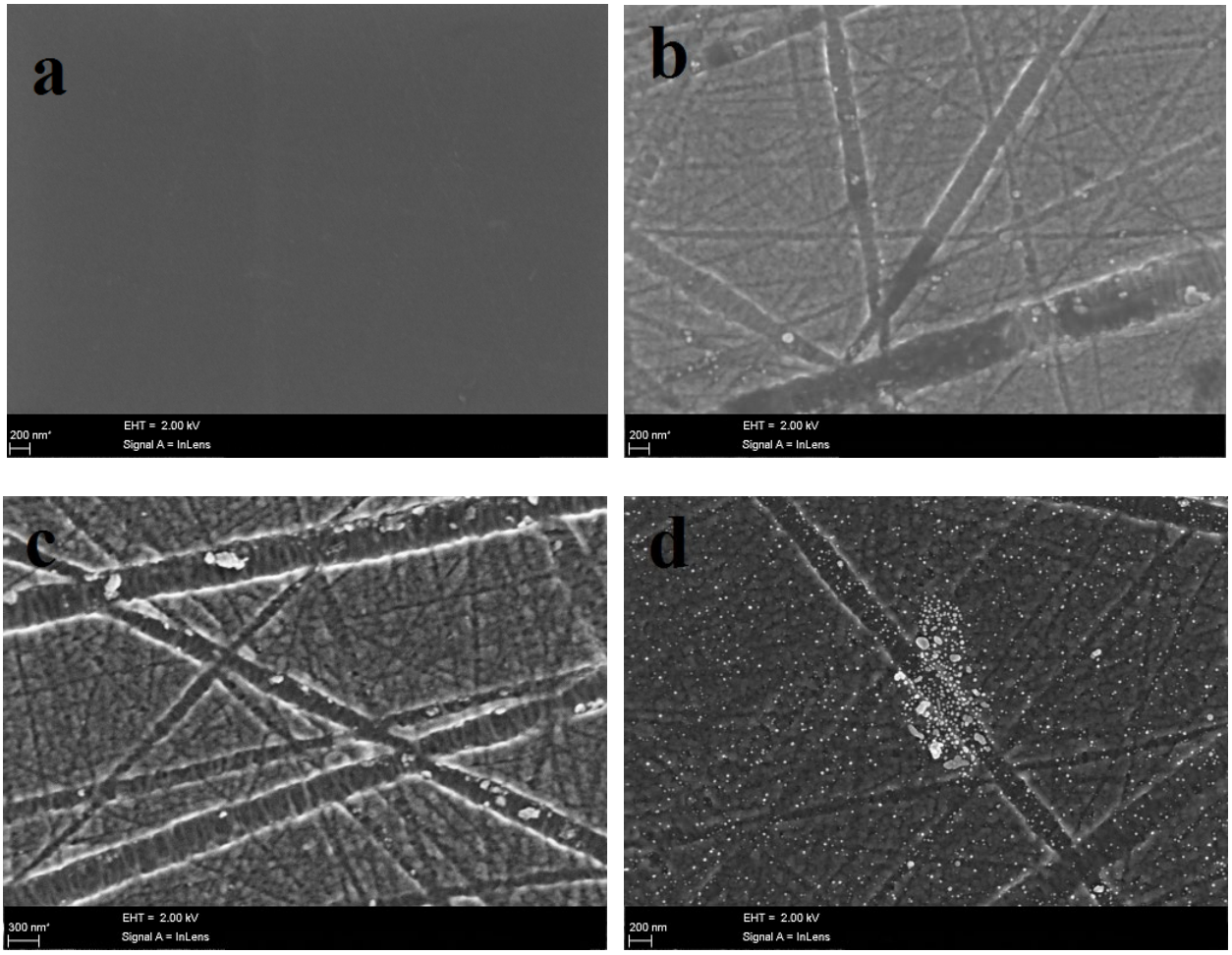

Fig. 7.10. SEM images of (a) pristine glassy carbon, (b) room temperature implanted Eu in glassy carbon, (c) annealed at 300°C and (d) 1000°C for 1h.

Figure 7.10 (c) shows the image of the sample after annealing at 300 ºC for 1h. The polishing lines are also clearly visible. The crystals appeared in the polishing lines. Figure 7.10 (d), shows that annealing at 1000 ºC led to some conglomeration of the crystals, even beyond the polishing lines. The particles/crystals appeared after annealing at 1000 ºC on the surface are ball-like (obtained at the higher magnification was not shown here). The one possibility for these ball-like crystals on the surface is that it can be attributed to the retained Eu on the surface which combined with the oxygen and formed Eu_2O_3. This image (7.10 (d)) is similar to the work of Li *et al*. [Li11] on the synthesis of the mesoporous Eu_2O_3 microsphere particles. The reason why the Eu-containing crystals tend to appear in the polishing lines may be due to the stress in these grooves leading to

change in the Gibbs free energy of the surface and near-surface atoms thereby affecting the out-diffusion rate of the europium.

Gebelt and Eick [Geb66] found a phase of apparent composition $EuC_{1.87}$ in equilibrium with graphite at 1000°C. H^o_f ($EuC_{1.87}$) at 298.15 K = -9.17 kcal/mol = -0.4 eV (the $4Eu + 3O_2 = 2Eu_2O_3$ reaction is exothermic reaction) and H^o_f (Eu_2O_3) at 298.15 K = -394.45 kcal/mol = -17.11 eV. The standard heat of formation (Enthalpy of formation) is H^o_f and the standard free energy of formation is G^o_f . This confirms that the formation of Eu_2O_3 is easily proceeded because of much more stable reaction in terms of heat of formation. This could be observed in the higher temperatures.

Thus, atoms at the high energy end of the Maxwell-Boltzmann distribution can react to form this carbide. Because it is exothermic, the reaction can continue. This might be the reason why we found such a strange diffusion behavior. At lower temperatures there is some Fickian diffusion of the Eu. At the higher temperatures, this carbide formation might occur. Because it is more difficult for a large compound to diffusion, only the Eu atoms, which segregate to the surface, diffuse but also form this carbide with the carbon atoms in the substrate.
For the proof of the compound/particles on the surface after heat treatment at higher temperature we planned to do XPS measurement, but unfortunately it did not work that time, but we plan to do it in future. Furthermore, as stated in thesis, the one possibility for these ball-like crystals on the surface is that it can be attributed to the retained Eu on the surface which combined with the oxygen and formed Eu_2O_3. This image (10 (d)) is similar to the work of Li et al. [Li11] on the synthesis of the mesoporous Eu_2O_3 microsphere particles. The reason why the Eu-containing crystals tends to appear in the polishing lines may be due to the stress in these grooves leading to change in the Gibbs free energy of the surface and near-surface atoms thereby affecting the out-diffusion rate of the europium. This stress-induced lowering of the surface energy may also lead the reaction to take place at a lower temperature.

7.2.4 RBS RESULTS OF GLASSY CARBON IMPLANTED WITH EU AT ROOM TEMPERATURE AND ISOCHRONALLY ANNEALED FOR 2H

The RBS measurements were done for 250 keV Eu implanted in glassy carbon at room temperature and then annealed isochronally for 2h but sequentially, from 300-500 ^oC (in steps of 25 ^oC). Figure

7.11 shows the RBS depth profiles of room temperature implanted and annealed samples at these temperatures. We considered the Eu implanted surface as the beginning (zero). On the other word we did show the Eu up to x = 0. Annealing at 300 ºC for the 2h led to the broadening of the implanted depth profile on both sides. The depth profile after annealing at 300 ºC is almost Gaussian. The heat treatment behaviour at higher than 300 ºC resulted in increasing diffusion toward the glassy carbon surface. The depth profiles of sample annealed at 325 ºC is still Gaussian. Although the depth profiles of the samples annealed at 350 ºC and higher temperatures are no longer Gaussian but they can be fitted to the solution of the Fick diffusion differential equation [Mal17], see Figure 7.11 (b). These fits were used to extract the diffusion coefficients for the samples annealed the different temperatures. As will be discussed later (section 7.2.6), the diffusion of europium to the glassy carbon surface caused the formation of larger crystals on the surface (see the SEM images, Figure 7.15).

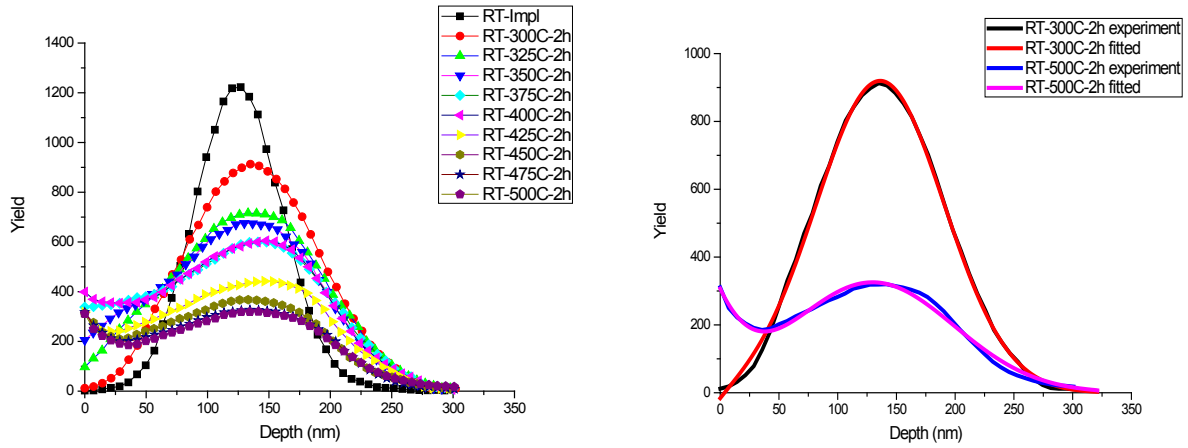

(a) (b)

Fig. 7.11. Depth profiles of (a) europium implanted into glassy carbon at room temperature and annealed between 300-500 °C for 2h and (b) fitted profiles for samples annealed between 300 and 500 ºC.

The diffusion coefficient for the sample annealed at 300 ºC is 1.2 x 10 $^{-19}$ m^2/s which is similar to that for 1h (refer to section 7.2.1). The diffusion coefficients obtained for all annealed samples are shown in Figure 7.12. From this figure it is clear that there is no trend in the diffusion coefficients

as a function of annealing temperature, i.e. the diffusion coefficient does not have an Arrhenius behavior. This behavior is the same as for the samples annealed for 1 h. Again this is due to continuous annealing of defects during the heating of the samples. Since the annealing were done sequentially, the previous heat treatments affected the microstructure of sample and consequently the diffusion coefficient.

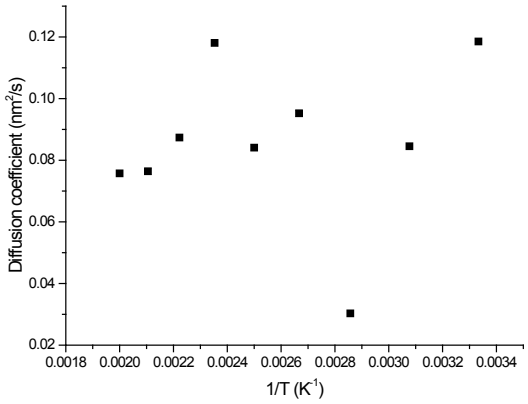

Fig. 7.12. Diffusion coefficient for annealed sample between 300-500 ºC for 2h.

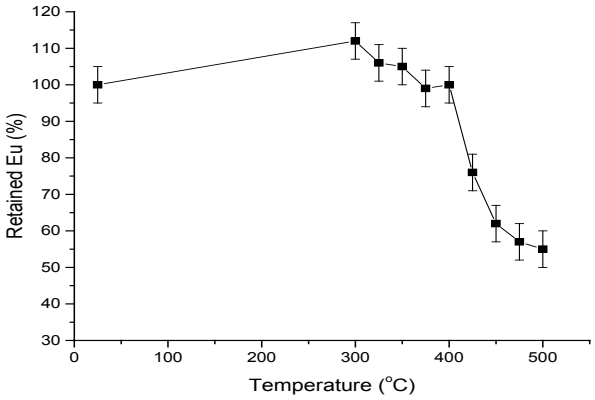

Fig. 7.13. Retained value (%) of room temperature Eu-implanted (with an estimated 5% error bar) after sequential isochronal annealing from 300 to 500°C for 2h.

To obtain the amount of europium lost/retained in the surface, we calculated the areas under the europium curves from the RBS depth profiles. Then we compared these values to that of the as-implanted europium area under curve and calculated the retained europium after annealing (Figure 7.13).

Increasing the temperature led to increasing loss of the europium. This is due to the diffusion of the europium to the surface. At higher heat treatment the defects (such as vacancies and interstitials) become mobile. This results in the rearrangement of the local bonding and graphitic-like crystallites [Kos08]. Considering the error of our RBS measurement, about 5-10%, there was no europium lost after annealing between 300 and 400 ºC while at 500 ºC that value was obtained about 55%. This means that about 45 ($\pm$ 5-10) % europium was lost after the annealing at 500 ºC for 2 hours, see Figure 7.13.

7.2.5 RAMAN RESULTS OF GLASSY CARBON IMPLANTED WITH EU AND ISOCHRONALLY ANNEALED FOR 2H

Figure 7.14 shows the Raman spectra of the pristine glassy carbon, the room temperature europium implanted and after vacuum annealing at 300, 400 and 500 ºC for 2h.

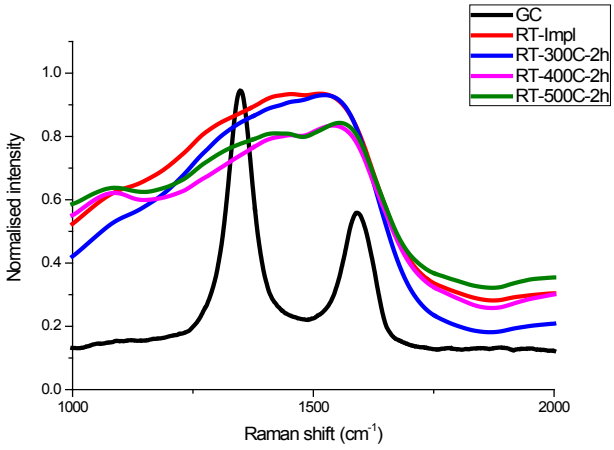

Fig. 7.14. Raman spectra of pristine glassy carbon, implanted at room temperature and annealed at 300, 400 and 500 °C for 2h.

The results of Raman spectra for the pristine glassy carbon and room temperature Eu implanted in glassy carbon were discussed in section 7.1.2. The results of this fitting (using the BWF) to samples annealing at some selected temperatures between 300 and 500 ºC for 2h are tabulated in Table 7.2.

As mentioned in section 7.2.2, the G peak wavenumber obtained for the as-implanted sample was at 1540 cm^{-1}. This value, by fitting the Raman spectra with BWF function, increased to 1548 cm^{-1} after annealing at 300 ºC for 2h. This value was the same as that for the annealing at 325 ºC for 2h. Increasing the temperature led to shift of the G peak wavenumber to the higher values. This value reached 1554 and 1567 cm^{-1} at 400 and 500 ºC, respectively.

The FWHM of the G peak (using the BWF fitting again) decreased from 195.8 at 300 ºC to 182.2 and 171.9 at 400 and 500 ºC, respectively. These changes in G peak wavenumber and its width values implies (as mentioned in section 7.1.2) that heat treatment of sample for longer period (the same temperature) leads to some degree of recovery in glassy carbon microstructure.

As indicated in Table 7.2, the I_D/I_G ratios for the samples after annealing at 300 and 325 ºC were 0.78 and 0.77, respectively. The negligible changes in I_D/I_G ratio for these two temperatures suggested that the ratio of converting the sp^2 to the sp^3 bonds is almost constant. The graphite crystal sizes (from equation 7.1) were 5.6 and 5.7 nm at 300 and 325 ºC, respectively. These values indicated that increasing temperature in step of 25 ºC at lower temperature (such as 325 ºC) even for 2h did not significantly change the crystallinity of the glassy carbon structure compared that at 300 ºC. However after annealing at 400, 450 and 500 ºC the results changed remarkably. The I_D/I_G ratio decreased to 0.47 at 400 ºC, 0.45 at 450 and 0.42 at 500 ºC, respectively. Increasing the temperature resulted in increasing the crystal size from 9.3 to 9.7 and 10.3 nm at 400 to 500 ºC for 2h, respectively. This increase in average crystal size with increasing temperature is in line with crystal growth theory [Bur51]. However, the difficulty in getting exact values when fitting distinct D and G peaks superimposed in a broad peak, places a great uncertainty on the exact values of L_a in Table 7.2.

Table 7.2. Raman results of Eu-implanted at room temperature and post-implanted annealing from 300 – 500 °C for 2h.

Temperature (°C)	I_D/I_G	La (nm)	G peak position (cm^{-1})	FWHM G peak (cm^{-1})
25 (GC)	1.8	2.5	1594	71.5
300	0.78	5.6	1548	195.8
325	0.77	5.7	1548	194.3
400	0.47	9.3	1554	182.2
450	0.45	9.7	1561	176.7
500	0.42	10.3	1567	171.9

7.2.6 SEM IMAGES OF GLASSY CARBON IMPLANTED WITH EU AND ISOCHRONALLY ANNEALING FOR 2H

The SEM images of the room temperature europium implanted sample and of the samples annealed at 300, 400 and 500 ^oC for 2 h are shown in Figure 7.15. Similar to Figure 7.10 (b), from Figure 7.15(a) it can be seen that after implantation the polishing grooves became prominent.

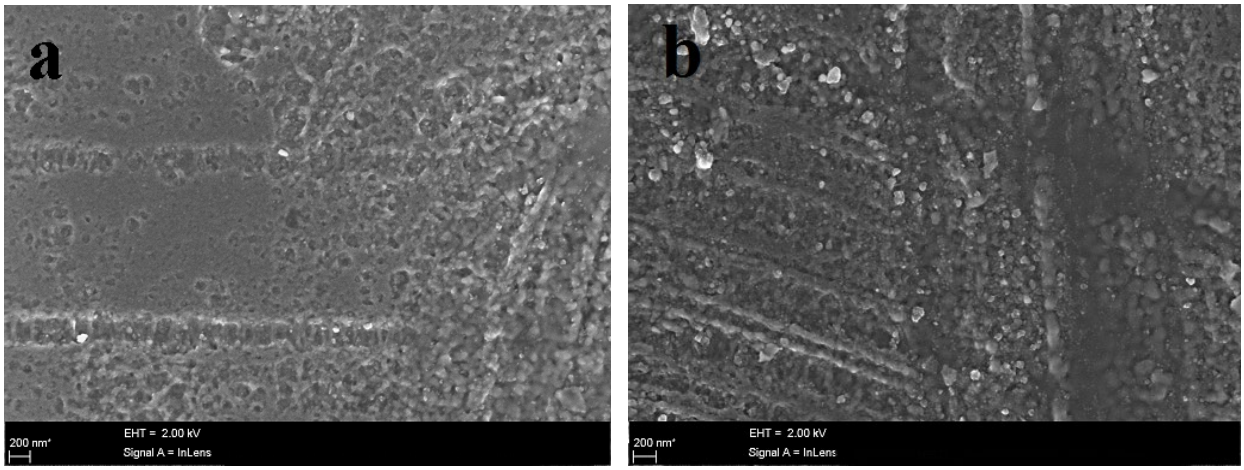

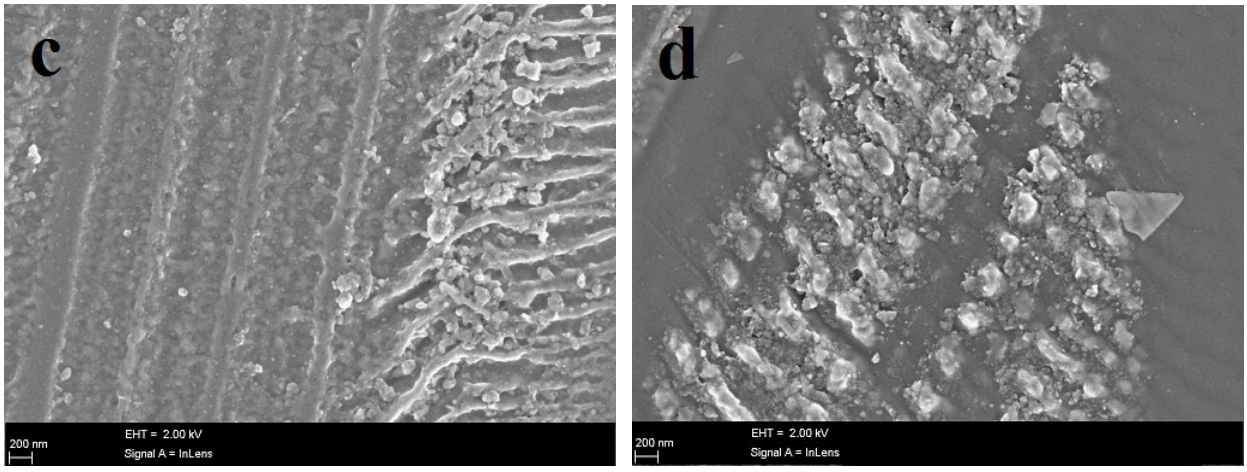

Fig. 7.15. SEM images of (a) room temperature Eu implanted, (b) annealed at 300°C, (c) 400 ºC and (d) 500°C for 2h.

After annealing at 300 ºC crystals appeared on the surface. These crystals are attributed to Eu or Eu-compounds (with carbon and/or oxygen) which were due to the diffusion of Eu to the surface, as the RBS depth profiles (see Figure 7.11) showed. From Figure 7.15 (c), it can be seen that after annealing at 400 °C, more and larger crystals appeared on the surface in line with increased diffusion and subsequent loss of Eu, see Figures 7.11 and 7.13. The crystals also clustered together. The same trend, i.e. larger crystals and clustering, also continued for the annealing at 500 °C, see Figure 7.15 (d).

7.3 RESULTS OF GLASSY CARBON IMPLANTED WITH EU AT 100 ºC

7.3.1 THE RBS RESULTS

Figure 7.16 shows the Eu depth profiles of 250 keV Eu ions implanted into glassy carbon at room temperature and at 100 ºC obtained from RBS. As can be seen in Figure 7.16, the Eu profile at the higher temperature implantation was slightly broader than the room temperature one. This means that there was some diffusion of europium in the glassy carbon. Furthermore, when comparing the area under the profile to that of the room temperature implanted profile, there was a slight reduction (about 5%) in the area indicating loss of the Eu.

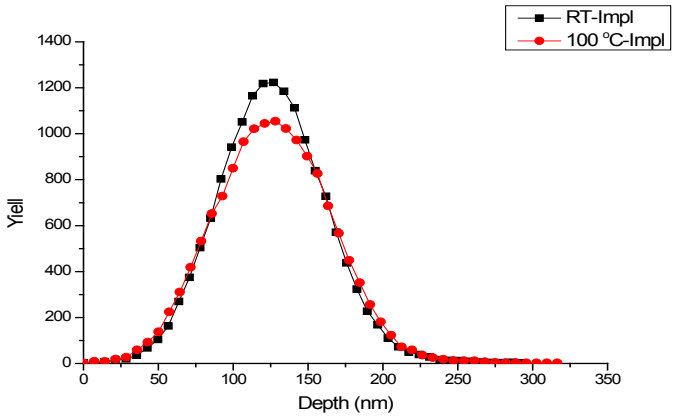

Fig. 7.16. RBS depth profiles of europium implanted in glassy carbon at room temperature and at 100 °C.

Another feature of the profiles in Figure 7.16 is that they were nearly Gaussian. As discussed in section 7.1.1 (fitting the room temperature implanted to the Edgeworth distribution), we fitted the depth profile of 100 °C implanted to the Edgeworth distribution to show that this profile is also Gaussian, see Figure 7.17. Using the Edgeworth distribution the R_p and ΔR_p obtained were about 124 and 37.5 nm, respectively. The skewness and kurtosis values obtained were about 0.02 and 3.01, respectively. As mentioned in section 7.1.1, the profile is nearly symmetric because a skewness value (γ) between $-0.5 < \gamma < 0.5$ is generally accepted to give a fairly symmetric profile.

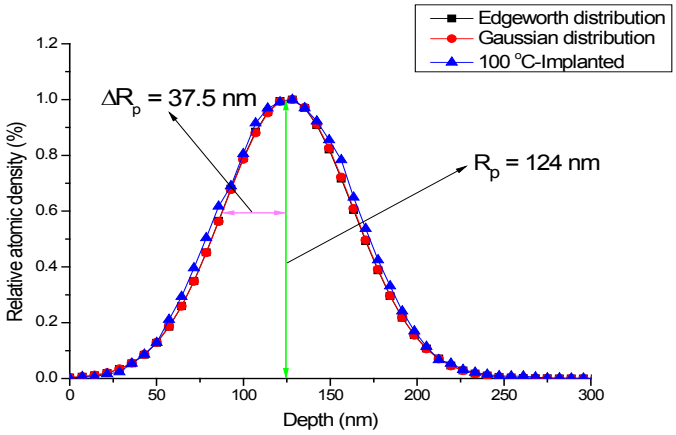

Fig. 7.17. Fitting profile of 100 °C europium implanted in glassy carbon with Edgeworth distribution

Figure 7.18 shows the europium depth profiles implanted at 100 ºC and after post-implantation annealing from 200 ºC to 1000 ºC in steps of 100 ºC. It can be seen that after annealing at 200 ºC the diffusion was negligible. After annealing at 300 ºC, the profile broadened in both sides, i.e., diffusion occurred towards the bulk and surface of the glassy carbon substrate. After annealing at 400 °C, the depth profile was no longer Gaussian. Increasing the temperature from 500 to 1000 ºC led to the movement of more europium to the glassy carbon surface. This is in agreement with results from europium retained in the glassy carbon as shown in Figure 7.20.

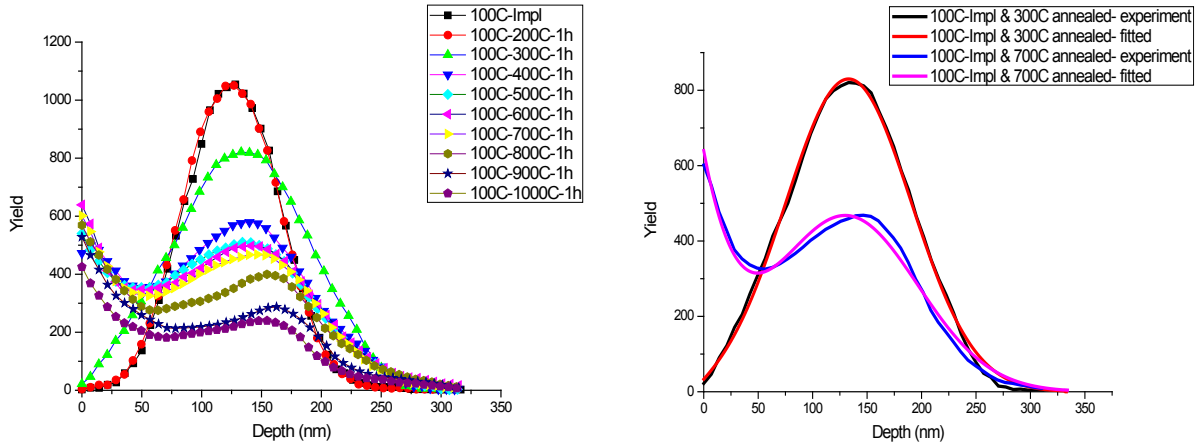

(a) (b)

Fig. 7.18. (a) Depth profiles of europium implanted into glassy carbon at 100 °C and after annealing at the various temperatures indicated in the legend. (b) Comparison between the depth profiles of samples annealed at 300 °C and at 700 °C, and the fitted curves from the solution to the Fick equation [Mal17].

As mentioned above the diffusion at 200 ºC was negligible which led to diffusion coefficient, using Ref [Mal17], of about zero. However, showed the good fitting of the experimental depth profiles at 300 – 700 ºC to theory (Figure 7.18 (b). This indicated that in this temperature range the diffusion was Fickian. However, the temperature dependence of the diffusion coefficients for this temperature range was not following the normal Arrhenius dependence. As similar to section 7.2.4, there are two region following the Arrhenius function. First is at 300-400 ºC and second is at the temperature range 400-700 ºC. The diffusion coefficient at 300 ºC was obtained about 1.24 x 10 -

^{19} m^2/s which increased to 1.9 x 10 $^{-19}$ m^2/s at 400 ºC. The D values then remained, within experimental error, i.e. 10-15%, constant for the higher annealing temperature, see Figure 7.19. As explained for the other RBS investigations, i.e. for the room temperature implanted samples which were sequentially isochronally annealed for 1 h and for 2 h, the historical heat treatment affected the microstructure of the damaged glassy carbon leading to a different diffusion rate.

The depth profiles for the samples annealed at 800-1000 ºC seem to suggest that diffusion continued in the same fashion as that for the lower annealing temperatures with increasing diffusion of the Eu to surface and loss of Eu (to be discussed below). However, the depth profiles did not fit well to the equation derived in [Mal17]. Therefore, no reliable diffusion coefficients could be obtained for these samples which suggest that the diffusion of the europium was no longer Fickian in this temperature range.

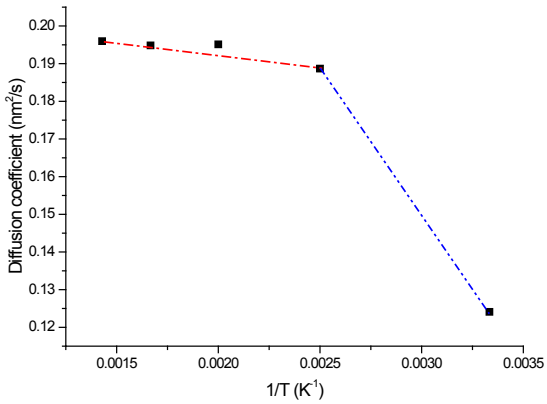

Fig. 7.19. Diffusion coefficients for sample annealed at 300-700 ºC for 1h.

Figure 7.20 shows the europium retained in glassy carbon after heat treatment behaviour at 200-1000 ºC for 1h. Considering the 100 ºC europium implanted in glassy carbon is the 100 %, at temperatures 200, 300 and 400 ºC the europium retained value were obtained 102, 101 and 100%. As mentioned in previous sections in this chapter, the RBS measurement error was about 5-10%, therefore no europium was lost, or gained, at these temperatures. However annealing at 500 and 800 ºC resulted in about 7 and 22% europium being lost. This trend continued for the higher annealing temperatures reaching about 50% at 1000 °C. This can be attributed to increased

diffusion/segregation of Eu to the surface of the glassy carbon substrate, see Figure 18. Since the melting point of Eu is 826 °C, the high value loss of europium is due to sublimation of the europium on the glassy carbon surface into the vacuum.

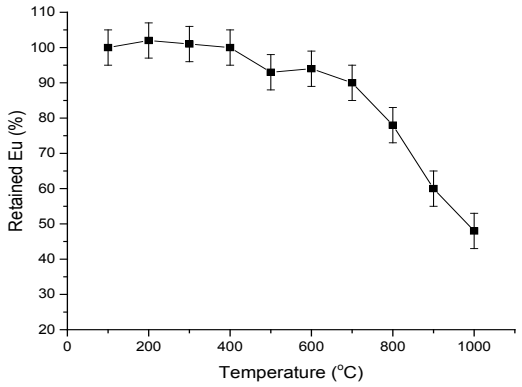

Fig. 7.20. Retained value (%) of Eu-implanted at 100 °C (with an estimated 5% error bar) after annealing between 200-1000 °C for 1h.

7.3.2 RAMAN RESULTS

Figure 7.21 shows the Raman spectra for virgin glassy carbon and after 100 °C europium implantation.

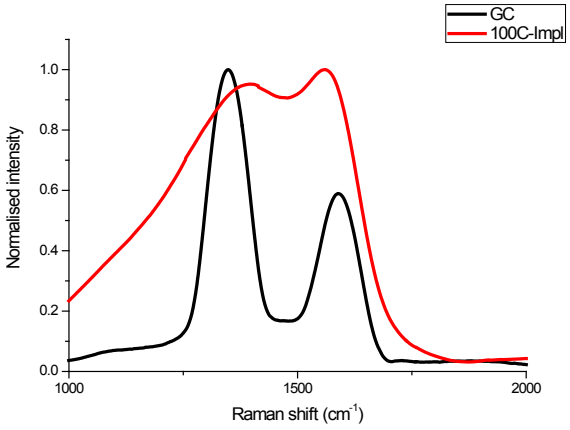

Fig. 7.21. Normalised Raman spectra for pristine glassy carbon and after 250 keV europium implantation at 100 °C.

As mentioned in the sections on the Raman results for room temperature implanted samples, we used the BWF function to fit the Raman spectra. After ion implantation at 100 °C the D and G peaks were merged and formed a single broad peak. However, in contrast to room temperature as-implanted samples, small G and D peaks appear superimposed on the broad peak, see Figure 7.22.

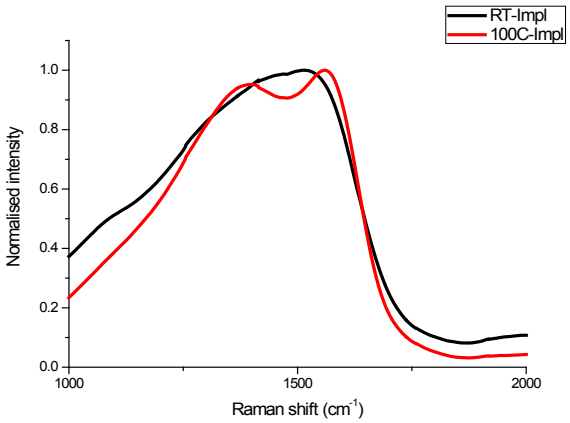

Fig. 7.22. Normalised Raman spectra of glassy carbon after europium implantation at room temperature and at 100 ºC.

Nevertheless good fitting of Lorentzian and BWF functions to these peaks cannot be done without assuming extra sub-peaks. This merging of the D and G peaks is characteristic of amorphous carbon, as mentioned in the Raman section (7.1.2) [McC94], [Fer00], [Odu18].

After implantation and fitting the Raman spectrum (by fitting BWF), the G peak position shifted to a lower wavenumber of 1567 cm^{-1}. The G peak FWHM increased from 71.5 to 149.8 cm^{-1} after implantation at 100 ºC. This decrease of the G peak position and increase in FWHM (as mentioned for room temperature implanted sample) confirmed that the ion implantation had changed the near-surface region (i.e., the implanted region) from glassy carbon to amorphous carbon as suggested by amorphisation trajectory [Les84]. It is interesting to note that corresponding changes after room temperature Eu implantation were 1540 cm^{-1} for the G peak position and 212 cm^{-1} for the FWHM of the G peak.

The I_D/I_G ratio decreased from 1.8 to 1.08 which is less than that for room temperature implantation. This could be implied that less than 15% sp^2 bonds changed to sp^3. This means less damage of glassy carbon structure. The other proof for this statement was already mentioned above, i.e. the fact after 100 ºC implantation the D and G peaks were visible. These two observations, together with the corresponding changes in the G peak position and its FWHM, indicated that less damage to the glassy carbon microstructure occurred during the 100 ºC implantation than during room temperature implantation. This enhanced annealing of radiation-induced defects during ion implantation at an elevated temperature is not uncommon and has been observed in other systems such as SiC [Mal13].

Figure 7.23 shows the Raman spectra for pristine glassy carbon, the 100 ºC europium implanted sample and then annealed at 300, 400, 900 and 1000 °C.

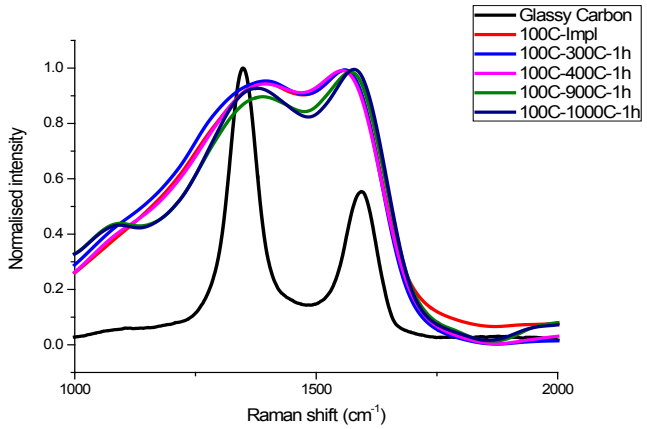

Fig. 7.23. Raman spectra of pristine glassy carbon, as-implanted at 100 ºC and annealed at 300, 400, 900 and 1000 °C for 1h.

Annealing at 300 and 400 °C led to an increase in the G peak wavenumber to 1556 and 1557 cm^{-1}, respectively. For the room temperature implanted samples which were annealed at 300 and 400 ºC the corresponding increases in the G peak position were 1550 and 1549 cm^{-1} which are less than that for the 100 ºC europium implanted. The fact that less damage to the glassy carbon microstructure is created by ion bombardment at 100 ºC compared to room temperature ion implantation, is basically the reason for these differences. From the theory of crystal growth

[Bur51], follows at annealing of defects is enhanced for systems with less damage. This trend continues when the annealing temperature is increased to 900 and 1000 ºC. The G peak positions moved to the higher wavenumbers at 1578 cm^{-1} and 1586 cm^{-1}, respectively. Comparing these values to G peak wavenumber of pristine glassy carbon at 1594 cm^{-1}, implies again that, by increasing the annealing temperature, some limited recovery of glassy carbon structure took place.

From Figure 7.24, it can be also seen that the G peak position is not as the same as for pristine glassy carbon after annealing at 1000 ºC for 1h. This means the heat treatment did not remove all the damage created by ion implantation. There was still induced-radiation damage retained in the glassy carbon implanted by Eu ions. Similar Raman results have been obtained in other studies [Odu18], [Lan12], [Njo17].

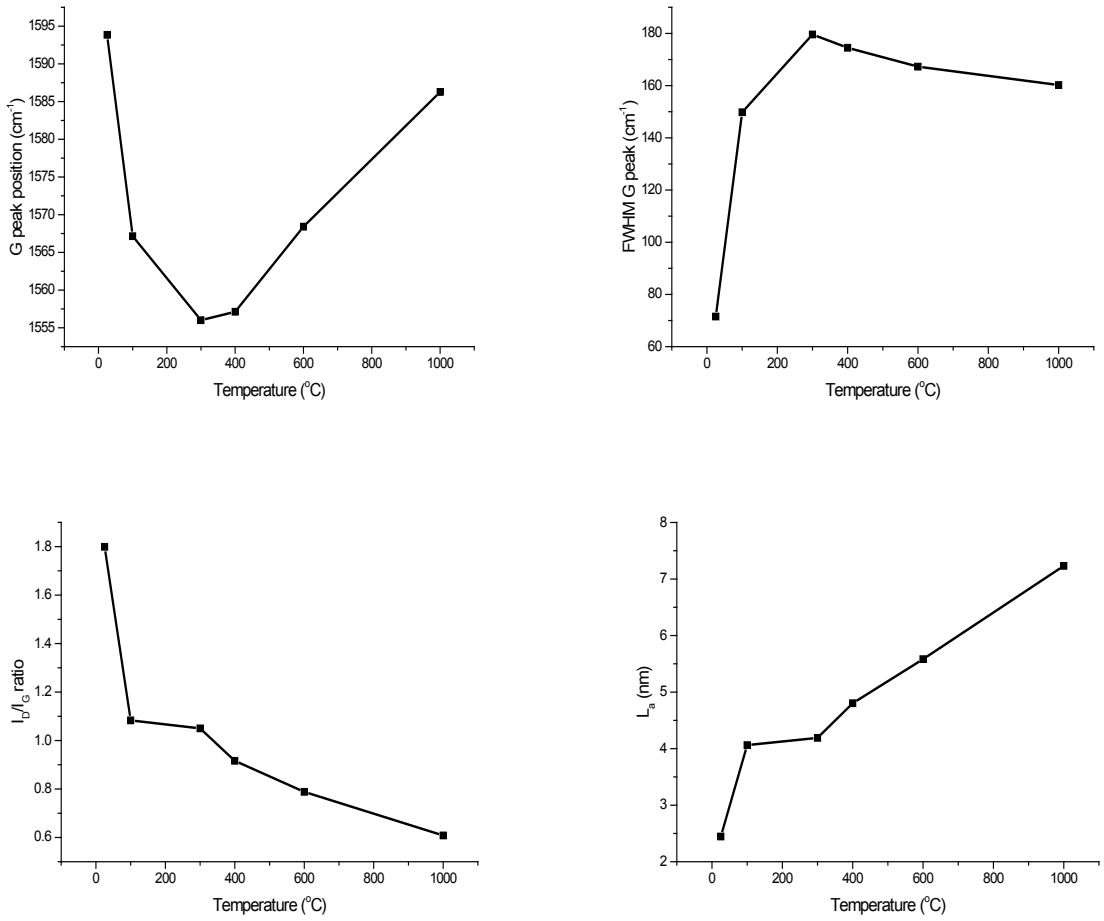

Fig. 7.24. Raman results (I_D/I_G ratio, G peak position and FWHM G peak) for glassy carbon after europium implantation at 100 ºC and annealing at 300, 400, 900 and 1000 ºC for 1h.

7.3.3 SEM RESULTS

Comparing the SEM images of pristine glassy carbon, Figure 7.25 (a) and 100 ºC implanted, Figure 7.25 (b), shows that the polishing marks from the mechanical polishing in implanted sample became pronounced after ion bombardment. After ion implantation and subsequent annealing, at 200 and 300 ºC (not shown here), these marks became prominent as grooves in the SEM images. During the polishing process, the loose carbon material collected in the grooves and remained stuck due to Van der Waals bonding.

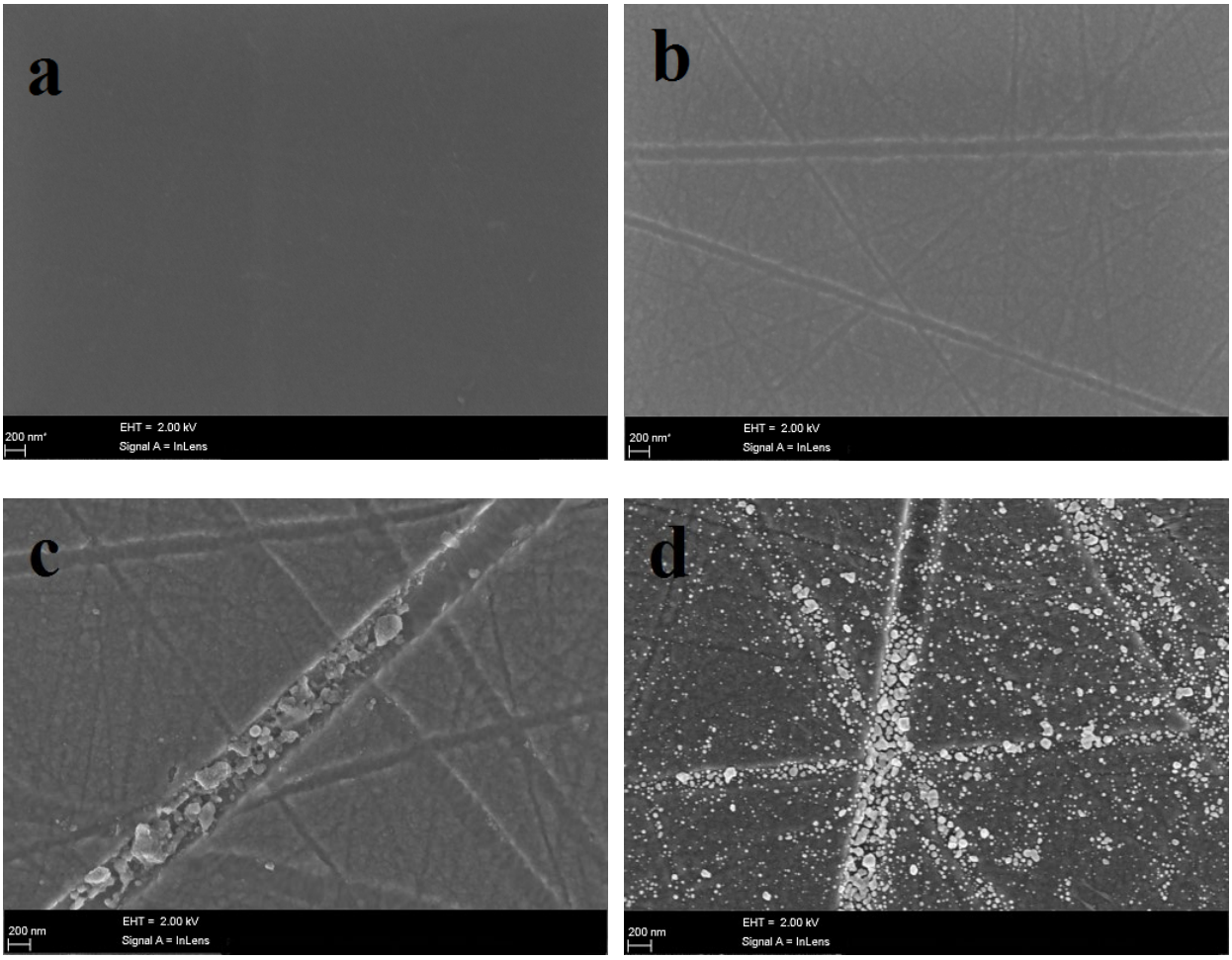

Fig. 7.25. SEM images of (a) pristine glassy carbon, (b) glassy carbon after 100 °C Eu implantation, and subsequent annealing at (c) 400 °C and (d) 1000 °C for 1h.

During implantation, the bombarding Eu ions sputtered these loosely bounded carbon atoms away, leading to the emergence of the polishing grooves. From Figure 7.25 (c), it can be seen that after annealing at 400 °C, crystals appeared on the glassy carbon surface. These crystals were attributed to Eu or Eu-compounds which were due to the diffusion of Eu to the surface, as seen in the RBS depth profiles, see Figure 7.18.

By increasing the heat treatment temperature to 1000 °C, it follows from Figure 7.25 (d) that the number of crystals increased but that they were smaller in size. The increase in the number of crystals was due to more diffusion of europium particles to the glassy carbon surface. Since this temperature of 1000 ^{o}C was higher than the melting point of Eu ($T_{melting}$ = 826 °C), this resulted in some sublimation of the Eu, thereby leading to a reduction in size. Another observation in Figure 7.25 (d) was the conglomeration of the Eu crystals in the polishing grooves. The mechanical grinding process changed the surface binding energies of the substrate atoms, especially in the grooves. This changed the Gibbs free energy of the system leading enhanced segregation in the grooves.

7.5 STEP HEIGHT AND DENSITY

In Chapter 2 (section 2.2.4) we discussed glassy carbon, its structure, properties and applications. It was mentioned that glassy carbon is a non-graphitizing carbon. It has the ribbon-like, tangled and fullerene-like microstructure. The tangled structure (due to a high number of tightly packed particles) leads to the low reactivity of glassy carbon which is the significant feature of glassy carbon [Har04]. Figure 7.26 shows a HRTEM image of pristine glassy carbon at a depth of 500 nm. Odutemowo *et al.* [Odu18] showed that after Sr ion bombardment of glassy carbon, it lost its fullerene-like structure and had amorphous-like structure. However, there were still graphite fringes which presented in glassy carbon surface (amorphised region). Studies [McC94], [Odu18], [McC93] show that after ion bombardment of glassy carbon the density of glassy carbon (1.42 g/cm^3) increases. This means that there is a different value for the thickness and subsequently density between unimplanted and implanted glassy carbon substrate. The change in height is as a result of an increase in density of glassy carbon.

To prove this, a step height measurement between the pristine glassy carbon and Eu-implanted at different temperatures were done by step height profiler. Figure 7.27 shows a typical profile obtained on one of the implanted glassy carbon samples by the step height profiler set-up at University of Pretoria.

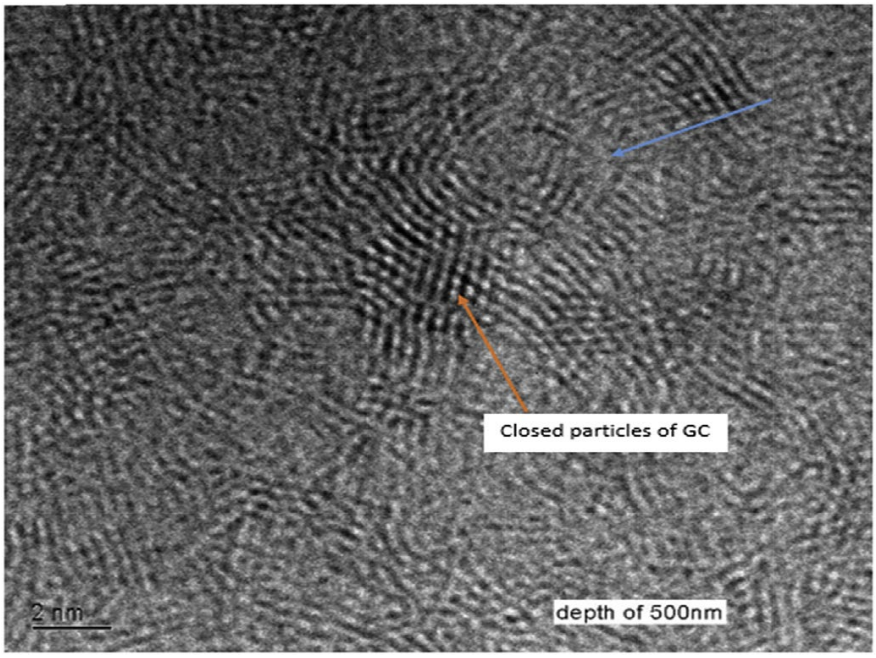

Fig. 7.26. The HRTEM image of the pristine glassy carbon. Taken from [Odu18]

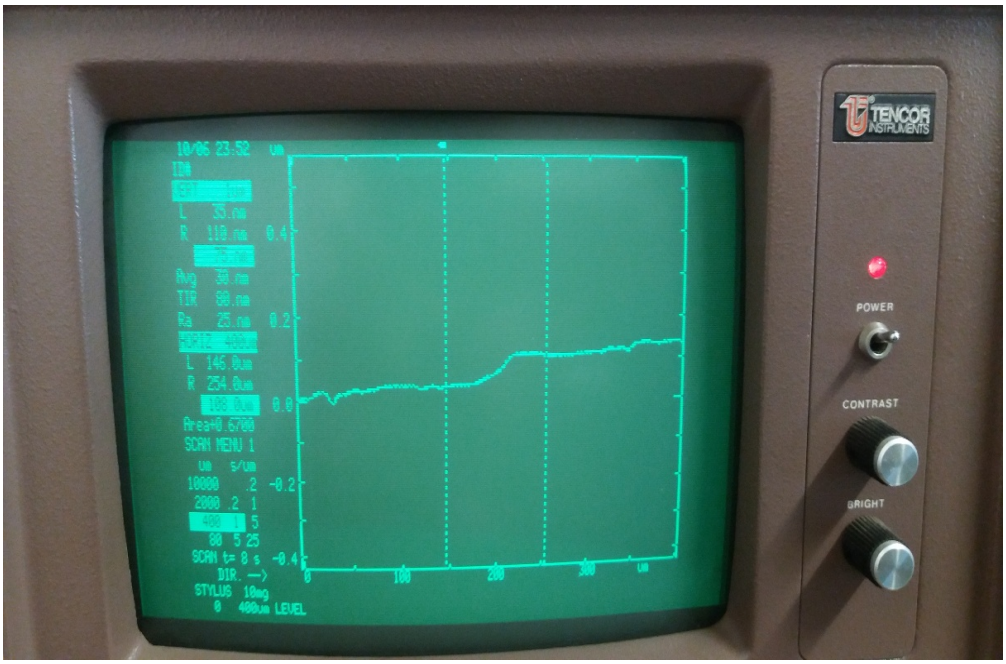

Fig. 7.27. The step height profiler set up at University of Pretoria with a typical profile.

For high accuracy of the obtained values from step height profiler, the measurements were repeated five times for every single sample. Then the average value was taken as the step height value for the sample. To calculate the density after ion bombardment, we assumed a constant mass value. Mass loss due to sputtering and the increase in the mass due to implantation of the europium ions into the glassy carbon were not taken into account. Then we followed the relationship as below;

$$\rho_i V_i = \rho_f V_f \tag{7.4}$$

where the V_i and V_f are the initial and final volumes, and ρ_i is the volume density of pristine glassy carbon and ρ_f is the final density of implanted region in glassy carbon. Then the formula can be obtained as below;

$$\rho_{imp}\, t_{imp} = \rho_{GC}(t_{imp} + \delta) \tag{7.5}$$

where ρ_{imp} is the density of the implanted area, t_{imp} is the thickness of the implanted area, ρ_{GC} is the density of glassy carbon and δ is the step height value. Using ρ_{GC} = 1.42 g/cm^3 and t_{imp} = R_p + ΔR_p [McC94], we can calculated the density of implanted layer (ρ_{imp}). The Rp and ΔRp were obtained from the fitting of the RBS depth profile to the Edgeworth distribution (see section 7.1).

The changes in the glassy carbon density after europium bombardment at different temperatures were introduced in Table 7.3.

The thickness of the implanted layer is usually taken to be $R_p + \Delta R_p$ [McC94], [Odu18]. By examining the change in the *G* and *D* peak positions in Raman spectroscopy in glassy carbon, it was found [Pra90] that the transformation begins to occur at a damage level of 0.21 displacements per atom (dpa) for a wide range of ion species (H, He, C, N, Si, and Xe). In this study the dpa value is about 3.5, Figure 7.1. This figure shows that the implanted depth (theoretically) is about 200 nm ($R_p + 2\Delta R_p$). However to get the homogenous thickness we need to consider less than that value which is $R_p + \Delta R_p$. Using the SRIM code gives the dpa parameter which is proportional to the energy density deposited by the incoming ion in nuclear collisions. Because SRIM does not take into account dynamic annealing or the effect of multiple impacts, the dpa parameter almost certainly overestimates the actual damage density for a given ion dose [McC94]. From Figure 7.1 (SRIM profile) it can be seen that the damage region (density) is ~ $R_p + \Delta R_p$ (< 200 nm).

Table 7.3. Density of the implanted glassy carbon layer after 250 keV europium bombardment at different temperatures

Implanted Samples	**$R_p+\Delta R_p$ Values**	**Average Step Height (δ)**	**Density of glassy carbon after Eu-implanted (ρ_{imp})**
Room temperature	160.2 nm	73 nm	2.07 g/cm^3
100 ºC	161.5 nm	55 nm	1.90 g/cm^3
150 ºC	161.6 nm	43 nm	1.80 g/cm^3
200 ºC	161.2 nm	40 nm	1.77 g/cm^3

The value of density for optimised tetrahedral amorphous carbon (ta:C) is 3.26 g/cm^3 which has about 85% sp^3 content. In addition, for hydrogenated diamond-like carbon (DLC:H) this value is about 2.35 g/cm^3 with about 75% sp^3 bonds [Lib00]. Our result for 250 keV implanted europium in glassy carbon at room temperature was 2.07 g/cm^3 which is less than that for optimised amorphous and DLC:H materials. The Raman results, in section 7.1.2, showed that in glassy

carbon about 15% of sp^2 bonds changed to sp^3 bonds after ion bombardment. This means that the dose/energy was not sufficient to cause the formation of optimised (fully) amorphous glassy carbon. This value shows that 250 keV Eu-implanted at room temperature caused only partial amorphisation of the glassy carbon.

From Table 7.3, it is clear that by increasing the Eu-implanted temperature, the density of glassy carbon decreased. Ion implantation at 100 ^oC led to decrease the density value from 2.07 to 1.90 g/cm^3. It can be implied that increasing the implanted temperature led to self-annealing of glassy carbon during the bombardment in agreement with the Raman results discussed in section 7.3.2. By increasing the substrate temperate, at 150 and 200 ^oC, the density decreased to 1.8 and 1.77 g/cm^3, respectively, i.e. increased self-annealing at the higher implantation temperatures.

REFERENCES

[Ada10] F. Adar, E. Lee, S. Mamedov, and A. Whitley, “Experimental Evaluation of the Depth Resolution of a Raman Microscope”, Microscopy Society of America, pp. 360, 2010.

[Bar94] J. Barbillat, P. Dhamelincourt, M. Delhaye, and E. da Silva, **“**Raman confocal microprobing, imaging and fibre-optic remote sensing: A further step in molecular analysis”, Journal of Raman Spectroscopy. 25, pp. 3, 1994.

[Bur51] W. K. Burton, N. Cabrera, F. C. Frank, "The Growth of Crystals and the Equilibrium Structure of their Surfaces", Philosophical Transactions of the Royal Society A: Mathematical, Physical and Engineering Sciences, 243(866), pp. 299–358, 1951.

[Dil84] R. O. Dillon, J. A. Woollam, V. Katkanant "Use of Raman scattering to investigate disorder and crystallite formation in as-deposited and annealed carbon films", Physical Review B, 29(6), 1984.

[Dul84] W. W. Duley, “Refractive indices for amorphous carbon”, Astrophysical Journal, 287, pp. 694-696, 1984.

[Eve00] N. J. Everall, “Confocal Raman Microscopy: Why the Depth Resolution and Spatial Accuracy Can Be Much Worse than You Think”, Society for Applied Spectroscopy, 54 (10), pp. 1515, 2000.

[Fer07] A. C. Ferrari, "Raman spectroscopy of graphene and graphite: disorder, electron-phonon coupling, doping and nonadiabatic effects", Solid State Communications, 143, pp. 47–57, 2007.

[Fer00] A. C. Ferrari, J. Robertson, "Interpretation of Raman spectra of disordered and amorphous carbon", Physical Review B, 61, 2000.

[Fer04] A. C. Ferrari, J. Robertson, "Raman spectroscopy of amorphous, nanostructured, diamond-like carbon, and nanodiamond", Philosophical Transactions of the Royal Society of London A: Mathematical, Physical and Engineering Sciences, 362(1824), pp. 2477–2512, 2004.

[Geb66] R. E. Gebelt and H. A. Eick, “Vaporization Behavior of Europium Dicarbide”, Journal of chemical physics, 44(8), pp. 2872, 1966.

[Gor10] T. Gorda, M. Russo, and J. Sloane, “Raman scattering”, 2010.

[Har04] P. J. F. Harris, "Fullerene-related structure of commercial glassy carbons", Philosophical Magazine, 2004.

[Hla17] T. T. Hlatshwayo, L. D. Sebitla, E. G. Njoroge, M. Mlambo, J .B. Malherbe, "Annealing effects on the migration of ion-implanted cadmium in glassy carbon", Nuclear Instruments and Methods in Physics Research, Section B: Beam Interactions with Materials and Atoms, 395, pp. 34–38, 2017.

[Jua88] C. B. Juang, L. Finzi, and C. J. Bustamante, “Design and application of a computer-controlled confocal scanning differential polarization microscope”, Rev. Sci. Instrum. 59, pp. 2399, 1988.

[Kos08] O. Koskelo, U. Köster, I. Riihimäki, J. Räisänen, "Migration kinetics of ion-implanted beryllium in glassy carbon", Diamond & Related Materials, 2008

[Lan12] D. F. Langa, N. G. van der Berg, E. Friedland, J. B. Malherbe, A. J. Botha, P. Chakraborty, E. Wendler, W. Wesch, "Heat treatment of glassy carbon implanted with cesium at room and high temperatures", Nuclear Instruments and Methods in Physics Research, Section B: Beam Interactions with Materials and Atoms, 273, pp. 68–71, 2012.

[Lav08] V. Lavrentiev, J. Vacik, H. Naramoto, "Structural phenomena in glassy carbon induced by cobalt ion implantation", Applied Physics A: Materials Science and Processing, 92(30), pp. 673–680, 2008.

[Les84] P. Lespade, A. Marchand, "Characterization of carbon materials by Raman microspectrometry", Carbon, 1984.

[Li11] Y. Li, M. Ge, J. Li, J. Wang, H. Zhang, "Synthesis of mesoporous Eu_2O_3 microspheres and Eu_2O_3 nanoparticle-wires as well as their optical properties", The Royal Society of Chemistry, 2011.

[Lib00] A. Libassi, A. C. Ferrari, V. Stolojan, B. K. Tanner, J. Robertson, L. M. Brown, "Density and sp^3 content in diamond like carbon films by x-ray reflectivity and electron energy loss spectroscopy", Materials Research Society, 2000.

[Mal13] J. B. Malherbe, "Diffusion of fission products and radiation damage in SiC", Journal of

Physics D: Applied Physics, 46(47), 2013.

[Mal17] J. B. Malherbe, P. A. Selyshchev, O. S. Odutemowo, C. C. Theron, E. G. Njoroge, D. F. Langa, T. T. Hlatshwayo, "Diffusion of a mono-energetic implanted species with a Gaussian profile", Nuclear Instruments and Methods in Physics Research, Section B: Beam Interactions with Materials and Atoms, 406, pp. 708–713, 2017.

[Mat99] M. J. Matthews, M. A. Pimenta, G. Dresselhaus, "Origin of dispersive effects of the Raman D band in carbon materials", Physical Review B, 59(10), pp. 6585–6588, 1999.

[McC93] D. McCulloch, S. Prawer, A. Hoffman, D. K. Sood, "Cross-sectional transmission electron microscopy investigation of xenon irradiated glassy carbon", Nuclear Inst. and Methods in Physics Research, B, 1993.

[McC94] D. McCulloch, S. Prawer, A. Hoffman, "Structural investigation of xenon-ion-beam-irradiated glassy carbon", Physical review B, 50, pp. 5905, 1994.

[Njo17] E. G. Njoroge, L. D. Sebitla, C. C. Theron, M. Mlambo, T. T. Hlatshwayo, O. S. Odutemowo, V. A. Skuratov, E. Wendler, J. B. Malherbe, "Structural modification of indium implanted glassy carbon by thermal annealing and SHI irradiation", Vacuum, 144, pp. 63–71, 2017.

[Odu16] O. S. Odutemowo, J. B. Malherbe, L. C. Prinsloo, D. F. Langa, E. Wendler, "High temperature annealing studies of strontium ion implanted glassy carbon", Nuclear Inst. and Methods in Physics Research B, 371, pp. 332–335, 2016.

[Odu18] O. S. Odutemowo, J. B. Malherbe, L. C. Prinsloo, E. G. Njoroge, R. Erasmus, E. Wendler, A. Undisz, M. Rettenmayr, "Structural and surface changes in glassy carbon due to strontium implantation and heat treatment", Journal of Nuclear Materials, 498, pp. 103–116, 2018.

[Pra90] S. Prawer, F. Ninio and I. Blanchonette, “Raman spectroscopic investigation of ion-beam irradiated glassy carbon”, Journal of Applied Physics, 68, pp. 2361, 1990.

[Rob02] J. Robertson, "Diamond-like amorphous carbon", Elsevier, 2002.

[Sig69] P. Sigmund, "Theory of sputtering. I. Sputtering yield of amorphous and polycrystalline targets", Physical Review, 184(2), 1969.

[Tab92] R. Tabaksblat, R.J. Meier, and B.J. Kip, “Confocal Raman Microspectroscopy: Theory and Application to Thin Polymer Samples”, Appl. Spectrosc. 46, pp. 60, 1992.

[Tak85] K. Takahashi, K. Yoshida, M. Iwaki, "Effect of ion implantation on electrochemical and surface properties of glassy carbon", Nuclear Inst. and Methods in Physics Research, B, 8, pp. 526–529, 1985.

[Tui70] F. Tuinstra, J. L. Koenig, "Raman Spectrum of Graphite", Journal of Chemical Physics, 53(3), 1970.

[Yan91] Q. Yang, D. J. O’Connor, Z. Wang, "Empirical formulae for energy loss straggling of ions in matter", Nuclear Inst. and Methods in Physics Research, B, 61(2), pp. 149–155, 1991.

[Zie13] J. F. Ziegler, "SRIM 2013 computer code, www.SRIM.org", USA, 2013.

CHAPTER 8

CONCLUSION

Europium is one of the fission products of uranium and plutonium. If it is released into the environment it can be taken into the body by breathing. Europium is toxic to lungs and mucous membrane if inhaled. It is also corrosive and burn skin. If europium reaches the blood, by deposition in the liver, and on the bone surface, it can be caused the cancer. It can be also absorbed and deposited in the kidneys.

Glassy carbon is such a material containing appropriate properties which might be used in nuclear reactors. It has significant properties such as chemical attack resistance, extreme corrosion and erosion resistance, strength and hardness, the impermeability to gases and liquids, the high resistance to thermal shock and etc. Thus it can be used as a diffusion barrier in nuclear reactors.

In this study glassy carbon samples were implanted with 250 keV europium ions at room temperature and at 100 ^{o}C. After implantation the samples were investigated by several techniques to determine the damage created by the ion bombardment processes and also the distribution of the europium atoms. The room temperature implanted europium were also isochronally but sequentially annealed in vacuum in wide ranges of temperatures such as 200-1000 ^{o}C (1h) and 300-500 ^{o}C (2h). The 100 ^{o}C europium implanted was also isochronally but sequentially annealed in vacuum from 200-1000 ^{o}C for 1h. The diffusion properties of the europium in the glassy carbon were then investigated with Rutherford backscattering spectrometry (RBS). These samples were analyzed to investigate the annealing of the initial irradiation damage, the diffusion of the implanted europium and possible reactions between the europium and glassy carbon induced by the ion bombardment and annealing.

The RBS results for room temperature implanted europium and post-implantation annealing for 1h, showed that increasing the temperature led to diffusion of europium. In annealing at 200 and 300 ^{o}C, the diffusion profile is Fickian type and the diffusion coefficients were 2.3×10^{-19} and 1.2×10^{-19} m^2/s, respectively. The fact that the diffusion coefficient at 300 ^{o}C was less than the one at 200 ^{o}C was an unexpected result. This was explained by the different annealing histories of the

two samples which changed the microstructure of the glassy carbon substrate. Because diffusion on a particular system depends critically on the microstructure of the substrate, this change in microstructure of the glassy carbon led to different diffusion processes. Annealing at 400 ^{o}C resulted in the whole Eu profile to shift deeper inside the glassy carbon and then to remained static even after annealing at 1000 ^{o}C. Although the depth profile from 400-1000 ^{o}C remained Gaussian, it did not exhibit Fickian diffusion. This can be attributed to the dependency of the diffusion behavior to the changes in the substrate microstructure at these temperatures. Annealing at 400 ^{o}C led to loss of europium about 30%. However increasing the temperature did not change this value and retained europium in the glassy carbon samples was about 70% compared to the as-implanted samples for this range of temperature (400-1000 ^{o}C).

For room temperature europium implanted glassy carbon and then annealing at 300 ^{o}C for 2h, the depth profile is also Fickian, giving a diffusion coefficient of 1.2×10^{-19} m^2/s, same as that for 1h. Europium diffusion at this temperature occurred in both sides (to surface and bulk) of glassy carbon. After annealing at higher than 300 ^{o}C the europium also diffused to the surface. The diffusion coefficients at these higher annealing temperatures did exhibit an Arrhenius behavior. There was no europium lost at 300-400 ^{o}C, while for the annealed sample from 425-500 ^{o}C for 2h, the europium loss was about 25-45 %.

The depth profile of europium implanted into glassy carbon at 100 ^{o}C (higher than room temperature) is slightly broader than that of the room temperature implanted sample. Annealing at 200-1000 ^{o}C for 1h led to diffusion of europium to the glassy carbon surface. At 200 and 300 ^{o}C the depth profiles were approximately Gaussian. The diffusion coefficient at 200 ^{o}C was negligible giving a D value of about zero. The diffusion coefficient values at 300 and 400 ^{o}C were 1.24×10^{-19} and 1.9×10^{-19} m^2/s, respectively. Good fitting of the experimental depth profiles to theory was obtained for the samples annealed from 300-700 ^{o}C indicating that the diffusion was Fickian. This is attributed to the fact that increasing the temperature led to more diffusion. The depth profiles for the samples annealed from 800-1000 ^{o}C could no longer be fitted to the solution to the Fick diffusion differential equation. However, there was still europium migration to the surface resulting in europium loss reaching about 50% at 1000 ^{o}C which is higher than the europium melting point ($T_{melting}$ = 826 ^{o}C).

As we stated in thesis, because of the sensitivity of Raman spectroscopy to structural changes, it is a powerful technique to monitor the microstructure changes in materials and also in carbon based materials [Kni88]. We used Raman to investigate the changes in bonding (sp^2 to sp^3) after ion bombardment. Raman spectra showed that ion implantation caused the two distinct (D and G) peaks of pristine glassy carbon to merge. After europium implantation the D and G peaks were undistinguishable which implied the amorphisation of implanted layer of the glassy carbon. Using BWF functions and peak fitting, the I_D/I_G ratio also showed after ion implantation this ratio remarkably decreased which can be explained by the amorphisation trajectory. The drop of the I_D/I_G ratio europium implantation suggested that about 15% of sp^2 converted to the sp^3 bonds.

For room temperature implanted europium in glassy carbon, after heat treatment at 300 and 400 ^oC for 1h, the D and G peaks just became noticeable on the broad merged peak. With increasing annealing temperature up to 1000 ^oC, these superimposed peaks also increased to become even more pronounced. Using BWF fitting, the G peak position increased while the FWHM of the G peak decreased with increasing annealing temperature. Reappearance of D and G peaks accompanied by the movement of G peak to the higher wavenumber implies that partial recovery of the glassy carbon structure took place. However the G peak position even after annealing at 1000 ^oC for 1h did not reach that for the pristine glassy carbon. This is due to retained radiation damage even after annealing at temperatures higher than the melting point of europium i.e. 826 ^oC.

The Raman results for room temperature europium implanted and annealing for 2h, are the same that for 1h. Using BWF fitting, the G peak moved to the higher wavenumber and the I_D/I_G ratio decreased. Using the TK formula the crystal size increased at 300-500 ^oC for 2h. The crystal size obtained from 5.6 nm at 300 ^oC increased to 10.3 nm at 500 ^oC.

The same results was obtained for 100 ^oC implanted europium in glassy carbon and then annealed. However, in contrast to room temperature as-implanted samples, where they were not visible, small G and D peaks appear superimposed on the broad peak. By fitting BWF to the Raman spectra for the 100 ^oC implanted samples, results gave the same trend of that for the room temperature implanted samples. The G peak position increased with increasing annealing temperatures in the range 300-1000 ^oC, while the I_D/I_G ratio decreased after implantation and annealing up to 1000 ^oC. The crystal size (L_a) increased by elevating the annealing temperature.

To investigation the morphology changes on the surfaces of the samples, SEM analysis carried out. The images showed that implantation and subsequent annealing changed the surface morphology by the formation of crystals which was attributed to europium compounds (carbide or oxide). This was due to the diffusion of europium to the glassy carbon surface.

Using step height measurements, the density of glassy carbon after implantation was obtained. The density of pristine glassy carbon is 1.43 g/cm^3 while it increased to 2.07 g/cm^3 after europium ion implantation at room temperature. The density of glassy carbon also increased to 1.9, 1.8 and 1.77 g/cm3 after europium implantation at 100, 150 and 200 ºC, respectively.

Finally, all the results were analyzed to make a recommendation about the suitability of glassy carbon as a storage material for one of the important fission products, i.e. europium. The diffusion/segregation of europium to the surface to surface; amorphisation of glassy carbon after ion implantation are the positive aspect of the research. Amorphisation was caused the density of glassy carbon increased. The amorphisation and compaction in the implanted layer of glassy carbon results in a surface layer which is significantly more resistant to abrasion than as-grown glassy carbon. Consequently, this study shows that glassy carbon should be a good storage material for radioactive europium.

REFERENCES

[Kni88] D. S. Knight, W. B. White, "Characterization of diamond films by Raman spectroscopy", Materials Research Laboratory, 1988.

[McC94] D. McCulloch, S. Prawer, A. Hoffman, "Structural investigation of xenon-ion-beam-irradiated glassy carbon", Physical review B, 1994.

APPENDIX

- ✓ M. F. Kenari, T. T. Hlatshwayo, O.S. Odutomowo, T. M. Mohlala, E. Wendler, J. B. Malherbe, “Migration Behavior of 100 °C Europium Ion Implantation in Glassy Carbon”, accepted at Journal IEEE Xplore, November 2018.